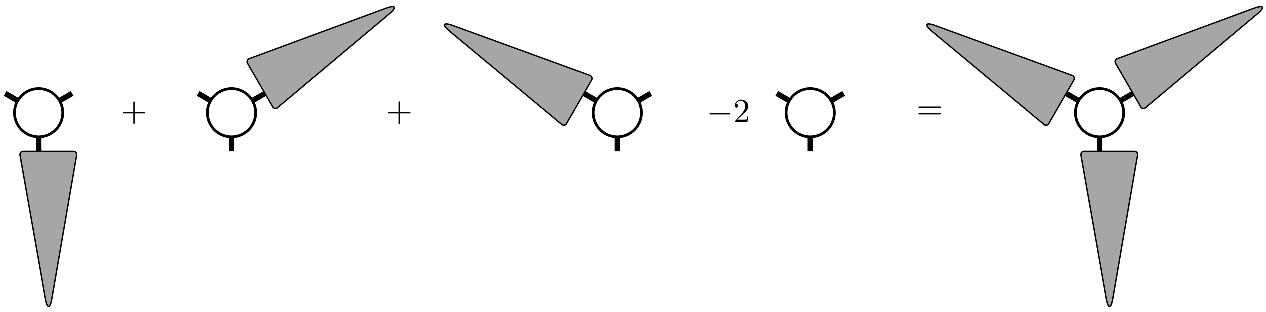

State-Space Experimental-Analytical Dynamic Substructuring Using the Transmission Simulator

Master's thesis in Applied Mechanics

MAREN SCHEEL

Supervisor: Anders T. Johansson, Chalmers University of Technology
Examiner: Prof. Arnold Kistner, University of Stuttgart

Department of Applied Mechanics
Göteborg, Sweden 20015

MASTER'S THESIS IN APPLIED MECHANICS

State-Space Experimental-Analytical Dynamic Substructuring using the Transmission Simulator

MAREN SCHEEL

Department of Applied Mechanics
Division of Dynamics
CHALMERS UNIVERSITY OF TECHNOLOGY

Göteborg, Sweden 2015

State-Space Experimental-Analytical Dynamic Substructuring using the Transmission Simulator
MAREN SCHEEL

Master's thesis 2015:91
ISSN 1652-8557
Department of Applied Mechanics
Division of Dynamics
Chalmers University of Technology
SE-412 96 Göteborg
Sweden
Telephone: +46 (0)31-772 1000

Cover:
The experimental task of this thesis is modelling the rotor of a wind turbine. Therefore, three one-bladed hubs are coupled, removing two hubs as transmission simulator.

Chalmers Reproservice
Göteborg, Sweden 2015

State-Space Experimental-Analytical Dynamic Substructuring using the Transmission Simulator
Master's thesis in Applied Mechanics
MAREN SCHEEL
Department of Applied Mechanics
Division of Dynamics
Chalmers University of Technology

Abstract

Dynamic substructuring is a powerful method to analyse complex structures by means of their substructures. While the method is well developed and widely used with Finite Element models, numerous hindrances exist for experimental dynamic substructuring. One remedy is the so-called transmission simulator which is an additional structure that matches the interface between two substructures. The physical specimen is attached to the substructure of interest and the assembly is measured. The influence of the transmission simulator is later removed from the identified model by means of its Finite Element model. By using this method, experimental models can be improved, and experimental-analytical substructuring can be performed with greater success. Over the last decade, the transmission simulator technique has been developed and used with the well-known methods Component Mode Synthesis and Frequency Based Substructuring. In this work, the transmission simulator method will be transferred to state-space synthesis, another approach for dynamic substructuring, where first-order state-space models are to be coupled. Moreover, the constraints Connection Point Constraints and Modal Constraints for Fixture and Subsystem will be applied. To verify the theoretical derivations, all aforementioned methods will be tested on a simple analytical beam example. Finally, experimental-analytical substructuring is conducted on the Ampair wind turbine, the SEM Dynamic Substructuring Focus Group benchmark structure. Experimental models of three blades will be identified with the help of the hub as transmission simulator and then coupled, removing the influence of two Finite Element hub models to arrive at a model of the rotor.

Keywords: Dynamic Substructuring, Transmission Simulator, State-Space Coupling, Ampair Wind Turbine

Zusammenfassung

Substrukturtechnik ist eine effiziente Methode, um komplexe Strukturen anhand ihrer Substrukturen zu analysieren. Das Verfahren wird häufig erfolgreich für Finite Elemente Berechnungen eingesetzt. Allerdings gibt es zahlreiche Hürden bei Anwendung von experimentellen Modellen. Mit Hilfe des Transmission Simulators können diese Modelle verbessert werden. Der Transmission Simulator steht als physikalisches Bauteil zur Verfügung und ist zusätzlich mit Finite Elemente modelliert. Das physikalische Bauteil wird mit der entsprechenden Substruktur verbunden und die Baugruppe vermessen. Später wird der Einfluss des Transmission Simulators vom experimentell bestimmten Modell entfernt. Dadurch können die Ergebnisse experimental-analytischer Substrukturtechnik verbessert werden.

Im Laufe des letzten Jahrzehnts wurde der Transmission Simulator entwickelt und mit den bekannten Methoden Component Mode Synthesis und Frequency Based Substructuring angewandt. In dieser Arbeit soll nun der Transmission Simulator auf die sogenannte State-Space Synthesis Methode übertragen werden. Dies ist ein weiterer Ansatz der Substrukturtechnik, bei dem Zustandsraummodelle erster Ordnung gekoppelt werden. Darüber hinaus werden die Bedingungen Connection Point Constraints und Modal Constraints for Fixture and Subsystem angewandt. Um die theoretische Herleitung zu überprüfen, werden alle genannten Methoden an einem einfachen Balkenbeispiel getestet.

Schließlich werden Experimente an der Ampair Windkraftanlage durchgeführt, welche von der SEM Dynamic Substructuring Focus Group als Modellstruktur ausgewählt wurde. Dadurch soll der Transmission Simulator in Anwendung mit allen drei Methoden verglichen werden. Dazu werden experimentelle Modelle dreier Rotorblätter mit Nabe als Transmission Simulator bestimmt und dann gekoppelt. Um das Modell des Rotors zu erhalten, wird der Einfluss der überzähligen zwei Naben mit Hilfe eines Finite Elemente Modells entfernt.

Preface

This thesis was written at Chalmers University of Technology, Sweden, during my ERASMUS semester in 2015 and is part of my Master studies at the University Stuttgart, Germany. Hopefully, the present work will contribute to the field of dynamic substructuring by promoting the combination of state-space synthesis and the transmission simulator. The main results regarding the wind turbine will be published at the 34^{th} International Modal Analysis Conference 2016.

Acknowledgements

First of all, I would like to thank my supervisor Assistant Professor Anders T. Johansson for welcoming me in Sweden and for giving me the opportunity to work on dynamic substructuring at Chalmers University of Technology. I am grateful for the knowledge he shared with me as well as for the interesting and stimulating discussions. Moreover, I want to thank for the numerous MATLAB scripts he provided which made this thesis feasible, and especially for giving me the possibility to publish and present my results at a conference.

Another great thank-you is directed to Mladen Gibanica who supported me with the experimental work, the Finite Element models and whose Master's thesis is the basis for this work. Furthermore, I would like to thank Prof. Thomas Abrahamsson who always had an open ear and provided many inspiring ideas. I am also very grateful that I could use scripts regarding system identification developed by Anders Liljerehn along with very helpful explanations on the theoretical background of his work.

A special thanks is directed to Randy Mayes for the meeting we had and for his ideas regarding the beam example. Without him, the verification and debugging of my methods would have been exceedingly more difficult.

I especially want to thank Pascal Reuß who initiated this collaboration, enabling me a valuable and unforgettable experience. Another thanks is directed to Prof. Arnold Kistner for taking the time to be my examiner at the University of Stuttgart and helping me with organizational matters. Additionally, I want to thank Johann Groß and Benjamin Seeger who shared their insights in dynamic substructuring with me and whose experience greatly benefited my work.

Last but not least, I want to thank my friends Simone, Adriana, and Filip who gave me support when I needed it the most, made fika breaks even more enjoyable and always had a hand to help me in the lab.

Ich versichere hiermit, dass ich die vorliegende Arbeit selbständig verfasst, noch nicht anderweitig zu Prüfungszwecken vorgelegt, keine anderen als die angegebenen Quellen oder Hilfsmittel benutzt sowie wörtliche oder sinngemäße Zitate als solche gekennzeichnet habe. Weiter erkläre ich, dass die Arbeit weder vollständig noch in Teilen bereits veröffentlicht wurde und das elektronische Exemplar mit den anderen Exemplaren übereinstimmt.

Stuttgart, den March 22, 2016 Maren Scheel

Nomenclature

$\boldsymbol{A}$	System matrix in a state-space model
A	Area
a	Modal Foss damping
$\boldsymbol{B}$	Input matrix in a state-space model
b	Width
$\boldsymbol{C}$	Output matrix in a state-space model
$\boldsymbol{D}$	Feedthrough matrix in a state-space model
$\boldsymbol{E}$	Compatibility matrix
E	Young's Modulus
F	Fourier transform of external forces
f	External forces
	Frequency in Hz
G	Fourier transform of connection forces
g	Connection forces
$\boldsymbol{H}$	Frequency Response Function matrix
h	Height
$\boldsymbol{I}$	Identity matrix
I	Second moment of area
$\boldsymbol{K}$	Stiffness matrix
	Coupling term in state-space coupling
$\boldsymbol{L}$	Boolean localisation matrix
l	Length
$\boldsymbol{M}$	Mass matrix
m	Mass
n	Number of states
$\boldsymbol{P}$	Localisation matrix for inputs and outputs
Q	Fourier transform of displacements
q	Physical displacement
r	Residual force
$\boldsymbol{T}$	Transformation matrix
t	Time
u	Input
$\boldsymbol{V}$	Damping matrix
x	State vector
y	Output
$\boldsymbol{Z}$	Dynamic stiffness matrix
H	Fourier transform of modal coordinates
η	Modal coordinates
λ	Eigenvalue
ξ	Modal damping ratio
ρ	Density
$\boldsymbol{\Phi}$	Modal matrix
ϕ	Modal shape vector
ω	Angular frequency in rad/s
$\Im$	Imaginary part

CB	Craig-Bampton
CB-IP	Craig-Bampton Interface Preserving
CMS	Component Mode Synthesis
CPT	Connection Point Constraints
DOF	Degree of Freedom
EMA	Experimental Modal Analysis
FBS	Frequency Based Substructuring
FE	Finite Element
FRF	Frequency Response Function
MAC	Modal Assurance Criterion
MCFS	Modal Constraints for Fixture and Subsytstem
SEM	Society for Experimental Mechanics

Indices

a	Accelerance
b	Body DOF
c	Connection/Coupling DOF
d	Displacement
e	Element
f	Related to external forces
g	Related to connection forces
k	Kept
meas	Measurement points
mod	Modal
q	Physical
r	Residual
s	Substructure
tot	Total system
ts	Transmission simulator
u	Input
v	Velocity, mobility
y	Output
ω	Frequency Domain

Superscripts

$\bar{\ }$	Coupled
$\dot{\ }$	Time derivative
$\tilde{\ }$	Transformed
$+$	Pseudo-inverse
$*$	Complex conjugate

List of Figures

1.1 General idea of dynamic substructuring 1
2.1 Coupling of two substructures 5
2.2 Scheme of the Transmission Simulator 12
3.1 Decoupling scheme of two beams 23
3.2 Phase of the decoupled beam's direct receptance FRF 23
3.3 Magnitude of the decoupled beam's direct receptance FRF 23
3.4 Coupling scheme of two beams with the transmission simulator 24
3.5 Results for the decoupled beam A with CPT 25
3.6 Results for the coupled beam AB with CPT 26
3.7 Results for the decoupled beam A with MCFS 26
3.8 Results for the coupled beam AB with MCFS 27
3.9 Results for the coupled beam AB with MCFS for different modes 27
4.1 The substructuring task 30
4.2 FE model of the one-bladed hub 31
4.3 FE model of the hub 32
4.4 FE model of the three-bladed hub 32
4.5 Measurement setup 33
4.6 Attachment of the stinger 33
4.7 Spread between blades 35
4.8 Effect of the stinger 35
4.9 Impassivity due to noise 36
4.10 Non-linearities in the blades 36
4.11 Deviations between 400 Hz and 600 Hz 37
4.12 Chirp measurements of the three-bladed hub 38
4.13 Comparison of measurement data and identified models for a one-bladed hub 39
4.14 MAC value comparison for the one-bladed hubs 40
4.15 Comparison of measurement data and identified models for the three-bladed hub 41
4.16 MAC value comparison for the identified three-bladed hub 42
4.17 Direct accelerance FRF of the three-bladed hub for the input/output location 20 44
4.18 Direct accelerance FRF of the three-bladed hub for the input/output location 24 45
4.19 MAC value comparison for the substructured three-bladed hub 47
B.1 Mode shapes of the coupled system 60

List of Tables

4.1 Component masses of the rotor 30
4.2 Properties of the FE models 30
4.3 Specifications of the measurement equipment 31
4.4 Identified resonance frequencies for the one-bladed hub 39
4.5 Identified modal damping for the one-bladed hubs 40
4.6 Modal parameters of first five flexible mode groups for the three-bladed hub 46
4.7 Errors of the modal parameters of first five flexible mode groups for the three-bladed hub . . . 46
B.1 Identified resonance frequencies for structure A and all models. 56
B.2 Identified damping for structure A and all models 56
B.3 Identified resonance frequencies for structure B and all models 57
B.4 Identified damping ratios for structure B and all models 57
B.5 Identified resonance frequencies for structure C and all models 58
B.6 Identified damping ratios for structure C and all models 58
B.7 Modal parameter for the other substructured models of the three-bladed hub 59

Contents

Abstract **v**

Zusammenfassung **v**

Preface **vii**

Acknowledgements **vii**

Nomenclature **ix**

List of Figures **xi**

List of Tables **xi**

Contents **xiii**

1 Introduction **1**
1.1 Background 1
1.2 Purpose and Limitations 2
1.3 Outline 3

2 Theory **4**
2.1 Coupling of Substructures 4
2.1.1 The Physical Domain 4
2.1.2 The Modal Domain 6
2.1.3 The Frequency Domain 7
2.1.4 The State-Space Domain 8
2.2 The Transmission Simulator 11
2.2.1 The Transmission Simulator Concept 11
2.2.2 The Modal Domain 13
2.2.3 Connection Point Constraints 13
2.2.4 Modal Constraints for Fixture and Subsystem 14
2.2.5 The Frequency Domain 15
2.2.6 The State-Space Domain 16
2.3 Receptance, Mobility and Accelerance FRFs 18
2.4 The Domain Transformations 19
2.5 System Identification of Physical Models 20
2.6 The Modal Assurance Criterion 20

3 The Beam Example **22**
3.1 Decoupling 22
3.2 Utilisation of a Transmission Simulator 24
3.2.1 Coupling with CPT 24
3.2.2 Coupling with MCFS 25
3.2.3 Remarks 28

4 Application to the Ampair 600 Wind Turbine **29**
4.1 Dynamic Substructuring of the Benchmark Wind Turbine 29
4.2 The Substructuring Task 29
4.3 Finite Element Models 30
4.4 Experimental Setup 31
4.5 Analysis of the Measurements 34
4.6 System Identification 37
4.6.1 The One-bladed Hub 37

4.6.2 The Three-bladed Hub 41
4.7 Substructuring Results 41
4.8 Discussion 48

5 Conclusion and Future Work **50**

References **51**

A Appendix to the Theory Chapter **54**
A.1 Jetmundsen's formulation 54
A.2 Woodbury matrix identity 55

B Appendix to the Experimental Results **56**
B.1 Identified Modal Parameters for the One-Bladed Hubs 56
B.2 Substructuring Results 59
B.3 Mode Shapes of the Three-Bladed Hub 59

1 Introduction

In this chapter, an introduction to dynamic substructuring is given followed by challenges associated with experimentally derived models. Next, the transmission simulator is shortly described. Furthermore, the purpose and limitations of the work at hand are given. The chapter concludes with an outline of the report.

1.1 Background

Dynamic substructuring is the idea of dividing complex structures into simpler components, which can be analysed efficiently and in detail [1]. The dynamics of the substructures are then coupled together to obtain a model for the assembled structure. Local behaviours can typically be investigated better with the substructure models since the model of the whole structure is likely to be coarser. Furthermore, dynamic substructuring is highly beneficial and widely used if the full structure is in fact an assembly of parts designed by separate project groups. Then, the substructures can be analysed independent of the other substructures and different modelling approaches may be applied, as Finite Element (FE) models or exerimental models.

Dynamic substructuring can be used in FE calculations for model order reduction where components are represented by a reduced set of generalised coordinates rather than by their detailed discretisation. FE models will subsequently be denoted analytical models. In some cases however, certain substructures cannot be modelled well due to unknown material properties or complex geometries [2]. Thus, recent years have seen an interest in coupling experimentally derived models with analytical ones. To achieve more progress in this research field, the Society for Experimental Mechanics (SEM) Dynamic Substructuring Focus Group chose to use a common testbed: the Ampair A600 wind turbine [3]. This structure is a rather simple structure, yet presenting ample opportunities for experimental dynamics substructuring.

The process of dynamic substructuring relies on enforcement of the compatibility and equilibrium at component interfaces as sketched in Figure 1.1. In their paper [1], de Klerk et al. provided a detailed overview on the topic including different methods for dynamic substructuring. The authors distinguish between primal and dual coupling in the physical, frequency, and modal domain. In primal coupling, a unique set of degrees of freedom (DOFs) is chosen to describe the coupled interface's motion, whereas equilibrium at the interface is enforced a-priori for dual coupling. Only primal coupling will be used in the present thesis.

Dynamic substructuring in the modal domain is known as Component Mode Synthesis (CMS). In CMS, the motion of the substructures is described by a reduced set of mode shapes. This method is widely used for synthesizing both experimentally derived and FE models. Different modes and basis vectors can be chosen to replicate the vibration. Most commonly, the Craig-Bampton representation is used for FE models, and free-free mode shapes are utilized when it comes to experimental models. Introductions to CMS are given e.g. by Craig and Kurdila [4] and by Meirovitch [5].

In Frequency-Based Substructuring (FBS), Frequency Response Functions (FRFs) are coupled directly and was first formulated by Bishop and Johnson [6]. It gained popularity with the improved formulation of Jetmundsen et al. [7]. FBS may be beneficial if measured FRFs are coupled, avoiding the need of system identification, yet measurement errors are often amplified in the coupling procedure.

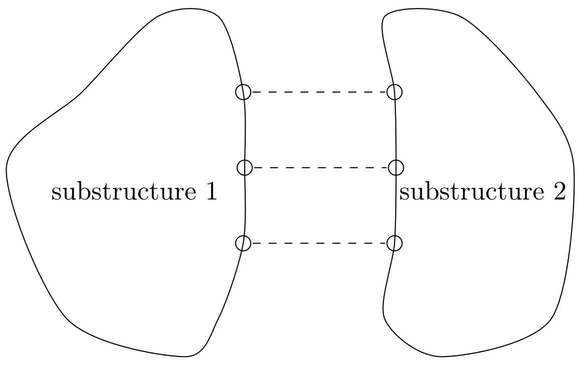

Figure 1.1: *Coupling of two general substructures. The interface between the substructures consists of three connection points.*

In this thesis, another substructuring method utilizing state-space models will be applied. State-space synthesis as used here is a rather new concept and was introduced by Sjövall in the last decade [8, 9]. A similar approach was proposed earlier by Su and Juang [10]. In state-space coupling, first-order systems are coupled, allowing for the wide field of first-order system identification methods such as subspace identification [11, 12].

Common to all experimental substructuring techniques is a need for high-quality data. CMS and state-space synthesis further require models of that data obeying physical constraints. These constraints may be violated by measurement errors such as noise. By directly decoupling measured FRFs, those constraints cannot be enforced which may yield wrong results after the coupling procedure. A second-order modal model with real eigenvectors includes features that have to be explicitly enforced for the more general state-space models. One crucial feature is Newton's second law which is essential for mechanical structures. Liljehren extensively applied state-space coupling and made a contribution to the system identification procedure with respect to dynamic substructuring (e.g. [13]).

Even though the concept of dynamic substructuring is straightforward, imposing the compatibility and equilibrium conditions on experimentally derived models is fraught with problems. For instance, not all DOFs at the interface can be measured as would be needed to enforce strict compatibility. For some structures, the actual connection points are not accessible at all. Moreover, experimental substructuring is typically feasible using only a small number of connection points, which may not be an adequate replication of the actual interface [14].

As a remedy, the transmission simulator technique was introduced by Allen, Mayes, and their co-workers [2, 15]. The transmission simulator is a well-modelled additional structure both available as physical specimen and analytical model. The physical part is joined to the structure of interest. Then, the compound structure is measured, and system identification is performed. To obtain a valid model for the structure of interest, the effect of the transmission simulator has to be removed from the identified model which is done by coupling the negative analytical model of the transmission simulator. Among the advantages of this technique is the avoidance of measuring the connection DOFs at the cost of an additional decoupling step. Instead, the measurement points on the transmission simulator are coupled to the exact same points of the analytical transmission simulator model.

Two different coupling conditions can be applied in this method, namely Connection Point Constraints (CPT) and Modal Constraints for Fixture and Subsystem (MCFS). The first estimates information on the connection points' motion using measurements points of the transmission simulator. The second method enforces the coupling conditions using these measurement points instead of the interface. To the author's knowledge, the transmission simulator was only applied to FBS and CMS (see e.g. [16] for a summary of both methods). Further, the methodology was tested on structures including the benchmark wind turbine by several research groups (see e.g. [17, 18]).

1.2 Purpose and Limitations

The goal of this work is to transfer the transmission simulator concept to state-space coupling in order to combine the benefits of both methods. At the point of writing, a similar approach has not been found in literature. Thus, this method will be introduced in the present work. First, removing the influence of one system from another in terms of state-space models will be derived. Both CPT and MCFS will be used as coupling constraints. Then, all methods will be verified by means of a simple theoretical beam example before experimental-analytical substructuring is performed on the wind turbine. Here, only MCFS will be used since these conditions show better results for experimental substructuring. The goal is to obtain a model of the rotor using the hub as transmission simulator. To achieve this, three blades will be attached to the hub and measured separately. Then, the three experimentally derived models are coupled with two negative analytical hub models. The coupled model will be compared with the measured rotor and its FE model. Further, the measurements will be carried out with different types of excitation to find the best model possible.

For the analytical representation of the transmission simulator, only free-free mode shapes will be utilized. Other approaches like the Craig-Bampton transmission simulator [19] are out of the scope of this thesis. Furthermore, it would be of interest to compare the results obtained with the transmission simulator to results obtained by coupling the blades directly to the hub. This was not done in this thesis but an attempt of this approach has been performed previously [20]. The FE model of the hub is not experimentally verified, only the density properties are modified such that the model replicates the measured weight. Since the flexible modes of the hub are far above the frequency range of interest, this modification is believed to be sufficient. Additionally, the state-space synthesis is not generalised for an arbitrary number of systems. Coupling of multiple models is performed in subsequent steps, combining two systems at a time.

1.3 Outline

The report is structured in five chapters. This introduction is followed by an extensive theory chapter. First, dynamic substructuring in different domains are explained in Section 2.1, and the transmission simulator is elaborated on in Section 2.2. Remarks on the transformation between models, system identification, and the Modal Assurance Criterion are given in Sections 2.3 to 2.6. Afterwards, the different substructuring methods are applied to a simple beam example in Chapter 3. This includes remarks on decoupling in Section 3.1 and the transmission simulator in Section 3.2, both with CPT and MCFS. Chapter 4 elaborates on the experimental results obtained with the wind turbine. The chapter starts with a brief literature overview in Section 4.1. Next, the FE models used are described in Section 4.3, and the measurements and the system identification are addressed in Sections 4.4 to 4.6. The results of the substructuring are finally presented in Section 4.7, followed by a discussion in Section 4.8. The work concludes with remarks and states ideas on future research work to further promote state-space experimental-analytical substructuring in Chapter 5.

2 Theory

In the following chapter, the four different dynamic substructuring methods physical coupling, CMS, FBS, and state-space synthesis will be explained and derived in parts. The notation of de Klerk et al. [1] is used wherever possible but sometimes changed to avoid confusion with the state-space notation. Subsequently, the concept of the transmission simulator is explained, including a brief review of the current literature. This technique is then derived for CMS following the paper of Allen et al. [21] and applied to FBS. Finally, the transmission simulator is developed for state-space synthesis. Both CPT and MCFS are applied as coupling constraints. The chapter also includes transformations between the models and their domains and concludes with remarks on the system identification procedure and the Modal Assurance Criterion.

2.1 Coupling of Substructures

In this section, dynamic substructuring is explained in the physical, modal, frequency, and state-space domain.

2.1.1 The Physical Domain

In the physical domain, the motion of a linear, discretised, non-gyroscopic, and non-circulatory multiple-degrees-of-freedom system with viscous damping is described by the differential equation [4]

$$\mathbf{M}^{(s)}\ddot{q}^{(s)}(t) + \boldsymbol{V}^{(s)}\dot{q}^{(s)}(t) + \boldsymbol{K}^{(s)}q^{(s)}(t) = f^{(s)}(t) + g^{(s)}(t) \tag{2.1}$$

with the mass, damping, and stiffness matrices $\boldsymbol{M}$, $\boldsymbol{V}$, and $\boldsymbol{K}$, respectively. $q^{(s)}$ stands for the displacements, f and g represent external and connection forces between the substructures, respectively [1]. The superscript s indicates the substructure's index.

The equations of multiple, still uncoupled substructures can be compactly written in block diagonal form as

$$\boldsymbol{M}\ddot{q}(t) + \boldsymbol{V}\dot{q}(t) + \boldsymbol{K}q(t) = f(t) + g(t) \tag{2.2}$$

with

$$\boldsymbol{M} = \begin{bmatrix} \boldsymbol{M}^{(1)} & & \\ & \ddots & \\ & & \boldsymbol{M}^{(h)} \end{bmatrix}, \qquad \boldsymbol{V} = \begin{bmatrix} \boldsymbol{V}^{(1)} & & \\ & \ddots & \\ & & \boldsymbol{V}^{(h)} \end{bmatrix}, \qquad \boldsymbol{K} = \begin{bmatrix} \boldsymbol{K}^{(1)} & & \\ & \ddots & \\ & & \boldsymbol{K}^{(h)} \end{bmatrix},$$

$$f = \begin{bmatrix} f^{(1)} \\ \vdots \\ f^{(h)} \end{bmatrix}, \quad g = \begin{bmatrix} g^{(1)} \\ \vdots \\ g^{(h)} \end{bmatrix},$$

and h being the number of substructures.

To couple the substructures, two conditions have to be enforced. First, the coupling DOFs at the interface between the substructures, indicated by the subscript c, have the same displacement when coupled. This condition is dubbed compatibility condition. Secondly, the connection forces cancel out, which is called equilibrium condition. Mathematically expressed, the compatibility condition for two adjacent substructures 1 and 2 is

$$q_c^{(1)} = q_c^{(2)}, \tag{2.3}$$

and the equilibrium condition is

$$f_c = f_c^{(1)} + g_c^{(1)} + f_c^{(2)} + g_c^{(2)} = f_c^{(1)} + f_c^{(2)} \tag{2.4}$$

or

$$0 = g_c^{(1)} + g_c^{(2)}. \tag{2.5}$$

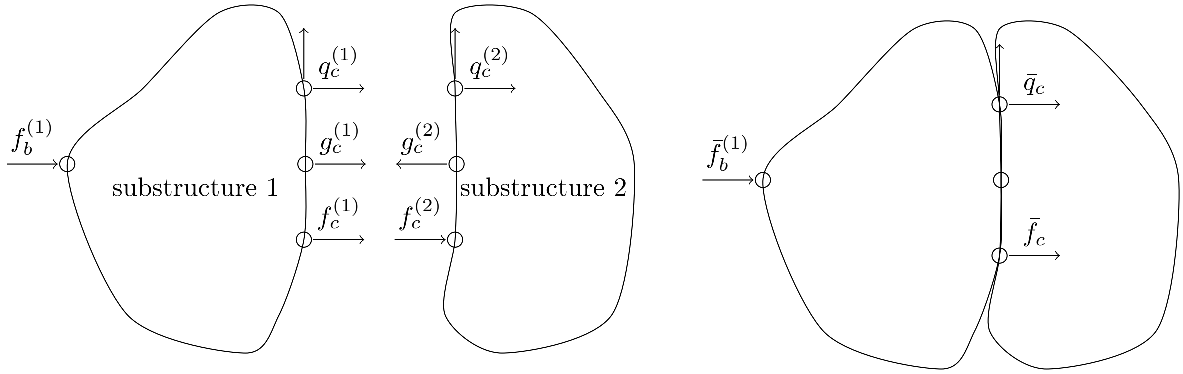

Figure 2.1: *Coupling of two substructures. The interface between the substructures consists here of three points. The interface's motion is described by the substructure coordinates* $q_c^{(s)}$ *and is influenced by the external and connection forces* $f_c^{(s)}$ *and* $g_c^{(s)}$*, respectively. The forces are only exemplified for one connection point. Furthermore, the substructure 1 is excited by an external force on a body DOF* $f_b^{(1)}$*. In the coupled configuration, the connection forces cancel out and the motion is now described in terms of a reduced set of coordinates, denoted* $\bar{q}_c$*. The coupled structure is excited by external forces at the interface,* $\bar{f}_c$*, and at a body DOF,* $\bar{f}_b$*.*

Equations (2.3) and (2.5) can be generalised for more adjacent substructures and for all interfaces in the structure. In matrix notation, this is expressed as

$$\boldsymbol{E}q = 0 \tag{2.6}$$

and

$$\boldsymbol{L}^T g = 0. \tag{2.7}$$

If the coupling DOFs match on all adjacent substructures, the compatibility matrix $\boldsymbol{E}$ has only 1, 0 and -1 as entries and is called a signed Boolean matrix. This is the case e.g. for FE models with consistent meshes and will be the case in the present thesis. Under those circumstances, the matrix $\boldsymbol{L}$ is also a Boolean matrix. The coupled system can thus be described with three equations, denoted as the three-field formulation [1],

$$\begin{cases} \boldsymbol{M}\ddot{q}(t) + \boldsymbol{V}\dot{q}(t) + \boldsymbol{K}q(t) = f(t) + g(t) \\ \boldsymbol{E}q = 0 \\ \boldsymbol{L}^T g = 0. \end{cases} \tag{2.8}$$

De Klerk et al. [1] distinguish between primal and dual coupling. In this work, only primal coupling will be considered. Therefore, a unique set of DOFs $\bar{q}$ for the coupled structure is chosen as

$$q = \boldsymbol{L}\bar{q}. \tag{2.9}$$

Thus, the matrix $\boldsymbol{L}$ localizes the coupling DOFs of the substructures $q^{(s)}$ in the global set of DOFs $\bar{q}$ of the coupled system. The coupling procedure until now is depicted in Figure 2.1.

Using the global coordinates, the compatibility equation becomes

$$\boldsymbol{E}q = \boldsymbol{E}\boldsymbol{L}\bar{q} = 0. \tag{2.10}$$

Since the vector $\bar{q}$ is in general not equal to zero, $\boldsymbol{L}$ must be the nullspace of $\boldsymbol{E}$ in order to fulfil the equation,

$$\boldsymbol{L} = null(\boldsymbol{E}). \tag{2.11}$$

Now, the coupled system can be written as

$$\begin{cases} \boldsymbol{M}\boldsymbol{L}\ddot{\bar{q}}(t) + \boldsymbol{V}\boldsymbol{L}\dot{\bar{q}}(t) + \boldsymbol{V}\boldsymbol{L}\bar{q}(t) = f(t) + g(t) \\ \boldsymbol{L}^T g = 0. \end{cases} \tag{2.12}$$

Multiplying the first equation from the left by $\boldsymbol{L}^T$ and using the information of the second, the equation of motion for a coupled system is obtained as

$$\bar{\boldsymbol{M}}\ddot{\bar{q}}(t) + \bar{\boldsymbol{V}}\dot{\bar{q}}(t) + \bar{\boldsymbol{K}}\bar{q}(t) = \bar{f}(t) \tag{2.13}$$

with

$$\bar{\boldsymbol{M}} = \boldsymbol{L}^T\boldsymbol{M}\boldsymbol{L}, \quad \bar{\boldsymbol{V}} = \boldsymbol{L}^T\boldsymbol{V}\boldsymbol{L}, \quad \bar{\boldsymbol{K}} = \boldsymbol{L}^T\boldsymbol{K}\boldsymbol{L}, \quad \bar{f} = \boldsymbol{L}^T f. \tag{2.14}$$

2.1.2 The Modal Domain

Instead of using the physical DOFs to describe the motion of a structure, modal coordinates η can be utilized. To this end, the coordinate transformation

$$q = \boldsymbol{\Phi}\eta \tag{2.15}$$

is introduced. The matrix $\boldsymbol{\Phi}$ may contain any mode shape vector ϕ of the structure, e.g. constraint modes or normal modes such as free normal modes or fixed interface normal modes. The reader is referred to Craig and Kurdila [4] for a thorough explanation of these and other modes. In this thesis, only free normal modes will be used. A discretized system described by n_q physical DOFs has also n_q modes. Normally, only a subset of the mode shapes are taken into account yielding a reduced order model. More on reduced order models can be found in the books of Craig and Kurdila [4] and Meirovitch [5].

Coupling in the modal domain, dubbed CMS, may involve both experimental and FE models. Experimentally derived modal models are usually obtained using Experimental Modal Analysis (EMA), whereas modal FE models are obtained by solving the eigenvalue problem of a FE model.

If the coordinate transformation (2.15) is used with $\boldsymbol{\Phi}$ containing mass normalised modes, the following modal model

$$\boldsymbol{M}_{mod}\ddot{\eta}(t) + \boldsymbol{V}_{mod}\dot{\eta}(t) + \boldsymbol{K}_{mod}\eta(t) = f_{mod}(t) + g_{mod}(t) \tag{2.16}$$

with

$$\begin{aligned}
\boldsymbol{M}_{mod} &= \boldsymbol{\Phi}^T\boldsymbol{M}\boldsymbol{\Phi} = \boldsymbol{I}, \\
\boldsymbol{V}_{mod} &= \boldsymbol{\Phi}^T\boldsymbol{V}\boldsymbol{\Phi} = \begin{bmatrix} \ddots & & \\ & 2\omega_i\xi_i & \\ & & \ddots \end{bmatrix} \\
\boldsymbol{K}_{mod} &= \boldsymbol{\Phi}^T\boldsymbol{K}\boldsymbol{\Phi} = \begin{bmatrix} \ddots & & \\ & {\omega_i}^2 & \\ & & \ddots \end{bmatrix} \\
f_{mod} &= \boldsymbol{\Phi}^T f, \quad g_{mod} = \boldsymbol{\Phi}^T g.
\end{aligned}$$

is obtained, where ω_i is the i-th resonance frequency of the system in rad/s and ξ_i is the associated modal damping ratio. The equations hold only if the matrices $\boldsymbol{M}$, $\boldsymbol{V}$, and $\boldsymbol{K}$ are symmetric.

Non-normalised mode vectors $\tilde{\boldsymbol{\Phi}}$ yield the matrices

$$\boldsymbol{M} = \begin{bmatrix} \ddots & & \\ & m_{mod,i} & \\ & & \ddots \end{bmatrix}, \quad \boldsymbol{V} = \begin{bmatrix} \ddots & & \\ & 2m_{mod,i}\omega_i\xi_i & \\ & & \ddots \end{bmatrix}, \quad \boldsymbol{K} = \begin{bmatrix} \ddots & & \\ & m_{mod,i}{\omega_i}^2 & \\ & & \ddots \end{bmatrix}, \tag{2.17}$$

with $m_{mod,i} \neq 1$. The mode vector can then be mass normalised with

$$\phi_i = \sqrt{\frac{1}{m_{mod,i}}}\tilde{\phi}_i. \tag{2.18}$$

In the following, the truncation of a modal model will be investigated. The transformation (2.15) can be partitioned such that

$$q = \begin{bmatrix} \boldsymbol{\Phi}_k & \boldsymbol{\Phi}_r \end{bmatrix} \begin{Bmatrix} \eta_k \\ \eta_r \end{Bmatrix}, \tag{2.19}$$

where k and r stand for the kept and the neglected residual modes, respectively. Since modal transformations yield diagonal matrices, the following relation

$$\boldsymbol{\Phi}_k^T \boldsymbol{M} \boldsymbol{\Phi}_k \ddot{\eta}_k + \boldsymbol{\Phi}_k^T \boldsymbol{M} \boldsymbol{\Phi}_r \ddot{\eta}_r + \boldsymbol{\Phi}_k^T \boldsymbol{V} \boldsymbol{\Phi}_k \dot{\eta}_k + \boldsymbol{\Phi}_k^T \boldsymbol{V} \boldsymbol{\Phi}_r \dot{\eta}_r + \boldsymbol{\Phi}_k^T \boldsymbol{K} \boldsymbol{\Phi}_k \eta_k + \boldsymbol{\Phi}_k^T \boldsymbol{K} \boldsymbol{\Phi}_r \eta_r = \boldsymbol{\Phi}_k^T f + \boldsymbol{\Phi}_k^T g \tag{2.20}$$

holds. Introducing the residual force r, which replaces the terms associated with the residual modes η_r, the reduced order equation of motion is

$$\begin{aligned} \boldsymbol{\Phi}_k^T \boldsymbol{M} \boldsymbol{\Phi}_k \ddot{\eta}_k + \boldsymbol{\Phi}_k^T \boldsymbol{V} \boldsymbol{\Phi}_k \dot{\eta}_k + \boldsymbol{\Phi}_k^T \boldsymbol{K} \boldsymbol{\Phi}_k \eta_k &= \boldsymbol{\Phi}_k^T f + \boldsymbol{\Phi}_k^T g - \boldsymbol{\Phi}_k^T \left(\boldsymbol{M} \boldsymbol{\Phi}_r \ddot{\eta}_r + \boldsymbol{V} \boldsymbol{\Phi}_r \dot{\eta}_r + \boldsymbol{K} \boldsymbol{\Phi}_r \eta_r \right) \\ &= \boldsymbol{\Phi}_k^T f + \boldsymbol{\Phi}_k^T g - \boldsymbol{\Phi}_k^T r(t). \end{aligned} \tag{2.21}$$

Due to the orthogonality of the mode shapes, $\boldsymbol{\Phi}_k^T r(t) = 0$ holds. Hence, the residual force r is zero in the reduced space. Subsequently, $\boldsymbol{\Phi}$ will be used for the modal transformation matrix, irrespective of how many modes are taken into consideration.

Coupling in the modal domain is done analogously to the physical domain. Here, the modal mass, stiffness, and damping matrices of all substructures are compactly written in block diagonal form to obtain the first equation of the three-field formulation (2.8). The compatibility and equilibrium equations are expressed as

$$\boldsymbol{E} q = \boldsymbol{E} \boldsymbol{\Phi} \eta = \boldsymbol{E}_{mod} \eta = 0 \tag{2.22}$$

$$\boldsymbol{L}^T \boldsymbol{\Phi}^T g = \boldsymbol{L}_{mod}^T g_{mod} = 0, \tag{2.23}$$

and a unique set of coordinates is chosen to be

$$\eta = \boldsymbol{L}_{mod} \bar{\eta} \tag{2.24}$$

with

$$\boldsymbol{L}_{mod} = null \left(\boldsymbol{E}_{mod} \right). \tag{2.25}$$

Multiplying the equation of motion of the uncoupled system by $\boldsymbol{L}_{mod}^T$ and incorporating both the equilibrium condition and the new coordinates, the coupled modal system is described by

$$\bar{\boldsymbol{M}}_{mod} \ddot{\bar{\eta}} + \bar{\boldsymbol{V}}_{mod} \dot{\bar{\eta}} + \bar{\boldsymbol{K}}_{mod} \bar{\eta} = \bar{f}_{mod} \tag{2.26}$$

with

$$\bar{\boldsymbol{M}}_{mod} = \boldsymbol{L}_{mod}^T \boldsymbol{M}_{mod} \boldsymbol{L}_{mod}, \quad \bar{\boldsymbol{V}}_{mod} = \boldsymbol{L}_{mod}^T \boldsymbol{V}_{mod} \boldsymbol{L}_{mod}, \quad \bar{\boldsymbol{K}}_{mod} = \boldsymbol{L}_{mod}^T \boldsymbol{K}_{mod} \boldsymbol{L}_{mod}, \quad \bar{f}_{mod} = \boldsymbol{L}_{mod}^T f_{mod}.$$

2.1.3 The Frequency Domain

The equation of motion (2.1) expressed in the time domain can also be transformed to the frequency domain. Here, the Fourier transform of the displacement Q and of the forces F and G are used. The mass, stiffness, and damping properties are combined in the dynamic stiffness matrix $\boldsymbol{Z}$. The three-field formulation is then

$$\begin{cases} (-\omega^2 \boldsymbol{M} + i\omega \boldsymbol{V} + \boldsymbol{K}) Q(\omega) = \boldsymbol{Z}(\omega) Q(\omega) = F(\omega) + G(\omega) \\ \boldsymbol{E}_\omega Q(\omega) = 0 \\ \boldsymbol{L}_\omega^T G(\omega) = 0. \end{cases} \tag{2.27}$$

Defining a unique set of DOFs $\bar{Q}$ and performing the same steps as before, the equation of motion of the coupled systems,

$$\bar{\boldsymbol{Z}}(\omega) \bar{Q} = \bar{F}(\omega) \tag{2.28}$$

with

$$\bar{\boldsymbol{Z}} = \boldsymbol{L}_\omega^T \boldsymbol{Z} \boldsymbol{L}_\omega, \quad \bar{F} = \boldsymbol{L}_\omega^T F, \tag{2.29}$$

is obtained. The FRF of the coupled system $\bar{\boldsymbol{H}}$ can then be calculated by inverting $\bar{\boldsymbol{Z}}$.

This formulation is straightforward, although numerical issues are inherent. To obtain coupled FRFs from substructure FRFs, three inversions are needed: two inversions to calculate the dynamic stiffness matrices of the substructures and one to convert the dynamic stiffness matrix of the coupled system to a FRF. An alternative formulation, reducing the number of inversions, was proposed by Jetmundsen et al. [7] and is commonly used to couple FRFs in practice. The derivation of this formula for two substructures can be found in the Appendix A.1. Starting from the FRF of a substructure,

$$\begin{bmatrix} Q_c^{(s)} \\ Q_b^{(s)} \end{bmatrix} = \boldsymbol{H}^{(s)} \begin{bmatrix} F_c^{(s)} \\ F_b^{(s)} \end{bmatrix} \tag{2.30}$$

with

$$\boldsymbol{H}^{(s)} = \begin{bmatrix} \boldsymbol{H}_{cc}^{(s)} & \boldsymbol{H}_{cb}^{(s)} \\ \boldsymbol{H}_{bc}^{(s)} & \boldsymbol{H}_{bb}^{(s)} \end{bmatrix}, \tag{2.31}$$

the FRF of the coupled system

$$\begin{bmatrix} Q_b^{(1)} \\ Q_c \\ Q_b^{(2)} \end{bmatrix} = \bar{\boldsymbol{H}} \begin{bmatrix} F_b^{(1)} \\ F_c \\ F_b^{(2)} \end{bmatrix} \tag{2.32}$$

is obtained as

$$\bar{\boldsymbol{H}} = \begin{bmatrix} \bar{\boldsymbol{H}}_{bb}^{(11)} & \bar{\boldsymbol{H}}_{bc}^{(1c)} & \bar{\boldsymbol{H}}_{bb}^{(12)} \\ \bar{\boldsymbol{H}}_{cb}^{(c1)} & \bar{\boldsymbol{H}}_{cc}^{(cc)} & \bar{\boldsymbol{H}}_{cb}^{(c2)} \\ \bar{\boldsymbol{H}}_{bb}^{(21)} & \bar{\boldsymbol{H}}_{bc}^{(2c)} & \bar{\boldsymbol{H}}_{bb}^{(22)} \end{bmatrix} = \begin{bmatrix} \boldsymbol{H}_{bb}^{(1)} & \boldsymbol{H}_{bc}^{(1)} & \boldsymbol{0} \\ \boldsymbol{H}_{cb}^{(1)} & \boldsymbol{H}_{cc}^{(1)} & \boldsymbol{0} \\ \boldsymbol{0} & \boldsymbol{0} & \boldsymbol{H}_{bb}^{(2)} \end{bmatrix} - \begin{bmatrix} \boldsymbol{H}_{bc}^{(1)} \\ \boldsymbol{H}_{cc}^{(1)} \\ -\boldsymbol{H}_{bc}^{(2)} \end{bmatrix} \left(\boldsymbol{H}_{cc}^{(1)} + \boldsymbol{H}_{cc}^{(2)} \right)^{-1} \begin{bmatrix} \boldsymbol{H}_{bc}^{(1)} \\ \boldsymbol{H}_{cc}^{(1)} \\ -\boldsymbol{H}_{bc}^{(2)} \end{bmatrix}^T \tag{2.33}$$

and

$$\begin{bmatrix} \boldsymbol{H}_{bc}^{(1)} \\ \boldsymbol{H}_{cc}^{(1)} \\ -\boldsymbol{H}_{bc}^{(2)} \end{bmatrix}^T = \begin{bmatrix} \boldsymbol{H}_{cb}^{(1)} & \boldsymbol{H}_{cc}^{(1)} & -\boldsymbol{H}_{cb}^{(2)} \end{bmatrix}. \tag{2.34}$$

The last relation holds only for reciprocal systems (see Section 2.5).

The notation is chosen such that the FRF of a substructure, $\boldsymbol{H}$, is indicated by its index as single superscript. The coupled FRF $\bar{\boldsymbol{H}}$ has two superscripts. The first superscript determines the substructure where the response DOF is localised, and the second describes the substructure with the input. The first and second subscripts distinguish between body (b) and coupling (c) DOFs on the output and input, respectively. For example, $\bar{\boldsymbol{H}}_{cb}^{(c2)}$ is the FRF from an input on a body DOF of substructure 2 to an output on a coupling DOF, whereas $\bar{\boldsymbol{H}}_{bb}^{(12)}$ is the FRF from an input on a body DOF of substructure 2 to an output on a body DOF of substructure 1.

Compared to CMS, the drawback of coupling in the frequency domain is amplification of noise, which can yield unphysical coupling results. If synthesised FRFs of models are used, the results are equal to CMS. Yet, models in the frequency domain circumvent the problems associated with modal truncation, since the influence of high frequency modes is inherent in the measured FRFs [1].

2.1.4 The State-Space Domain

The last dynamic substructuring technique presented in this thesis is the synthesis of state-space models. Here, first-order differential equations expressed in state-space systems are coupled.

For the following derivation, the state vector is defined with physical coordinates, $x = \left\{ q^T \quad \dot{q}^T \right\}^T$. In the present thesis, the inputs are forces connected by the relation $f = \boldsymbol{P}_u u$, where the Boolean matrix $\boldsymbol{P}_u$ localises the input locations among all physical DOFs. The output of a system will be a set of displacements unless stated otherwise, defined by $y = \boldsymbol{P}_y q$, where $\boldsymbol{P}_y$ is again a Boolean selection matrix. With this, a state-space representation of the equation of motion [4] is

$$\begin{cases} \dot{x} = \boldsymbol{A}x + \boldsymbol{B}u \\ y = \boldsymbol{C}x + \boldsymbol{D}u \end{cases} \tag{2.35}$$

with

$$\begin{cases} \boldsymbol{A} = \begin{bmatrix} \boldsymbol{0} & \boldsymbol{I} \\ -\boldsymbol{M}^{-1}\boldsymbol{K} & -\boldsymbol{M}^{-1}\boldsymbol{V} \end{bmatrix} \\ \boldsymbol{B} = \begin{bmatrix} \boldsymbol{0} \\ \boldsymbol{M}^{-1}\boldsymbol{P}_u \end{bmatrix} \\ \boldsymbol{C} = \begin{bmatrix} \boldsymbol{P}_y & \boldsymbol{0} \end{bmatrix}. \end{cases}$$

For both displacement and velocity outputs, the relation $\boldsymbol{D} = \boldsymbol{0}$ holds since forces have only a direct influence on the acceleration, not on velocity or displacements, according to Newton's second law.

Next, the synthesis of two state-space models is explained. The following method was developed by Sjövall [9]. For a thorough derivation, the reader is referred to the licentiate thesis [8], and a shorter version can be found in the paper of Liljerehn [13].

The derivation starts from a general state-space system. The following equations are taken from Sjövall's work [8], following his notation. In a general system, the states are arbitrary, possibly unknown, linear combinations of physical coordinates. However, the inputs and outputs are known and the vectors can be partitioned in entries corresponding to the coupling DOFs and entries corresponding to the remaining body DOFs. The system is then described by

$$u^{(s)} = \begin{Bmatrix} u_c^{(s)} \\ u_b^{(s)} \end{Bmatrix}, \quad y_{(s)} = \begin{Bmatrix} y_c^{(s)} \\ y_b^{(s)} \end{Bmatrix}, \tag{2.36}$$

and

$$\begin{cases} \dot{x}^{(s)} = \boldsymbol{A}^{(s)} x^{(s)} + \boldsymbol{B}^{(s)} u^{(s)} = \boldsymbol{A}^{(s)} x^{(s)} + \begin{bmatrix} \boldsymbol{B}_c^{(s)} & \boldsymbol{B}_b^{(s)} \end{bmatrix} u^{(s)} \\ y^{(s)} = \begin{bmatrix} \boldsymbol{C}_d^{(s)} \\ \boldsymbol{C}_b^{(s)} \end{bmatrix} x^{(s)}. \end{cases} \tag{2.37}$$

The subscript d in $\boldsymbol{C}_d$ stands for displacement outputs at coupling DOFs. Before the systems can be coupled, the state vector x is transformed such that the coupling DOFs are represented by the displacement and the velocity at the interface, $y_c^{(s)}$ and $\dot{y}_c^{(s)}$. This transformation is written as

$$\tilde{x}^{(s)} = \boldsymbol{T}^{(s)} x^{(s)} = \begin{Bmatrix} \dot{y}_c^{(s)} \\ y_c^{(s)} \\ x_b^{(s)} \end{Bmatrix}, \tag{2.38}$$

and the new state-space representation, dubbed coupling form, is

$$\begin{cases} \tilde{\boldsymbol{A}}^{(s)} = \boldsymbol{T}^{(s)} \boldsymbol{A}^{(s)} \boldsymbol{T}^{(s)^{-1}} = \begin{bmatrix} \boldsymbol{A}_{vv}^{(s)} & \boldsymbol{A}_{vd}^{(s)} & \boldsymbol{A}_{vb}^{(s)} \\ \boldsymbol{I} & \boldsymbol{0} & \boldsymbol{0} \\ \boldsymbol{0} & \boldsymbol{A}_{bd}^{(s)} & \boldsymbol{A}_{bb}^{(s)} \end{bmatrix} \\ \tilde{\boldsymbol{B}}^{(s)} = \boldsymbol{T}^{(s)} \boldsymbol{B}^{(s)} = \begin{bmatrix} \boldsymbol{B}_{vv}^{(s)} & \boldsymbol{B}_{vb}^{(s)} \\ \boldsymbol{0} & \boldsymbol{0} \\ \boldsymbol{0} & \boldsymbol{B}_{bb}^{(s)} \end{bmatrix} \\ \tilde{\boldsymbol{C}}^{(s)} = \boldsymbol{C}^{(s)} \boldsymbol{T}^{(s)^{-1}} = \begin{bmatrix} \boldsymbol{0} & \boldsymbol{I} & \boldsymbol{0} \\ \boldsymbol{C}_{bv}^{(s)} & \boldsymbol{C}_{bd}^{(s)} & \boldsymbol{C}_{bb}^{(s)} \end{bmatrix}, \end{cases} \tag{2.39}$$

where the subscript v stands for velocity at the coupling DOF.

The transformation matrix $\boldsymbol{T}$ is found as follows. First, the matrix

$$\boldsymbol{T}_0^{(s)} = \begin{bmatrix} \boldsymbol{C}_d^{(s)} \boldsymbol{A}^{(s)} \\ \boldsymbol{C}_d^{(s)} \\ \boldsymbol{T}_{0,3}^{(s)} \end{bmatrix} \tag{2.40}$$

is defined, with $\boldsymbol{T}_{0,3}$ being an arbitrary nullspace of $\boldsymbol{B}_c^{(s)}$, $\boldsymbol{T}_{0,3}^{(s)} \boldsymbol{B}_c^{(s)} = 0$, such that $\boldsymbol{T}_0^{(s)}$ is non-singular. The final transformation is given by

$$\boldsymbol{T}^{(s)} = \begin{bmatrix} \boldsymbol{C}_d^{(s)} \boldsymbol{A}^{(s)} \\ \boldsymbol{C}_d^{(s)} \\ \boldsymbol{T}_{0,3}^{(s)} \left(\boldsymbol{I} - \boldsymbol{A}^{(s)} \boldsymbol{Z}_{0,1}^{(s)} \boldsymbol{C}_d^{(s)} \right) \end{bmatrix} \tag{2.41}$$

where

$$\boldsymbol{Z}_0^{(s)} = \boldsymbol{T}_0^{(s)^{-1}} \equiv \begin{bmatrix} \boldsymbol{Z}_{0,1}^{(s)} & \boldsymbol{Z}_{0,2}^{(s)} & \boldsymbol{Z}_{0,3}^{(s)} \end{bmatrix}. \tag{2.42}$$

If the number of states is given by n and the number of coupling DOFs by n_c, the size of the identity matrix $\boldsymbol{I}$ and the transformation matrix $\boldsymbol{T}$ is n x n. The partition $\boldsymbol{T}_{0,3}$ is of size $(n-2n_c)$ x n, while $\boldsymbol{Z}_{0,1}$ is of size n x n_c.

Essentially, state-space synthesis of two systems is extracting the second-order differential equation of each model and adding them:

$$\begin{aligned} \boldsymbol{B}_{vv}^{(1)^{-1}} \ddot{y}_c^{(1)} + \boldsymbol{B}_{vv}^{(2)^{-1}} \ddot{y}_c^{(2)} = \boldsymbol{B}_{vv}^{(1)^{-1}} & \left(\boldsymbol{A}_{vv}^{(1)} \dot{y}_c^{(1)} + \boldsymbol{A}_{vd}^{(1)} y_c^{(1)} + \boldsymbol{A}_{vb}^{(1)} y_b^{(1)} + \boldsymbol{B}_{vv}^{(1)} u_c^{(1)} + \boldsymbol{B}_{vb}^{(1)} u_b^{(1)} \right) \\ + \boldsymbol{B}_{vv}^{(2)^{-1}} & \left(\boldsymbol{A}_{vv}^{(2)} \dot{y}_c^{(2)} + \boldsymbol{A}_{vd}^{(2)} y_c^{(2)} + \boldsymbol{A}_{vb}^{(2)} y_b^{(2)} + \boldsymbol{B}_{vv}^{(2)} u_c^{(2)} + \boldsymbol{B}_{vb}^{(2)} u_b^{(2)} \right). \end{aligned} \tag{2.43}$$

To enforce compatibility and equilibrium, the conditions

$$\begin{cases} \ddot{y}_c^{(1)} = \ddot{y}_c^{(2)} = \ddot{y}_c \\ \dot{y}_c^{(1)} = \dot{y}_c^{(2)} = \dot{y}_c \\ y_c^{(1)} = y_c^{(2)} = y_c \\ u_c^{(1)} = u_{c,g}^{(1,2)} + u_{c,f}^{(1)} \\ u_c^{(2)} = -u_{c,g}^{(1,2)} + u_{c,f}^{(2)} \\ \quad u_c = u_c^{(1)} + u_c^{(2)} \end{cases} \tag{2.44}$$

have to be incorporated. Then, the coupled state-space system is obtained after some transformations as

$$\begin{cases} \begin{Bmatrix} \dddot{y}_c \\ \ddot{y}_c \\ \dot{x}_b^{(1)} \\ \dot{x}_b^{(2)} \end{Bmatrix} = \begin{bmatrix} \bar{\boldsymbol{A}}_{vv} & \bar{\boldsymbol{A}}_{vd} & \bar{\boldsymbol{A}}_{vb}^{(1)} & \bar{\boldsymbol{A}}_{vb}^{(2)} \\ \boldsymbol{I} & \boldsymbol{0} & \boldsymbol{0} & \boldsymbol{0} \\ \boldsymbol{0} & \boldsymbol{A}_{bd}^{(1)} & \boldsymbol{A}_{bb}^{(1)} & \boldsymbol{0} \\ \boldsymbol{0} & \boldsymbol{A}_{bd}^{(2)} & \boldsymbol{0} & \boldsymbol{A}_{bb}^{(2)} \end{bmatrix} \begin{Bmatrix} \dot{\bar{y}}_c \\ \bar{y}_c \\ x_b^{(1)} \\ x_b^{(2)} \end{Bmatrix} + \begin{bmatrix} \bar{\boldsymbol{B}}_{vv} & \bar{\boldsymbol{B}}_{vb}^{(1)} & \bar{\boldsymbol{B}}_{vb}^{(2)} \\ \boldsymbol{0} & \boldsymbol{0} & \boldsymbol{0} \\ \boldsymbol{0} & \boldsymbol{B}_{bb}^{(1)} & \boldsymbol{0} \\ \boldsymbol{0} & \boldsymbol{0} & \boldsymbol{B}_{bb}^{(2)} \end{bmatrix} \begin{Bmatrix} \bar{u}_c \\ u_b^{(1)} \\ u_b^{(2)} \end{Bmatrix} \\ \begin{Bmatrix} \bar{y}_c \\ y_b^{(1)} \\ y_b^{(2)} \end{Bmatrix} = \begin{bmatrix} \boldsymbol{0} & \boldsymbol{I} & \boldsymbol{0} & \boldsymbol{0} \\ \boldsymbol{C}_{bv}^{(1)} & \boldsymbol{C}_{bd}^{(1)} & \boldsymbol{C}_{bb}^{(1)} & \boldsymbol{0} \\ \boldsymbol{C}_{bv}^{(2)} & \boldsymbol{C}_{bd}^{(2)} & \boldsymbol{0} & \boldsymbol{C}_{bb}^{(2)} \end{bmatrix} \begin{Bmatrix} \dot{\bar{y}}_c \\ \bar{y}_c \\ x_b^{(1)} \\ x_b^{(2)} \end{Bmatrix} \end{cases} \tag{2.45}$$

with

$$\begin{cases} \quad \boldsymbol{K} = \left(\boldsymbol{B}_{vv}^{(1)} + \boldsymbol{B}_{vv}^{(2)} \right)^{-1} \\ \bar{\boldsymbol{A}}_{vv} = \boldsymbol{B}_{vv}^{(1)} \boldsymbol{K} \boldsymbol{A}_{vv}^{(2)} + \boldsymbol{B}_{vv}^{(2)} \boldsymbol{K} \boldsymbol{A}_{vv}^{(1)} \\ \bar{\boldsymbol{A}}_{vd} = \boldsymbol{B}_{vv}^{(1)} \boldsymbol{K} \boldsymbol{A}_{vd}^{(2)} + \boldsymbol{B}_{vv}^{(2)} \boldsymbol{K} \boldsymbol{A}_{vd}^{(1)} \\ \bar{\boldsymbol{A}}_{vb}^{(1)} = \boldsymbol{B}_{vv}^{(2)} \boldsymbol{K} \boldsymbol{A}_{vb}^{(1)} \\ \bar{\boldsymbol{A}}_{vb}^{(2)} = \boldsymbol{B}_{vv}^{(1)} \boldsymbol{K} \boldsymbol{A}_{vb}^{(2)} \\ \bar{\boldsymbol{B}}_{vv} = \boldsymbol{B}_{\boldsymbol{vv}}^{(1)} \boldsymbol{K} \boldsymbol{B}_{vv}^{(2)} \\ \bar{\boldsymbol{B}}_{vb}^{(1)} = \boldsymbol{B}_{vv}^{(2)} \boldsymbol{K} \boldsymbol{B}_{vb}^{(1)} \\ \bar{\boldsymbol{B}}_{vb}^{(2)} = \boldsymbol{B}_{vv}^{(1)} \boldsymbol{K} \boldsymbol{B}_{vb}^{(2)}. \end{cases} \tag{2.46}$$

The intermediate steps are explained in Sjövall's licentiate thesis [8]. For the equation manipulations, a special case of the Woodbury matrix identity is used, which is derived in the Appendix A.2.

The state-space synthesis of substructures was further translated into de Klerk's general framework by Gibanica [20, 22]. He also revealed numerical difficulties of the state-space approach applied to a complex structure like wind turbines that stem from the choice of the nullspace in the coupling form transformation. As a remedy, all state-space systems will be diagonalised before the transformation is performed, as was suggested by Gibanica.

A very similar approach for state-space coupling was introduced by Su and Juang [10]. However, their method does not yield a minimal model. In contrast, Sjövall avoids the auxiliary states of Su and Juang by using the similarity transformation to coupling form.

The state-space method in the present form is related to both FBS and CMS. On the one hand, the technique uses the same equations for compatibility and equilibrium as FBS but the problem of matrix inversions is reduced as the only inversion needed in equation (2.46) is for the matrix $\boldsymbol{K}$. On the other hand, models are used for the coupling procedure rather than (measured) FRFs. During the system identification, errors can occur and be transferred to the coupled models in both state-space synthesis and CMS. But noise is removed at the same time, diminishing associated errors.

One benefit in using state-space synthesis is the allowance for the wide field of first-order system identification methods. Many currently used system identification algorithms use state-space models. Thus, by applying state-space coupling, the identified model does not have to be transformed to second-order form prior to coupling.

Note that important prerequisites exist for state-space coupling. The systems used for the synthesis need to be passive and physically consistent, which must be ensured during the system identification process. More on this topic can be found in Section 2.5. In addition, one matrix version is needed in state-space coupling (see the derivation by Sjövall [8]). Therefore, the matrix $\boldsymbol{B}_{vv} = \boldsymbol{C}_d \boldsymbol{A} \boldsymbol{B}_c$ must be full rank . However, ${\boldsymbol{B}_{vv}}^{-1}$ corresponds to the interface inertia and it thus exists.

Furthermore, crucial conditions on the inputs and outputs hold for the coupling form transformation. In order to have a full rank transformation matrix, $\boldsymbol{B}_c$ must have full column rank and $\boldsymbol{C}_d$ must have full row rank. These conditions are easily fulfilled if only a few coupling DOFs are used. However, if the state-space synthesis should be used for interfaces containing many connection points, the aforementioned conditions can cause severe difficulties. Up to now, state-space synthesis was not applied to continuous interfaces. Moreover, state-space synthesis is hitherto limited to coupling two systems at a time. Multiple systems need to be coupled step by step.

2.2 The Transmission Simulator

The following sections deal with experimental substructuring using a transmission simulator. First, the concept of the transmission simulator will be explained, including an overview of the literature. Next, decoupling of structures will be derived for CMS and FBS, following the paper of Allen et al. [21]. Then, the transmission simulator will be developed for state-space representations. Furthermore, the two coupling constraints CPT and MCFS will be explained thoroughly for the modal domain [21] and applied to the other methods as well.

2.2.1 The Transmission Simulator Concept

So far, coupling of analytical models has been performed with great success. However, serious difficulties arise in the synthesis of experimental and analytical models [21]. Traditionally, experimental models are obtained with measurements simulating free-free boundary conditions. However, the extracted eigenvectors do not form a good basis for the motion of the coupled system since stress at the interface cannot be represented [14]. Thus, a large number of mode shapes is typically necessary to replicate the interface motion. For analytical models, the mode shape basis can be enlarged with e.g. residual flexibility or constraint modes and fixed-interface modes as in the Craig-Bampton Method [4]. Yet, it is infeasible to measure for instance constraint modes since it would require the application of displacements at distinct DOFs. Previously, researchers have used lumped masses to excite the interface [21], improving the obtained mode shape basis. After the measurements, the mass is removed from the model. Depending on the structure and frequency range of interest, it can be difficult to have a mass which is large enough in order to have the desired effect but is also rigid [21].

Yet another challenge in experimental substructuring is connected to the measurement of the interface. To define the coupling constraints, all DOFs at every connection point must be known. In general, moments and rotations at the connection points are difficult to measure. Moreover, it may be infeasible to mount sensors at those locations. In most cases however, coupling a discrete interface consisting of a rather small number of connection points is practical. The rotational DOFs can be obtained from measurements of points close to the connection points, if the interface is considered to be rigid in this frequency range. Alternatively, multiple connection points with translational information only are coupled [23]. However, few connection points might not represent the actual physical coupling well [14]. Yet, increasing the number of connection points to imitate a continuous interface intensifies the aforementioned difficulties.

The transmission simulator was conceived to remedy the aforementioned roadblocks. This method uses an additional structure, denoted transmission simulator. It can be used to retrieve information about the connection points using the transmission simulator's mode shapes and to relax the coupling constraints due to

Figure 2.2: *Scheme of the Transmission Simulator. The structure of interest A is assembled with the physical transmission simulator TS, and the structure ATS is measured. Then, an analytical model of the transmission simulator is subtracted. In a second coupling step, a second structure B is coupled to arrive at a model for the assembled structure AB.*

model truncation. Instead of measuring the structure of interest in a free-free configuration, it is attached to a second structure, the transmission simulator, and the assembly is measured. The influence of the transmission simulator needs to be removed afterwards, which is done by subtracting its analytical model [21]. The scheme of the transmission simulator idea is depicted in Figure 2.2.

Applying this technique, the measurement of rotations and forces at all connection points can be avoided [14]. The additional mass excites the interface, which brings a larger number of modes into the measured frequency range. The obtained mode shapes will likely resemble the motion of the coupled system more closely than free-free mode shapes, yielding a better modal basis and reducing the number of necessary mode shapes.

The transmission simulator was introduced by Mayes, Allen, and their co-workers [2, 15]. Mayes et al. [2] extended the mass-loading approach by using a flexible structure. To couple the substructures in the frequency domain, Connection Point Constraints (CPT) were used. Thereby, the connection points' motion is inferred using the measurement points on the transmission simulator structure. If the structure is considered to be rigid, the geometry information is sufficient to do so. However, Mayes et al. concluded that it can be beneficial to use mode shapes instead.

In the companion paper [15], the transmission simulator with CPT was used with CMS. Moreover, Allen and Mayes introduced new constraint conditions dubbed Modal Constraints for Fixture and Subsystem (MCFS). Instead of enforcing strict equality, the constraints are applied in a least squares sense yielding a reduced sensitivity towards measurement errors. A short introduction to the topic was provided by Mayes [16], whereas a thorough derivation of both methods was given by Allen et al. [21], including an explanation under which conditions the transmission simulator method works.

In order to replicate the joints at the interface, it is advised to use a part of the actual assembled system as a transmission simulator [21], hence avoiding the need of manufacturing a new structure. However, this choice is not always feasible. Thus, Mayes and Arviso [14] list specifications for the physical design of the transmission simulator as well as for the sensor placement. Note that in their work, the term transmission simulator is used for the first time.

One hindrance of the transmission simulator is the occurrence of indefinite mass or stiffness matrices after decoupling, which yields unphysical results. Allen et al. [24] elaborated on metrics for further investigation as well as possible reasons for this issue. Techniques to overcome this problem were suggested by Mayes et al. [25]. A new extension of the transmission simulator approach is the Craig-Bampton (CB) transmission simulator introduced by Kammer et al. [19], where a CB model is used instead of free-free mode shapes.

At this stage, the reader should note the combinations of transmission simulator methods, which may cause slight confusion. Strictly speaking, one has to distinguish between the free-free and the CB representation of the structure. Furthermore, three different coupling constraints exist which are CPT, MCFS and Motion Relative to the Interface. The latter is commonly abbreviated with CB-IP for Craig-Bampton Interface Preserving. In his thesis, Seeger [26] has given an overview and numerical investigations on all versions. In the present work, the term transmission simulator denotes the use of a free-free representation with MCFS. However, CPT will be explained in the following section and used for the theoretical beam example in Chapter 3.

Alternative ideas to overcome the difficulties in experimental coupling without transmission simulator were suggested by different research groups. One of them is the Virtual Coupling Point and Equivalent Multi-Point Connection [23] where translational measurements close to the actual connection point are necessary. D'Ambrogio and Fregolent suggested extended and mixed interfaces for coupling [27], using interface and body (internal) DOFs.

In summary, the transmission simulator is a good method to remove some of the major obstacles in experimental-analytical coupling. By measuring the structure in a coupled configuration, the extracted mode shapes form a better basis for the system. Connection properties of joints can be included in the model. Since MCFS is applied on the measurement points, the estimate of the connection point displacements and rotations is avoided (see section 2.2.4 for more explanations). Moreover, these constraints allow for a distributed interface since it is implicitly modelled by the transmission simulator mode shapes.

2.2.2 The Modal Domain

Removing the influence of one structure from another is equal to adding a negative representation of the first one to the latter [21]. In the subsequent, this procedure will be dubbed subtraction or decoupling of a system. In the modal domain, decoupling is achieved by adding a system with negative modal mass, damping, and stiffness to the compound structure. In the following, the structure to be subtracted will be denoted transmission simulator (ts) and decoupled from the total system (tot). The uncoupled block diagonal form of both systems is then

$$\begin{bmatrix} \boldsymbol{M}_{mod}^{(tot)} & \mathbf{0} \\ \mathbf{0} & -\boldsymbol{M}_{mod}^{(ts)} \end{bmatrix} \begin{Bmatrix} \ddot{\eta}^{(tot)} \\ \ddot{\eta}^{(ts)} \end{Bmatrix} + \begin{bmatrix} \boldsymbol{V}_{mod}^{(tot)} & \mathbf{0} \\ \mathbf{0} & -\boldsymbol{V}_{mod}^{(ts)} \end{bmatrix} \begin{Bmatrix} \dot{\eta}^{(tot)} \\ \dot{\eta}^{(ts)} \end{Bmatrix} + \begin{bmatrix} \boldsymbol{K}_{mod}^{(tot)} & \mathbf{0} \\ \mathbf{0} & -\boldsymbol{K}_{mod}^{(ts)} \end{bmatrix} \begin{Bmatrix} \eta^{(tot)} \\ \eta^{(ts)} \end{Bmatrix} = \begin{Bmatrix} f_{mod}^{(tot)} \\ f_{mod}^{(ts)} \end{Bmatrix} + \begin{Bmatrix} g_{mod}^{(tot)} \\ g_{mod}^{(ts)} \end{Bmatrix}. \tag{2.47}$$

Applying the coupling conditions, a model of the structure of interest is obtained.

2.2.3 Connection Point Constraints

As stated above, the displacements at the interface need to be known for the coupling process in traditional dynamic substructuring. If the actual connection point cannot be measured, its motion can be estimated from the measurement points' motion using the analytical transmission simulator model. In the FE model, information about all DOFs is available. This approach is called CPT. To succeed, the physical transmission simulator being part of the total structure must have the same motion as its analytical model. In other words, $q_c^{(tot)}$ is unknown as well as $\boldsymbol{\Phi}_c^{(tot)}$, which refers to the partition of the modal matrix including only coupling DOFs. The mode shapes associated with the measurement points, $\boldsymbol{\Phi}_{meas}^{(tot)}$, are measured and the full mode shape matrix of the transmission simulator $\boldsymbol{\Phi}^{(ts)}$ is available from the analytical model.

The motion of the total structure corresponding to the transmission simulator can be expressed in terms of the latter's modal coordinates,

$$\begin{Bmatrix} q_c^{(tot)} \\ q_{meas}^{(tot)} \end{Bmatrix} = \begin{Bmatrix} \boldsymbol{\Phi}_c^{(ts)} \\ \boldsymbol{\Phi}_{meas}^{(ts)} \end{Bmatrix} \eta^{(ts)}. \tag{2.48}$$

The subscript $meas$ refers only to the measurement points on the transmission simulator. It is required that the mode shapes are linearly independent on the chosen measurement point set and that there are at least as many measurement points as modes in the transmission simulator representation [21]. Thus, $\boldsymbol{\Phi}_{meas}^{(ts)}$ has more rows than columns and full column rank. Then, the motion of the total structure's connection point $q_c^{(tot)}$ can be written with

$$\eta^{(ts)} = \left(\boldsymbol{\Phi}_{meas}^{(ts)}\right)^{+} q_{meas}^{(tot)} \tag{2.49}$$

as

$$q_c^{(tot)} = \boldsymbol{\Phi}_c^{(ts)} \left(\boldsymbol{\Phi}_{meas}^{(ts)}\right)^{+} q_{meas}^{(tot)} \tag{2.50}$$

where $^+$ stands for the Moore-Penrose pseudo-inverse. With this estimate, the modified compatibility condition is

$$q_c^{(ts)} - \boldsymbol{\Phi}_c^{(ts)} \left(\boldsymbol{\Phi}_{meas}^{(ts)}\right)^{+} q_{meas}^{(tot)} = 0 \tag{2.51}$$

or in matrix notation

$$\begin{aligned} \begin{bmatrix} \boldsymbol{I} & -\boldsymbol{I} \end{bmatrix} \begin{Bmatrix} q_c^{(tot)} \\ q_c^{(ts)} \end{Bmatrix} &= \begin{bmatrix} \boldsymbol{I} & -\boldsymbol{I} \end{bmatrix} \begin{bmatrix} \boldsymbol{\Phi}_c^{(ts)} \left(\boldsymbol{\Phi}_{meas}^{(ts)}\right)^{+} & \mathbf{0} \\ \mathbf{0} & \boldsymbol{I} \end{bmatrix} \begin{Bmatrix} q_{meas}^{(tot)} \\ q_c^{(ts)} \end{Bmatrix} \\ &= \begin{bmatrix} \boldsymbol{I} & -\boldsymbol{I} \end{bmatrix} \begin{bmatrix} \boldsymbol{\Phi}_c^{(ts)} \left(\boldsymbol{\Phi}_{meas}^{(ts)}\right)^{+} & \mathbf{0} \\ \mathbf{0} & \boldsymbol{I} \end{bmatrix} \begin{bmatrix} \boldsymbol{\Phi}_{meas}^{(tot)} & \mathbf{0} \\ \mathbf{0} & \boldsymbol{\Phi}_c^{(ts)} \end{bmatrix} \begin{Bmatrix} \eta^{(tot)} \\ \eta^{(ts)} \end{Bmatrix} = 0. \end{aligned} \tag{2.52}$$

If the compatibility matrix is defined as

$$\boldsymbol{E}_{CPT} = \begin{bmatrix} \boldsymbol{I} & -\boldsymbol{I} \end{bmatrix} \begin{bmatrix} \boldsymbol{\Phi}_c^{(ts)} \left(\boldsymbol{\Phi}_{meas}^{(ts)}\right)^{+} & \mathbf{0} \\ \mathbf{0} & \boldsymbol{I} \end{bmatrix} \begin{bmatrix} \boldsymbol{\Phi}_{meas}^{(tot)} & \mathbf{0} \\ \mathbf{0} & \boldsymbol{\Phi}_c^{(ts)} \end{bmatrix}, \tag{2.53}$$

the matrix $\boldsymbol{L}_{CPT}$ is calculated as $\boldsymbol{L}_{CPT} = null(\boldsymbol{E}_{CPT})$. $\boldsymbol{\Phi}_{meas}^{(ts)}$ must be well conditioned since its pseudo-inverse is needed for the estimation. For the assessment, the condition number is utilized [28].

2.2.4 Modal Constraints for Fixture and Subsystem

Problems occur if the measurement information is not sufficient for describing the motion of the connection points. A solution to this is the MCFS method. Here, the coupling is enforced by constraining the displacement of all measurement points on the transmission simulator to be equal to the motion of the analytical transmission simulator model which is

$$q_{meas}^{(ts)} = q_{meas}^{(tot)}. \tag{2.54}$$

Note that $q_{meas}^{(ts)}$ and $q_{meas}^{(tot)}$ have the same size since $q_{meas}^{(tot)}$ stands for the measurement points on the part of the total structure that belongs to the transmission simulator and $q_{meas}^{(ts)}$ stands for the displacement of the analytical model at exactly those measurement points.

If there are more measurement points than modes, some coupling conditions will be redundant and may cause problems like lock-down. To avoid such problems, it is desired to relax the constraints and fulfil them in a least squares sense. This is done in terms of the transmission simulator modal matrix $\boldsymbol{\Phi}_{meas}^{(ts)}$, hence the name modal constraints [21]. The pseudo-inverse of the modal matrix is multiplied by equation (2.54),

$$\left(\boldsymbol{\Phi}_{meas}^{(ts)}\right)^{+} q_{meas}^{(ts)} = \eta^{(ts)} = \left(\boldsymbol{\Phi}_{meas}^{(ts)}\right)^{+} q_{meas}^{(tot)} = \left(\boldsymbol{\Phi}_{meas}^{(ts)}\right)^{+} \boldsymbol{\Phi}_{meas}^{(tot)} \eta^{(tot)}. \tag{2.55}$$

The term $\left(\boldsymbol{\Phi}_{meas}^{(ts)}\right)^{+} q_{meas}^{(tot)}$ describes an orthogonal projection of the total systems' motion onto the space spanned by the transmission simulator mode shapes. Again, only the specified measurement points on the transmission simulator are considered. The number of constraints is thereby reduced to the number of modes in the representation of the transmission simulator. If fewer modes than measurement points are considered, the constraints do not enforce strict equality of the displacements but the compatibility condition will be fulfilled in the desired least squares sense.

In matrix notation, the coupling condition is

$$\begin{aligned}\left(\boldsymbol{\Phi}_{meas}^{(ts)}\right)^{+} \begin{bmatrix}\boldsymbol{I}_{meas} & -\boldsymbol{I}_{meas}\end{bmatrix} \begin{Bmatrix} q_{meas}^{(tot)} \\ q_{meas}^{(ts)} \end{Bmatrix} &= \left(\boldsymbol{\Phi}_{meas}^{(ts)}\right)^{+} \begin{bmatrix}\boldsymbol{I}_{meas} & -\boldsymbol{I}_{meas}\end{bmatrix} \begin{bmatrix} \boldsymbol{\Phi}_{meas}^{(tot)} & \boldsymbol{0} \\ \boldsymbol{0} & \boldsymbol{\Phi}_{meas}^{(ts)} \end{bmatrix} \begin{Bmatrix} \eta^{(tot)} \\ \eta^{(ts)} \end{Bmatrix} \\ &= \begin{bmatrix} \left(\boldsymbol{\Phi}_{meas}^{(ts)}\right)^{+} \boldsymbol{\Phi}_{meas}^{(tot)} & -\boldsymbol{I}_{mod} \end{bmatrix} \begin{Bmatrix} \eta^{(tot)} \\ \eta^{(ts)} \end{Bmatrix} = \boldsymbol{E}_{MCFS} \begin{Bmatrix} \eta^{(tot)} \\ \eta^{(ts)} \end{Bmatrix} = 0 \end{aligned} \tag{2.56}$$

and $\boldsymbol{L}_{MCFS} = null(\boldsymbol{E}_{MCFS})$. Here, the identity matrix $\boldsymbol{I}_{meas}$ in the first row has as many rows and columns as there are measurement points, whereas $\boldsymbol{I}_{mod}$ in the second row has as many rows and columns as there are modes in the representation of the transmission simulator.

After the model for the substructure of interest is obtained, it can be coupled to other structures. This can be done using the information of the connection point included in the transmission simulator. Thus, the coupling condition would constrain the negative transmission simulator with the next substructure [21]. However, MCFS can also be applied for the next coupling step, which yields better results. Moreover, it has been recommended to use the same transmission simulator for both structures to be coupled and then removing the transmission simulator twice[1], as was done e.g. in the work of Allen et al. [21]. Thereby, the robustness properties of MCFS can be exploited for the overall coupling procedure.

If the transmission simulator is to be subtracted n_{ts} times from n_{tot} representations of the total systems, the mass, damping, and stiffness matrices are multiplied with n_{ts} and n_{tot} accordingly [16],

$$\begin{aligned}\begin{bmatrix} n_{tot}\boldsymbol{M}_m^{(tot)} & \boldsymbol{0} \\ \boldsymbol{0} & -n_{ts}\boldsymbol{M}_m^{(ts)} \end{bmatrix} \begin{Bmatrix} \ddot{\eta}^{(tot)} \\ \ddot{\eta}^{(ts)} \end{Bmatrix} + \begin{bmatrix} n_{tot}\boldsymbol{V}_m^{(tot)} & \boldsymbol{0} \\ \boldsymbol{0} & -n_{ts}\boldsymbol{V}_m^{(ts)} \end{bmatrix} \begin{Bmatrix} \dot{\eta}^{(tot)} \\ \dot{\eta}^{(ts)} \end{Bmatrix} \\ + \begin{bmatrix} n_{tot}\boldsymbol{K}_m^{(tot)} & \boldsymbol{0} \\ \boldsymbol{0} & -n_{ts}\boldsymbol{K}_m^{(ts)} \end{bmatrix} \begin{Bmatrix} \eta^{(tot)} \\ \eta^{(ts)} \end{Bmatrix} = \begin{Bmatrix} f_m^{(tot)} \\ f_m^{(ts)} \end{Bmatrix} + \begin{Bmatrix} g_m^{(tot)} \\ g_m^{(ts)} \end{Bmatrix}. \end{aligned} \tag{2.57}$$

[1]Even though this statement is not mentioned explicitly, hints can be found in the paper [21]. Furthermore, Randy Mayes, one of the authors, has reported the observation in a conversation.

2.2.5 The Frequency Domain

Now, the constraints CPT and MCFS introduced above will be applied to FBS using the formulation of Jetmundsen et al. Selected equations can be found in the work of Mayes and Arviso [14, 16].

Subtracting of frequency domain models can be done in two ways, denoted Inverse Coupling and Direct Decoupling [27]. Direct Decoupling is the approach of rearranging the coupling equations (2.33) such that the system of interest can be deduced. For instance, the equations can be chosen as

$$\boldsymbol{H}_{cc}^{(1)} = \bar{\boldsymbol{H}}_{cc}^{(cc)} - \bar{\boldsymbol{H}}_{cc}^{(cc)}\left(\bar{\boldsymbol{H}}_{cc}^{(cc)} - \boldsymbol{H}_{cc}^{(2)}\right)^{-1}\bar{\boldsymbol{H}}_{cc}^{(cc)} \tag{2.58}$$

$$\boldsymbol{H}_{bc}^{(1)} = \bar{\boldsymbol{H}}_{bb}^{(12)}\left(\boldsymbol{H}_{cb}^{(2)}\right)^{+}\left(\boldsymbol{H}_{cc}^{(1)} + \boldsymbol{H}_{cc}^{(2)}\right) \tag{2.59}$$

$$\boldsymbol{H}_{cb}^{(1)} = \left(\boldsymbol{H}_{cc}^{(1)} + \boldsymbol{H}_{cc}^{(2)}\right)\left(\boldsymbol{H}_{bc}^{(2)}\right)^{+}\bar{\boldsymbol{H}}_{bb}^{(21)} \tag{2.60}$$

$$\boldsymbol{H}_{bb}^{(1)} = \bar{\boldsymbol{H}}_{bb}^{(11)} + \boldsymbol{H}_{bc}^{(1)}\left(\boldsymbol{H}_{cc}^{(1)} + \boldsymbol{H}_{cc}^{(2)}\right)^{-1}\boldsymbol{H}_{cb}^{(1)}. \tag{2.61}$$

Recall the notation explained in Section 2.1.3. The above equations hold for systems with more body DOFs than coupling DOFs. If $\boldsymbol{H}_{bc}$ and $\boldsymbol{H}_{cb}$ are square, the pseudo-inverse reduces to the inverse of the matrices.

In Inverse Coupling, the negative FRFs of the transmission simulator, $\boldsymbol{H}^{(ts)}$, is coupled to the positive total system's FRFs $\boldsymbol{H}^{(tot)}$. This will be used in the present thesis. Applying CPT, the measurement points' displacements are used to infer the coupling point's displacement according to equation (2.50),

$$\begin{Bmatrix} q_c^{(tot)} \\ q_b^{(tot)} \end{Bmatrix} = \begin{bmatrix} \boldsymbol{\Phi}_c^{(ts)}\left(\boldsymbol{\Phi}_{meas}^{(ts)}\right)^{+} & \boldsymbol{0} \\ \boldsymbol{0} & \boldsymbol{I} \end{bmatrix} \begin{Bmatrix} q_{meas}^{(tot)} \\ q_b^{(tot)} \end{Bmatrix}. \tag{2.62}$$

Accordingly, the forces at the coupling point are obtained with

$$\begin{Bmatrix} f_{meas}^{(tot)} \\ f_b^{(tot)} \end{Bmatrix} = \begin{bmatrix} \left(\boldsymbol{\Phi}_c^{(ts)}\left(\boldsymbol{\Phi}_{meas}^{(ts)}\right)^{+}\right)^{T} & \boldsymbol{0} \\ \boldsymbol{0} & \boldsymbol{I} \end{bmatrix} \begin{Bmatrix} f_c^{(tot)} \\ f_b^{(tot)} \end{Bmatrix}. \tag{2.63}$$

Thus, the measured FRFs

$$\begin{aligned} \begin{Bmatrix} Q_{meas}^{(tot)} \\ Q_b^{(tot)} \end{Bmatrix} &= \boldsymbol{H}^{(tot)} \begin{Bmatrix} F_{meas}^{(tot)} \\ F_b^{(tot)} \end{Bmatrix} \\ &= \begin{bmatrix} \boldsymbol{H}_{meas,meas}^{(tot)} & \boldsymbol{H}_{meas,b}^{(tot)} \\ \boldsymbol{H}_{b,meas}^{(tot)} & \boldsymbol{H}_{b,b}^{(tot)} \end{bmatrix} \begin{Bmatrix} F_{meas}^{(tot)} \\ F_b^{(tot)} \end{Bmatrix} \end{aligned} \tag{2.64}$$

will be transformed to

$$\begin{aligned} \begin{Bmatrix} Q_c^{(tot)} \\ Q_b^{(tot)} \end{Bmatrix} &= \begin{bmatrix} \boldsymbol{\Phi}_c^{(ts)}\left(\boldsymbol{\Phi}_{meas}^{(ts)}\right)^{+} & \boldsymbol{0} \\ \boldsymbol{0} & \boldsymbol{I} \end{bmatrix} \begin{bmatrix} \boldsymbol{H}_{meas,meas}^{(tot)} & \boldsymbol{H}_{meas,b}^{(tot)} \\ \boldsymbol{H}_{b,meas}^{(tot)} & \boldsymbol{H}_{b,b}^{(tot)} \end{bmatrix} \begin{bmatrix} \left(\boldsymbol{\Phi}_c^{(ts)}\left(\boldsymbol{\Phi}_{meas}^{(ts)}\right)^{+}\right)^{T} & \boldsymbol{0} \\ \boldsymbol{0} & \boldsymbol{I} \end{bmatrix} \begin{Bmatrix} F_c^{(tot)} \\ F_b^{(tot)} \end{Bmatrix} \\ &= \begin{bmatrix} \boldsymbol{H}_{c,c}^{(tot)} & \boldsymbol{H}_{c,b}^{(tot)} \\ \boldsymbol{H}_{b,c}^{(tot)} & \boldsymbol{H}_{b,b}^{(tot)} \end{bmatrix} \begin{Bmatrix} F_c^{(tot)} \\ F_b^{(tot)} \end{Bmatrix}. \end{aligned} \tag{2.65}$$

The transmission simulator to be subtracted is represented by the negative FRFs

$$\boldsymbol{H}^{(ts)} = -\begin{bmatrix} \boldsymbol{H}_{c,c}^{(ts)} & \boldsymbol{H}_{c,b}^{(ts)} \\ \boldsymbol{H}_{b,c}^{(ts)} & \boldsymbol{H}_{b,b}^{(ts)} \end{bmatrix}. \tag{2.66}$$

Coupling these two FRF matrices, the system of interest is deduced.

MCFS can be applied similarly. The measurement points' motion and the associated forces will be expressed in modal coordinates,

$$\begin{Bmatrix} \eta^{(tot)} \\ q_b^{(tot)} \end{Bmatrix} = \begin{bmatrix} \left(\boldsymbol{\Phi}_{meas}^{(ts)}\right)^+ & \mathbf{0} \\ \mathbf{0} & \boldsymbol{I} \end{bmatrix} \begin{Bmatrix} q_{meas}^{(tot)} \\ q_b^{(tot)} \end{Bmatrix} \tag{2.67}$$

$$\begin{Bmatrix} \eta^{(ts)} \\ q_b^{(ts)} \end{Bmatrix} = \begin{bmatrix} \left(\boldsymbol{\Phi}_{meas}^{(ts)}\right)^+ & \mathbf{0} \\ \mathbf{0} & \boldsymbol{I} \end{bmatrix} \begin{Bmatrix} q_{meas}^{(ts)} \\ q_b^{(ts)} \end{Bmatrix} \tag{2.68}$$

$$\begin{Bmatrix} f_{meas}^{(tot)} \\ f_b^{(tot)} \end{Bmatrix} = \begin{bmatrix} \left(\left(\boldsymbol{\Phi}_{meas}^{(ts)}\right)^+\right)^T & \mathbf{0} \\ \mathbf{0} & \boldsymbol{I} \end{bmatrix} \begin{Bmatrix} f_{mod}^{(tot)} \\ f_b^{(tot)} \end{Bmatrix} \tag{2.69}$$

$$\begin{Bmatrix} f_{meas}^{(ts)} \\ f_b^{(ts)} \end{Bmatrix} = \begin{bmatrix} \left(\left(\boldsymbol{\Phi}_{meas}^{(ts)}\right)^+\right)^T & \mathbf{0} \\ \mathbf{0} & \boldsymbol{I} \end{bmatrix} \begin{Bmatrix} f_{mod}^{(ts)} \\ f_b^{(ts)} \end{Bmatrix} \tag{2.70}$$

This yields the FRFs

$$\begin{aligned} \begin{Bmatrix} H^{(tot)} \\ Q_b^{(tot)} \end{Bmatrix} &= \begin{bmatrix} \left(\boldsymbol{\Phi}_{meas}^{(ts)}\right)^+ & \mathbf{0} \\ \mathbf{0} & \boldsymbol{I} \end{bmatrix} \begin{bmatrix} \boldsymbol{H}_{meas,meas}^{(tot)} & \boldsymbol{H}_{meas,b}^{(tot)} \\ \boldsymbol{H}_{b,meas}^{(tot)} & \boldsymbol{H}_{b,b}^{(tot)} \end{bmatrix} \begin{bmatrix} \left(\left(\boldsymbol{\Phi}_{meas}^{(ts)}\right)^+\right)^T & \mathbf{0} \\ \mathbf{0} & \boldsymbol{I} \end{bmatrix} \begin{Bmatrix} F_{mod}^{(tot)} \\ F_b^{(tot)} \end{Bmatrix} \\ &= \begin{bmatrix} \boldsymbol{H}_{mod,mod}^{(tot)} & \boldsymbol{H}_{mod,b}^{(tot)} \\ \boldsymbol{H}_{b,mod}^{(tot)} & \boldsymbol{H}_{b,b}^{(tot)} \end{bmatrix} \begin{Bmatrix} F_{mod}^{(tot)} \\ F_b^{(tot)} \end{Bmatrix} \end{aligned} \tag{2.71}$$

for the total system and

$$\begin{aligned} \begin{Bmatrix} H^{(ts)} \\ Q_b^{(ts)} \end{Bmatrix} &= -\begin{bmatrix} \left(\boldsymbol{\Phi}_{meas}^{(ts)}\right)^+ & \mathbf{0} \\ \mathbf{0} & \boldsymbol{I} \end{bmatrix} \begin{bmatrix} \boldsymbol{H}_{meas,meas}^{(ts)} & \boldsymbol{H}_{meas,b}^{(ts)} \\ \boldsymbol{H}_{b,meas}^{(ts)} & \boldsymbol{H}_{b,b}^{(ts)} \end{bmatrix} \begin{bmatrix} \left(\left(\boldsymbol{\Phi}_{meas}^{(ts)}\right)^+\right)^T & \mathbf{0} \\ \mathbf{0} & \boldsymbol{I} \end{bmatrix} \begin{Bmatrix} F_{mod}^{(ts)} \\ F_b^{(ts)} \end{Bmatrix} \\ &= -\begin{bmatrix} \boldsymbol{H}_{mod,mod}^{(ts)} & \boldsymbol{H}_{mod,b}^{(ts)} \\ \boldsymbol{H}_{b,mod}^{(ts)} & \boldsymbol{H}_{b,b}^{(ts)} \end{bmatrix} \begin{Bmatrix} F_{mod}^{(ts)} \\ F_b^{(ts)} \end{Bmatrix} \end{aligned} \tag{2.72}$$

for the negative transmission simulator. To obtain the system of interest, these FRFs can then be coupled as explained in Section 2.1.3. Note the difference in notation between $\boldsymbol{H}^{(ts)}$ and $H^{(ts)}$. The first is the FRF matrix of the transmission simulator, whereas the latter indicates the Fourier transform of the modal coordinates $\eta^{(ts)}$. Accordingly, $F_{mod}^{(ts)}$ stands for the Fourier transform of the modal forces $f_{mod}^{(ts)}$. If a system is to be subtracted n times, the dynamic stiffness matrix is multiplied by that factor, while the FRF is divided by it [14].

2.2.6 The State-Space Domain

In the following, subtracting models in the state-space domain will be derived, and then, CPT and MCFS will be applied. A negative state-space system can be illustrated by the use of the physical state vector $x = \begin{Bmatrix} q^T & \dot{q}^T \end{Bmatrix}^T$. With negative mass, stiffness, and damping, the state-space matrices

$$\begin{cases} \boldsymbol{A} = \begin{bmatrix} \mathbf{0} & \boldsymbol{I} \\ -(-\boldsymbol{M})^{-1}\left(-\boldsymbol{K}^{-1}\right) & -(-\boldsymbol{M})^{-1}\left(-\boldsymbol{V}^{-1}\right) \end{bmatrix} = \begin{bmatrix} \mathbf{0} & \boldsymbol{I} \\ -\boldsymbol{M}^{-1}\boldsymbol{K}^{-1} & -\boldsymbol{M}^{-1}\boldsymbol{V}^{-1} \end{bmatrix} \\ \boldsymbol{B} = \begin{bmatrix} \mathbf{0} \\ -\boldsymbol{M}^{-1}\boldsymbol{P}_u \end{bmatrix} = -\begin{bmatrix} \mathbf{0} \\ \boldsymbol{M}^{-1}\boldsymbol{P}_u \end{bmatrix} \\ \boldsymbol{C} = \begin{bmatrix} \boldsymbol{P}_y & \mathbf{0} \end{bmatrix} \end{cases} \tag{2.73}$$

can be obtained. In other words, it suffices to multiply only the input matrix $\boldsymbol{B}$ by -1.

Instead of adding a negative system, Equation (2.43) could also be modified such that a positive system can be subtracted by changing the plus into a minus. However, the phase of the transmission simulator body DOFs is then inverted which causes wrong results if they are coupled in a later step. This will be shown in Chapter 3.

The CPT can be implemented in the state-space domain similar to the frequency domain. Starting from the identified state-space representation of the measured total system,

$$\begin{cases} \dot{x}^{(tot)} = \boldsymbol{A}^{(tot)} x^{(tot)} + \begin{bmatrix} \boldsymbol{B}_{meas}^{(tot)} & \boldsymbol{B}_b^{(tot)} \end{bmatrix} \begin{Bmatrix} u_{meas}^{(tot)} \\ u_b^{(tot)} \end{Bmatrix} \\ \begin{Bmatrix} y_{meas}^{(tot)} \\ y_b^{(tot)} \end{Bmatrix} = \begin{bmatrix} \boldsymbol{C}_{d,meas}^{(tot)} \\ \boldsymbol{C}_b^{(tot)} \end{bmatrix} x^{(tot)}, \end{cases} \tag{2.74}$$

the inputs and outputs are transformed to

$$\begin{cases} \dot{x}^{(tot)} = \boldsymbol{A}^{(tot)} x^{(tot)} + \begin{bmatrix} \boldsymbol{B}_{meas}^{(tot)} & \boldsymbol{B}_b^{(tot)} \end{bmatrix} \begin{bmatrix} \left(\boldsymbol{\Phi}_c^{(ts)} \left(\boldsymbol{\Phi}_{meas}^{(ts)} \right)^+ \right)^T & \boldsymbol{0} \\ \boldsymbol{0} & \boldsymbol{I} \end{bmatrix} \begin{Bmatrix} u_c^{(tot)} \\ u_b^{(tot)} \end{Bmatrix} \\ \qquad = \boldsymbol{A}^{(tot)} x^{(tot)} + \begin{bmatrix} \boldsymbol{B}_c^{(tot)} & \boldsymbol{B}_b^{(tot)} \end{bmatrix} \begin{Bmatrix} u_c^{(tot)} \\ u_b^{(tot)} \end{Bmatrix} \\ \begin{Bmatrix} y_c^{(tot)} \\ y_b^{(tot)} \end{Bmatrix} = \begin{bmatrix} \boldsymbol{\Phi}_c^{(ts)} \left(\boldsymbol{\Phi}_{meas}^{(ts)} \right)^+ & \boldsymbol{0} \\ \boldsymbol{0} & \boldsymbol{I} \end{bmatrix} \begin{bmatrix} \boldsymbol{C}_{d,meas}^{(tot)} \\ \boldsymbol{C}_b^{(tot)} \end{bmatrix} x^{(tot)} = \begin{bmatrix} \boldsymbol{C}_{d,c}^{(tot)} \\ \boldsymbol{C}_b^{(tot)} \end{bmatrix} x^{(tot)} \end{cases} \tag{2.75}$$

The state-space model of the transmission simulator remains unmodified except for the negative input matrix. Then, the two systems are coupled as shown in Section 2.1.4.

Using the MCFS method in the state-space domain, the measured input and output vectors

$$\begin{Bmatrix} u_{meas}^{(ts)} & u_b^{(ts)} \end{Bmatrix}^T, \qquad \begin{Bmatrix} u_{meas}^{(tot)} & u_b^{(tot)} \end{Bmatrix}^T, \qquad \begin{Bmatrix} y_{meas}^{(ts)} & y_b^{(ts)} \end{Bmatrix}^T, \qquad \begin{Bmatrix} y_{meas}^{(tot)} & y_b^{(tot)} \end{Bmatrix}^T$$

are expressed in terms of modal coordinates marked by the subscript *mod*. This is again done by means of the modal matrix $(\boldsymbol{\Phi}_{meas}^{(ts)})^+$. The body inputs and outputs remain unchanged. Hence, the new inputs and outputs are given by

$$\begin{Bmatrix} u_{meas}^{(tot)} \\ u_b^{(tot)} \end{Bmatrix} = \begin{bmatrix} \left(\left(\boldsymbol{\Phi}_{meas}^{(ts)} \right)^+ \right)^T & \boldsymbol{0} \\ \boldsymbol{0} & \boldsymbol{I} \end{bmatrix} \begin{Bmatrix} u_{mod}^{(tot)} \\ u_b^{(tot)} \end{Bmatrix}, \qquad \begin{Bmatrix} u_{meas}^{(ts)} \\ u_b^{(ts)} \end{Bmatrix} = \begin{bmatrix} \left(\left(\boldsymbol{\Phi}_{meas}^{(ts)} \right)^+ \right)^T & \boldsymbol{0} \\ \boldsymbol{0} & \boldsymbol{I} \end{bmatrix} \begin{Bmatrix} u_{mod}^{(ts)} \\ u_b^{(ts)} \end{Bmatrix} \tag{2.76}$$

and

$$\begin{Bmatrix} y_{mod}^{(tot)} \\ y_b^{(tot)} \end{Bmatrix} = \begin{bmatrix} \left(\boldsymbol{\Phi}_{meas}^{(ts)} \right)^+ & \boldsymbol{0} \\ \boldsymbol{0} & \boldsymbol{I} \end{bmatrix} \begin{Bmatrix} y_{meas}^{(tot)} \\ y_b^{(tot)} \end{Bmatrix}, \qquad \begin{Bmatrix} y_{mod}^{(ts)} \\ y_b^{(ts)} \end{Bmatrix} = \begin{bmatrix} \left(\boldsymbol{\Phi}_{meas}^{(ts)} \right)^+ & \boldsymbol{0} \\ \boldsymbol{0} & \boldsymbol{I} \end{bmatrix} \begin{Bmatrix} y_{meas}^{(ts)} \\ y_b^{(ts)} \end{Bmatrix}, \tag{2.77}$$

respectively. With the new vectors, the transformed models

$$\begin{cases} \dot{x}^{(tot)} = \boldsymbol{A}^{(tot)} x^{(tot)} + \begin{bmatrix} \boldsymbol{B}_{meas}^{(tot)} & \boldsymbol{B}_b^{(tot)} \end{bmatrix} \begin{bmatrix} \left(\left(\boldsymbol{\Phi}_{meas}^{(ts)} \right)^+ \right)^T & \boldsymbol{0} \\ \boldsymbol{0} & \boldsymbol{I} \end{bmatrix} \begin{Bmatrix} u_{mod}^{(tot)} \\ u_b^{(tot)} \end{Bmatrix} \\ \qquad = \boldsymbol{A}^{(tot)} x^{(tot)} + \begin{bmatrix} \boldsymbol{B}_{mod}^{(tot)} & \boldsymbol{B}_b^{(tot)} \end{bmatrix} \begin{Bmatrix} u_{mod}^{(ts)} \\ u_b^{(tot)} \end{Bmatrix} \\ \begin{Bmatrix} y_{mod}^{(tot)} \\ y_b^{(tot)} \end{Bmatrix} = \begin{bmatrix} \left(\boldsymbol{\Phi}_{meas}^{(ts)} \right)^+ & \boldsymbol{0} \\ \boldsymbol{0} & \boldsymbol{I} \end{bmatrix} \begin{bmatrix} \boldsymbol{C}_{d,meas}^{(tot)} \\ \boldsymbol{C}_b^{(tot)} \end{bmatrix} x^{(tot)} = \begin{bmatrix} \boldsymbol{C}_{d,mod}^{(tot)} \\ \boldsymbol{C}_b^{(tot)} \end{bmatrix} x^{(tot)} \end{cases} \tag{2.78}$$

and

$$\begin{cases} \dot{x}^{(ts)} = \boldsymbol{A}^{(ts)} x^{(ts)} + \begin{bmatrix} \boldsymbol{B}_{meas}^{(ts)} & \boldsymbol{B}_b^{(ts)} \end{bmatrix} \begin{bmatrix} \left(\left(\boldsymbol{\Phi}_{meas}^{(ts)} \right)^+ \right)^T & \boldsymbol{0} \\ \boldsymbol{0} & \boldsymbol{I} \end{bmatrix} \begin{Bmatrix} u_{mod}^{(ts)} \\ u_b^{(ts)} \end{Bmatrix} \\ \qquad = \boldsymbol{A}^{(ts)} x^{(ts)} + \begin{bmatrix} \boldsymbol{B}_{mod}^{(ts)} & \boldsymbol{B}_b^{(ts)} \end{bmatrix} \begin{Bmatrix} u_{mod}^{(ts)} \\ u_b^{(ts)} \end{Bmatrix} \\ \begin{Bmatrix} y_{mod}^{(ts)} \\ y_b^{(ts)} \end{Bmatrix} = \begin{bmatrix} \left(\boldsymbol{\Phi}_{meas}^{(ts)} \right)^+ & \boldsymbol{0} \\ \boldsymbol{0} & \boldsymbol{I} \end{bmatrix} \begin{bmatrix} \boldsymbol{C}_{d,meas}^{(ts)} \\ \boldsymbol{C}_b^{(ts)} \end{bmatrix} x^{(ts)} = \begin{bmatrix} \boldsymbol{C}_{d,mod}^{(ts)} \\ \boldsymbol{C}_b^{(ts)} \end{bmatrix} x^{(ts)} \end{cases} \tag{2.79}$$

are obtained.

By coupling these models, the influence of the transmission simulator is removed and the system of interest is deduced. The final state-space system is then

$$\begin{cases} \begin{Bmatrix} \ddot{\bar{y}}_{mod} \\ \dot{\bar{y}}_{mod} \\ \dot{x}_b^{(tot)} \\ \dot{x}_b^{(ts)} \end{Bmatrix} = \begin{bmatrix} \bar{\boldsymbol{A}}_{vv} & \bar{\boldsymbol{A}}_{vd} & \bar{\boldsymbol{A}}_{vb}^{(tot)} & \bar{\boldsymbol{A}}_{vb}^{(ts)} \\ \boldsymbol{I} & \boldsymbol{0} & \boldsymbol{0} & \boldsymbol{0} \\ \boldsymbol{0} & \boldsymbol{A}_{bd}^{(tot)} & \boldsymbol{A}_{bb}^{(tot)} & \boldsymbol{0} \\ \boldsymbol{0} & \boldsymbol{A}_{bd}^{(ts)} & \boldsymbol{0} & \boldsymbol{A}_{bb}^{(ts)} \end{bmatrix} \begin{Bmatrix} \dot{\bar{y}}_{mod} \\ \bar{y}_{mod} \\ x_b^{(tot)} \\ x_b^{(ts)} \end{Bmatrix} + \begin{bmatrix} \bar{\boldsymbol{B}}_{vv} & \bar{\boldsymbol{B}}_{vb}^{(tot)} & \bar{\boldsymbol{B}}_{vb}^{(ts)} \\ \boldsymbol{0} & \boldsymbol{0} & \boldsymbol{0} \\ \boldsymbol{0} & \boldsymbol{B}_{bb}^{(tot)} & \boldsymbol{0} \\ \boldsymbol{0} & \boldsymbol{0} & \boldsymbol{B}_{bb}^{(ts)} \end{bmatrix} \begin{Bmatrix} \bar{u}_{mod} \\ u_b^{(tot)} \\ u_b^{(ts)} \end{Bmatrix} \\ \begin{Bmatrix} \bar{y}_{mod} \\ y_b^{(tot)} \\ y_b^{(ts)} \end{Bmatrix} = \begin{bmatrix} \boldsymbol{0} & \boldsymbol{I} & \boldsymbol{0} & \boldsymbol{0} \\ \boldsymbol{C}_{bv}^{(tot)} & \boldsymbol{C}_{bd}^{(tot)} & \boldsymbol{C}_{bb}^{(tot)} & \boldsymbol{0} \\ \boldsymbol{C}_{bv}^{(ts)} & \boldsymbol{C}_{bd}^{(ts)} & \boldsymbol{0} & \boldsymbol{C}_{bb}^{(ts)} \end{bmatrix} \begin{Bmatrix} \dot{\bar{y}}_{mod} \\ \bar{y}_{mod} \\ x_b^{(tot)} \\ x_b^{(ts)} \end{Bmatrix} \end{cases} \tag{2.80}$$

with

$$\begin{cases} \boldsymbol{K} = \left(\boldsymbol{B}_{vv}^{(tot)} - \boldsymbol{B}_{vv}^{(ts)}\right)^{-1} \\ \bar{\boldsymbol{A}}_{vv} = \boldsymbol{B}_{vv}^{(tot)}\boldsymbol{K}\boldsymbol{A}_{vv}^{(ts)} - \boldsymbol{B}_{vv}^{(ts)}\boldsymbol{K}\boldsymbol{A}_{vv}^{(tot)} \\ \bar{\boldsymbol{A}}_{vd} = \boldsymbol{B}_{vv}^{(tot)}\boldsymbol{K}\boldsymbol{A}_{vd}^{(ts)} - \boldsymbol{B}_{vv}^{(ts)}\boldsymbol{K}\boldsymbol{A}_{vd}^{(tot)} \\ \bar{\boldsymbol{A}}_{vb}^{(tot)} = -\boldsymbol{B}_{vv}^{(ts)}\boldsymbol{K}\boldsymbol{A}_{vb}^{(tot)} \\ \bar{\boldsymbol{A}}_{vb}^{(ts)} = \boldsymbol{B}_{vv}^{(tot)}\boldsymbol{K}\boldsymbol{A}_{vb}^{(ts)} \\ \bar{\boldsymbol{B}}_{vv} = -\boldsymbol{B}_{\boldsymbol{vv}}^{(tot)}\boldsymbol{K}\boldsymbol{B}_{vv}^{(ts)} \\ \bar{\boldsymbol{B}}_{vb}^{(tot)} = -\boldsymbol{B}_{vv}^{(ts)}\boldsymbol{K}\boldsymbol{B}_{vb}^{(tot)} \\ \bar{\boldsymbol{B}}_{vb}^{(ts)} = \boldsymbol{B}_{vv}^{(tot)}\boldsymbol{K}\boldsymbol{B}_{vb}^{(ts)} \end{cases}$$

Here, the input matrix $\boldsymbol{B}^{(ts)}$ is considered positive and the minus is written down explicitly for a better understanding. Note that this is the same result as applying traditional state-space synthesis with a negative input matrix

$$\boldsymbol{B}^{(ts)} = -\begin{bmatrix} \boldsymbol{B}_{mod}^{(ts)} & \boldsymbol{B}_b^{(ts)} \end{bmatrix}.$$

If n_{ts} copies of the transmission simulator are decoupled from n_{tot} copies of the total system, Equation (2.43) changes accordingly to

$$\begin{aligned} & n_{tot}\boldsymbol{B}_{vv}^{(tot)^{-1}}\ddot{y}_c^{(tot)} + n_{ts}\boldsymbol{B}_{vv}^{(ts)^{-1}}\ddot{y}_c^{(ts)} \\ & \quad = n_{tot}\boldsymbol{B}_{vv}^{(tot)^{-1}}\left(\boldsymbol{A}_{vv}^{(tot)}\dot{y}_c^{(tot)} + \boldsymbol{A}_{vd}^{(tot)}y_c^{(tot)} + \boldsymbol{A}_{vb}^{(tot)}y_b^{(tot)} + \boldsymbol{B}_{vv}^{(tot)}u_c^{(tot)} + \boldsymbol{B}_{vb}^{(tot)}u_b^{(tot)}\right) \\ & \quad + n_{ts}\boldsymbol{B}_{vv}^{(ts)^{-1}}\left(\boldsymbol{A}_{vv}^{(ts)}\dot{y}_c^{(ts)} + \boldsymbol{A}_{vd}^{(ts)}y_c^{(ts)} + \boldsymbol{A}_{vb}^{(ts)}y_b^{(ts)} + \boldsymbol{B}_{vv}^{(ts)}u_c^{(ts)} + \boldsymbol{B}_{vb}^{(ts)}u_b^{(ts)}\right). \end{aligned} \tag{2.81}$$

This is equal to dividing $\boldsymbol{B}_{vv}^{(tot)}$ by n_{tot} and $\boldsymbol{B}_{vv}^{(ts)}$ by n_{ts}. Note that care must be taken with the term $\bar{\boldsymbol{B}}_{vv}$. As in equation (2.57), only the mass, stiffness, and damping parameters are multiplied but the input matrix for the forces remains equal. Therefore, the equilibrium condition (2.44) also remains unmodified. Hence, the definition of $\bar{\boldsymbol{B}}_{vv}$ changes. If each system is only coupled once, recall the definition

$$\bar{\boldsymbol{B}}_{vv} = \boldsymbol{B}_{\boldsymbol{vv}}^{(tot)}\boldsymbol{K}\boldsymbol{B}_{vv}^{(ts)} = \boldsymbol{B}_{\boldsymbol{vv}}^{(tot)}\left(\boldsymbol{B}_{vv}^{(tot)} - \boldsymbol{B}_{vv}^{(ts)}\right)^{-1}\boldsymbol{B}_{vv}^{(ts)}. \tag{2.82}$$

However, if at least one of the systems is to be coupled multiple times, the definition changes to

$$\bar{\boldsymbol{B}}_{vv} = \frac{n_{tot}+n_{ts}}{n_{tot}n_{ts}}\boldsymbol{B}_{\boldsymbol{vv}}^{(tot)}\boldsymbol{K}\boldsymbol{B}_{vv}^{(ts)} = \frac{n_{tot}+n_{ts}}{n_{tot}n_{ts}}\boldsymbol{B}_{\boldsymbol{vv}}^{(tot)}\left(\frac{1}{n_{tot}}\boldsymbol{B}_{vv}^{(tot)} - \frac{1}{n_{ts}}\boldsymbol{B}_{vv}^{(ts)}\right)^{-1}\boldsymbol{B}_{vv}^{(ts)}. \tag{2.83}$$

2.3 Receptance, Mobility and Accelerance FRFs

In this work, the input to a system will always be force excitation. Depending on the output, different terms to denote the FRF will be used [29]. If the output of the system is a set of displacements, the term receptance and the subscript d will be used. Mobility data stands for velocity outputs, indicated by the subscript v, whereas acceleration outputs yield accelerance FRFs and will be indicated by a. In addition, the term driving-point or direct FRF labels a frequency response function where the input and output are located at the same position.

In the frequency domain, velocity and acceleration can be deduced from the displacement by multiplying with $i\omega$ and $-\omega^2$, respectively. Accordingly, the receptance FRF $\boldsymbol{H}_d$ is connected to the mobility FRF $\boldsymbol{H}_v$ and the accelerance FRF $\boldsymbol{H}_a$ by

$$\boldsymbol{H}_a = i\omega \boldsymbol{H}_v = i\omega \left(i\omega \boldsymbol{H}_d \right) = -\omega^2 \boldsymbol{H}_d. \tag{2.84}$$

In order to synthesize FRFs from state-space systems, the output equation of the time-domain state-space model has to be adapted. Output displacements are given by

$$y = \boldsymbol{C}_d x. \tag{2.85}$$

Velocity outputs can be obtained from the derivative

$$\dot{y} = \boldsymbol{C}_d \dot{x} = \boldsymbol{C}_d \left(\boldsymbol{A}x + \boldsymbol{B}u \right) = \boldsymbol{C}_d \boldsymbol{A} x + \boldsymbol{C}_d \boldsymbol{B} u = \boldsymbol{C}_v x + \boldsymbol{D}_v u. \tag{2.86}$$

Since Newton's second law states that forces and velocities are connected via integration, there must not be a direct feedthrough from force input to velocity outputs for physical, structural problems modelled with state-space, thus

$$\boldsymbol{D}_v = \boldsymbol{C}_d \boldsymbol{B} = 0. \tag{2.87}$$

If the state vector is formed by displacements and velocities, $x = \begin{bmatrix} q^T & \dot{q}T \end{bmatrix}^T$, the relation can also be illustrated by

$$y = \boldsymbol{C}_d x = \begin{bmatrix} \boldsymbol{P}_y & \boldsymbol{0} \end{bmatrix} x \tag{2.88}$$

$$\begin{aligned} \dot{y} &= \boldsymbol{C}_d \boldsymbol{A} x + \boldsymbol{C}_d \boldsymbol{B} u = \begin{bmatrix} \boldsymbol{P}_y & \boldsymbol{0} \end{bmatrix} \begin{bmatrix} \boldsymbol{0} & \boldsymbol{I} \\ -\boldsymbol{M}^{-1}\boldsymbol{K} & -\boldsymbol{M}^{-1}\boldsymbol{V} \end{bmatrix} x + \begin{bmatrix} \boldsymbol{P}_y & \boldsymbol{0} \end{bmatrix} \begin{bmatrix} \boldsymbol{0} \\ \boldsymbol{M}^{-1}\boldsymbol{P}_u \end{bmatrix} u \\ &= \begin{bmatrix} \boldsymbol{0} & \boldsymbol{P}_y \end{bmatrix} x + \boldsymbol{0} u = \boldsymbol{C}_v x \end{aligned} \tag{2.89}$$

Acceleration outputs can be obtained accordingly with

$$\ddot{y} = \boldsymbol{C}_v \dot{x} = \boldsymbol{C}_v \left(\boldsymbol{A}x + \boldsymbol{B}u \right) = \boldsymbol{C}_v \boldsymbol{A} x + \boldsymbol{C}_v \boldsymbol{B} u = \boldsymbol{C}_d \boldsymbol{A}^2 x + \boldsymbol{C}_d \boldsymbol{A} \boldsymbol{B} u = \boldsymbol{C}_a x + \boldsymbol{D}_a u \tag{2.90}$$

or in terms of a physical state vector,

$$\begin{aligned} \ddot{y} &= \boldsymbol{C}_v \boldsymbol{A} x + \boldsymbol{C}_v \boldsymbol{B} u = \begin{bmatrix} \boldsymbol{0} & \boldsymbol{P}_y \end{bmatrix} \begin{bmatrix} \boldsymbol{0} & \boldsymbol{I} \\ -\boldsymbol{M}^{-1}\boldsymbol{K} & -\boldsymbol{M}^{-1}\boldsymbol{V} \end{bmatrix} x + \begin{bmatrix} \boldsymbol{0} & \boldsymbol{P}_y \end{bmatrix} \begin{bmatrix} \boldsymbol{0} \\ \boldsymbol{M}^{-1}\boldsymbol{P}_u \end{bmatrix} u \\ &= \begin{bmatrix} -\boldsymbol{P}_y \boldsymbol{M}^{-1} K & -\boldsymbol{P}_y \boldsymbol{M}^{-1} V \end{bmatrix} x + \boldsymbol{P}_y \boldsymbol{M}^{-1} \boldsymbol{P}_u u = \boldsymbol{C}_a x + \boldsymbol{D}_a u. \end{aligned} \tag{2.91}$$

2.4 The Domain Transformations

To compare the results of the different substructuring methods, it is desired to transform models from one domain to another. FRFs of modal and state-space models are synthesized with

$$\boldsymbol{H}(\omega) = \Phi \big(-\omega^2 \boldsymbol{M}_{mod} + i\omega \boldsymbol{V}_{mod} + \boldsymbol{K}_{mod} \big)^{-1} \Phi^T \tag{2.92}$$

and

$$\boldsymbol{H}(\omega) = \boldsymbol{C}(i\omega \boldsymbol{I} - \boldsymbol{A})^{-1} \boldsymbol{B} + \boldsymbol{D}, \tag{2.93}$$

respectively. A second-order modal model is connected to a first-order state-space system with the matrices

$$\begin{cases} \boldsymbol{A} = \begin{bmatrix} \boldsymbol{0} & \boldsymbol{I} \\ -\boldsymbol{M}_{mod}^{-1} \boldsymbol{K}_{mod} & -\boldsymbol{M}_{mod}^{-1} \boldsymbol{V}_{mod} \end{bmatrix} \\ \boldsymbol{B} = \begin{bmatrix} \boldsymbol{0} \\ \boldsymbol{M}_{mod}^{-1} \boldsymbol{\Phi}^T \boldsymbol{P}_u \end{bmatrix} \\ \boldsymbol{C} = \begin{bmatrix} \boldsymbol{P}_y \boldsymbol{\Phi} & \boldsymbol{0} \end{bmatrix}. \end{cases} \tag{2.94}$$

Obtaining a second-order modal model from a state-space model is somewhat less straightforward. The eigenvalues of the system matrix $\boldsymbol{A}$ come in complex conjugated pairs $\lambda_{i,i+1} = -\omega_i \xi_i \pm i\omega_i \sqrt{1-\xi_i{}^2}$. For lightly damped structures, $\xi_i{}^2$ is negligible yielding $\lambda_{i,i+1} \approx -\omega_i \xi_i \pm i\omega_i$. Thus, the resonance frequency and modal damping can be deduced easily.

To scale the calculated eigenvectors, the modal mass m_{mod} can be utilized. Using the input and output matrices $\boldsymbol{B}$ and $\boldsymbol{C}$, the modal Foss damping a_i is calculated [30] which is related to the model parameters by

$$a_i = 2\xi_i \omega_i m_{mod} + 2\lambda_i m_{mod,i}, \tag{2.95}$$

assuming that the damping matrix can be brought to diagonal form. With the aforementioned approximation for lightly damped structures, the modal mass is extracted by

$$m_{mod,i} = \frac{\Im(a_i)}{2\omega_i}. \tag{2.96}$$

Solving the eigenvalue problem of the state-space system, the obtained eigenvectors will be complex. However, for lightly damped systems or system with proportional damping, the entries of every eigenvector form a straight line arbitrarily rotated in the complex plane. After rotating the eigenvector such that it coincides with the real axis, a real mode shape vector is obtained which can then be mass normalised.

2.5 System Identification of Physical Models

Before coupling state-space systems, models have to be identified starting from the measured FRFs. In the present work, state-space subspace identification is applied using the command `n4sid` of MATLAB's System Identification toolbox [12]. The theory of subspace identification can be found in the books of Ljung [11], and Van Overschee and De Moor [31].

The correct model order of the identified system is decisive for the success of substructuring. It can be found by thorough investigation of the measurement data to distinguish physical from spurious modes. Yet, this approach is cumbersome and its success is not guaranteed. An alternative is the automated system identification method developed by Yaghoubi and Abrahamsson [32]. Both approaches are used in this thesis.

Another crucial point in the synthesis of state-space models is physically consistent models. This was stressed in the work of Sjövall and Abrahamsson [9] and Liljerehn and Abrahamsson [33]. In contrast to second-order modal models identified with common mode extraction techniques, state-space models, estimated with first-order system identification, are rather general representations of systems, which try to replicate the data as well as possible, independent of potential violation of physical laws. However, measurement errors may yield unphysical models. Thus, a physically correct model needs to be ensured by enforcing physical properties. In the remainder of this section, all necessary steps are explained [33].

Starting from an identified model with velocity outputs denoted mobility form, first reciprocity is enforced. Maxwell's reciprocity theorem states that the response of a system measured at position i and excited at position j is the same as the response measured at j and excited at i [34]. Thus, the FRF matrix of a reciprocal system is symmetric. Having measured all responses of a system excited at one position, reciprocity can be used to obtain the unmeasured FRFs.

Next, passivity of the system is enforced. The energy dissipated in a passive system must be non-negative. This implies a non-negative real part of the mobility driving-point FRF for reciprocal systems [9], yielding a phase of $[-90°, 0°]$. Equivalently, the accelerance and receptance driving-point FRFs have a phase range of $[0°, 180°]$ and $[-180°, 0°]$, respectively. Another interpretation is that the receptance condition ensures the response at the driving-point to be in the direction of the excitation force. A method developed by Liljerehn [33] is utilized for the enforcement.

Finally, a force input to a system fulfilling Newton's second law has a direct effect on the acceleration only, not on velocity or displacement. For state-space systems, this corresponds to a zero direct feedthrough matrix $\boldsymbol{D}$. Measurement errors or model truncation may evoke a non-zero feedthrough matrix. Thus, the satisfaction of $\boldsymbol{D_d} = \boldsymbol{0}$ and $\boldsymbol{D_v} = \boldsymbol{C_d B} = \boldsymbol{0}$ has to be checked.

2.6 The Modal Assurance Criterion

To compare the mode shapes of two models, the Modal Assurance Criterion (MAC) is applied. The MAC value is a metric for the linear consistency of two mode shape sets [35] and lies between 1 for perfect consistency and

0 for no consistency at all. For the two vectors ϕ_k and ϕ_l, it is calculated for the mode i as

$$MAC_{kl,i} = \frac{|\phi_{k,i}^T \phi_{l,i}^*|^2}{\phi_{k,i}^T \phi_{k,i}^* \phi_{l,i}^T \phi_{l,i}^*} \tag{2.97}$$

where * indicates the complex conjugate of the vector. In general, a MAC value below 0.8 is considered as bad whereas a MAC value above 0.9 is a good correlation [29].

The MAC metric may lack significance for symmetric structures as the rotor of a wind turbine. Due to the symmetry, some modes are symmetric modes that are typically close in frequency. For such modes, the calculated eigenvectors of the identified system span the subspace associated with these modes, yet they can be arbitrarily rotated. In contrast, the modes of FE models often represent shapes that meet intuition. Thus, the identified mode shapes are most likely a linear combination of the associated FE mode shape vectors yielding low MAC values. To account for that, the angle between the subspaces spanned by the identified eigenvectors and the FE mode shapes is calculated for modes close in frequency [36]. If the angle is close to zero, the subspaces align well, and the corresponding mode shapes replicate the same motion. The squared cosine of the angle between subspaces spanned by only one vector each is equal to the MAC value. Therefore, both the MAC value and the squared cosine of the subspace angle will be used to assess the coherency of two models for symmetric structures.

3 The Beam Example

In this chapter, the transmission simulator is applied to a simple structure consisting of only a few beam elements. By this example, numerous effects and problems, which are typically encountered, can be illustrated. This includes for instance the design of the transmission simulator and the choice of modes to span the mode shape basis. In the first section, the example is depicted, and decoupling is performed. Here, a system will be subtracted without the use of a transmission simulator, assuming that the connection point's motion is given. This is followed by the transmission simulator method with CPT and MCFS in the second section.

3.1 Decoupling

In order to compare the substructuring methods CMS, FBS, and state-space synthesis, a simple example is chosen. With its aid, it will be shown that all decoupling methods yield the same results if the same information is inherent in the models and if the transmission simulator is applied properly. A beam structure is chosen for this purpose, built up by plane elements obtained from axial and Bernoulli-Euler bending elements [4, 37]. The mass and the stiffness matrices of one element are

$$\boldsymbol{M}_e = \frac{m}{420}\begin{bmatrix} 140 & 0 & 0 & 70 & 0 & 0 \\ 0 & 156 & 22l & 0 & 54 & -13l \\ 0 & 22l & 4l^2 & 0 & 13l & -3l^2 \\ 70 & 0 & 0 & 140 & 0 & 0 \\ 0 & 54 & 13l & 0 & 156 & -22l \\ 0 & -13l & -3l^2 & 0 & -22l & 4l^2 \end{bmatrix} \tag{3.1}$$

and

$$\boldsymbol{K}_e = \begin{bmatrix} \frac{EA}{l} & 0 & 0 & -\frac{EA}{l} & 0 & 0 \\ 0 & 12\frac{EI}{l^3} & 6\frac{EI}{l^2} & 0 & -12\frac{EI}{l^3} & 6\frac{EI}{l^2} \\ 0 & 6\frac{EI}{l^2} & 4\frac{EI}{l} & 0 & -6\frac{EI}{l^2} & 2\frac{EI}{l} \\ -\frac{EA}{l} & 0 & 0 & \frac{EA}{l} & 0 & 0 \\ 0 & -12\frac{EI}{l^3} & -6\frac{EI}{l^2} & 0 & 12\frac{EI}{l^3} & -6\frac{EI}{l^2} \\ 0 & 6\frac{EI}{l^2} & 2\frac{EI}{l} & 0 & -6\frac{EI}{l^2} & 4\frac{EI}{l} \end{bmatrix}, \tag{3.2}$$

respectively, with the element mass m, the length l, Young's modulus E, the cross section A and the second moment of area $I = bh^3/12$. To obtain the beam structures, these element matrices are coupled in the physical domain as is done in FE calculations.

The assembled beam structure involves two beams. The left one, dubbed A, will later be the structure of interest in the decoupling procedure and consists of three elements. A two-element beam denoted B is supposed to be coupled to the former in order to form the total structure, called AB. The elements of this structure have the material properties of steel, i.e. a density of $\rho = 8000\,\mathrm{kg/m^3}$ and Young's modulus of $E = 210\,\mathrm{GPa}$. The cross section is chosen to be quadratic with a side length $b = h = 0.01\,\mathrm{m}$. With the element length $l = 0.1\,\mathrm{m}$, the mass and stiffnesses of one element are $m = 0.08\,\mathrm{kg}$, $EI = 175\,\mathrm{Nm^2}$ and $EA = 21{,}000{,}000\,\mathrm{N}$. To create a lightly damped structure, proportional damping was set to $\boldsymbol{V} = \alpha\boldsymbol{M} + \beta\boldsymbol{K}$, $\alpha = 0.1$, and $\beta = 10^{-8}$.

First, the influence of beam B will be removed from the assembled system AB to arrive at a model for A. Decoupling in this example acts on the assumption that all DOFs of the connection point 4 between A and B are known. Obviously, this will rarely be the case in reality since the coupling point is typically not accessible in a coupled configuration. However, with the help of this rather escapist assumption, the subtraction of systems in the frequency and state-space domain will be investigated. The procedure is depicted in Figure 3.1, where black nodes indicate that all three DOFs are known, whereas the DOFS of white nodes are unknown simulating a restricted number of measurement points.

All methods mentioned in the theory chapter are applied to this example, that is decoupling with CMS, inverse coupling and direct decoupling of FRFs as well as state-space decoupling. The latter is performed both

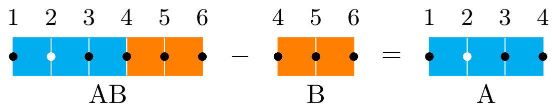

Figure 3.1: *Decoupling scheme of two plane beams. The influence of beam B is to be removed from the structure AB in order to retrieve a model of A. All three DOFs at the black nodes are assumed to be known, whereas white nodes are unknown.*

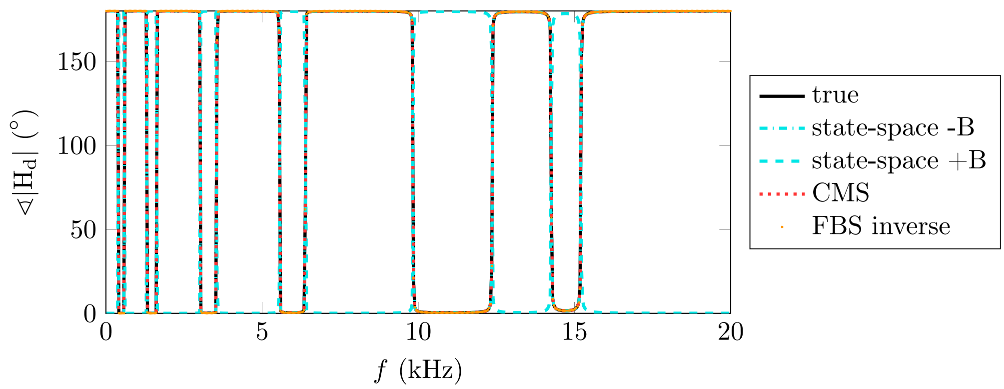

Figure 3.2: *Phase of the decoupled beam FRF. The direct receptance FRF at connection node 4 in lateral direction is shown. If a negative representation of B is coupled to AB, the phase of state-space synthesis with negative input matrix, CMS, and FBS equals the phase of the true system. The phase of state-space decoupling by subtracting the positive system B yields an inverted phase at the connection point.*

by coupling the system B with a negative input matrix and by subtracting the positive system B. As stated in the theory section, the phase at node 4 of beam A is inverted if the positive system B is subtracted. Figure 3.2 illustrates this observation. All other methods, including inverse coupling and direct decoupling of FRFs, yield exactly the same results. Neither Figure 3.2 nor Figure 3.3 show deviations between the FRF of true beam A and the decoupled structure. Note that in this example, there are more body degrees of freedom than coupling degrees of freedom which facilitates direct decoupling of FRFs.

In accordance with the FRFs, the calculated resonance frequencies and damping ratios of the CMS and state-space results match the true values exactly. However, this holds only for the flexible modes since some rigid body resonance frequencies in the initial beam models were found to be negative due to numerical inaccuracies and ill conditioned matrices.

An interesting feature in decoupling modal and state-space systems becomes apparent in this decoupling task. The state-space system obtained after substructuring has more states than the true system for beam A. Given the number of states n_{AB} and n_B for the beams AB and B, respectively, the number of states that

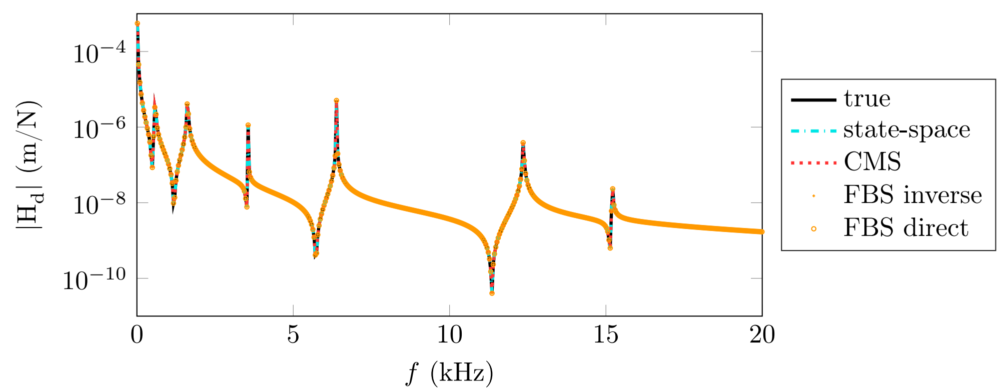

Figure 3.3: *Magnitude of the decoupled beam FRF. The direct receptance FRF at node 3 in lateral direction is shown. All methods yield the exact same FRF as the true system.*

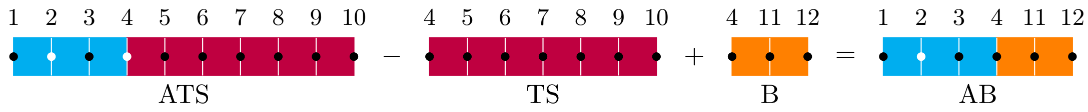

Figure 3.4: *Coupling scheme of two beams with the transmission simulator TS. Its influence is to be removed from the structure ATS in order to retrieve a model of A. Then, the system B is coupled in a second step. All three DOFs at the black nodes are assumed to be known, whereas white nodes are unknown.*

are retained after the coupling step are $n = n_{AB} + n_B - 2n_c$. Here, n_c is the number of coupling DOFs. This yields 48 states for the decoupled system in contrast to 24 states for the true system A. Accordingly, the decoupled model obtained with CMS has 24 modes instead of 12 modes. Moreover, the results reveal that the spurious modes come in pairs. Hence, the twelve spurious modes correspond to six spurious resonance frequencies. The occurrence of those pairs can be explained vividly by means of state-space coupling. The model of the decoupled beam A still consists of both the systems AB and B. Thus, the motion of B is present in the partitions associated with beam AB as well as in the partition corresponding to B, which yields an increased model order and the aforementioned spurious doubled states. In this example, those states can be easily identified and removed as the true resonance frequencies are unique, meaning that no repeated modes exist. However, the spurious states are no longer evident if the decoupling is performed with CPT and MCFS as will be stated later.

Furthermore, all investigated methods are interchangeable for damped structures, as long as the same information is used and noise is absent. If damping is removed, spurious peaks occur in the FRFs for state-space synthesis, since one of the spurious modes in each pair becomes unstable.

3.2 Utilisation of a Transmission Simulator

Now, a third beam, coupled to the beam A, is introduced as transmission simulator to form the assumed experimental structure ATS (see Figure 3.4). By means of this simple example, essential insights can be gained with respect to the transmission simulator's application. Especially, the design of the transmission simulator proves to be of utmost importance for the substructuring results. In this section, these observations are demonstrated.

The geometrical dimensions of the transmission simulator elements are chosen to be the same as for the other beams. In order to have enough measurement points on the transmission simulator, the beam is built up by six elements. All DOFs are assumed to be known, hence six measurement points on the transmission simulator with three DOFS each are available.

Under certain conditions, the mass matrix of the decoupled system can become indefinite [24]. To prevent this, the element mass of the transmission simulator was lowered and chosen to be $m_{ts} = 0.08m$. At the same time, the transmission simulator needs to be stiff. More precisely, the first flexible mode of the transmission simulator should to be higher than the first flexible mode of the structure of interest[1]. Therefore, Young's modulus $E_{ts} = 16E$ was chosen. With these properties, the transmission simulator features the desired behaviour while still being a beam with only a few elements.

3.2.1 Coupling with CPT

Twenty modes were chosen to represent the total system ATS, whereas nine modes were included in the transmission simulator representation, which corresponds to a condition number of 101.0 for the mode shape matrix $\mathbf{\Phi}^{(ts)}_{meas}$. If only the decoupling step ATS − TS = A is performed, beam A is retrieved unsatisfactorily.

The FRFs of the true and the substructured system resemble the axial motion very well but fail to replicate lateral and bending motion, as can be seen in Figure 3.5. Consequently, the estimated resonance frequencies of the beam A are not in agreement with the true ones.

Moreover, three of the obtained resonance frequencies in the CMS results are complex since both the mass matrix and the stiffness matrix become indefinite after substructuring. To force the model to be physical, two possible remedies exist. Mayes et al. proposed two techniques [25], which prevent negative mass matrices. Yet, a straightforward approach to remove complex resonance frequencies is their manual elimination since they are

[1]Again, this requirement was mentioned by Randy Mayes in a conversation.

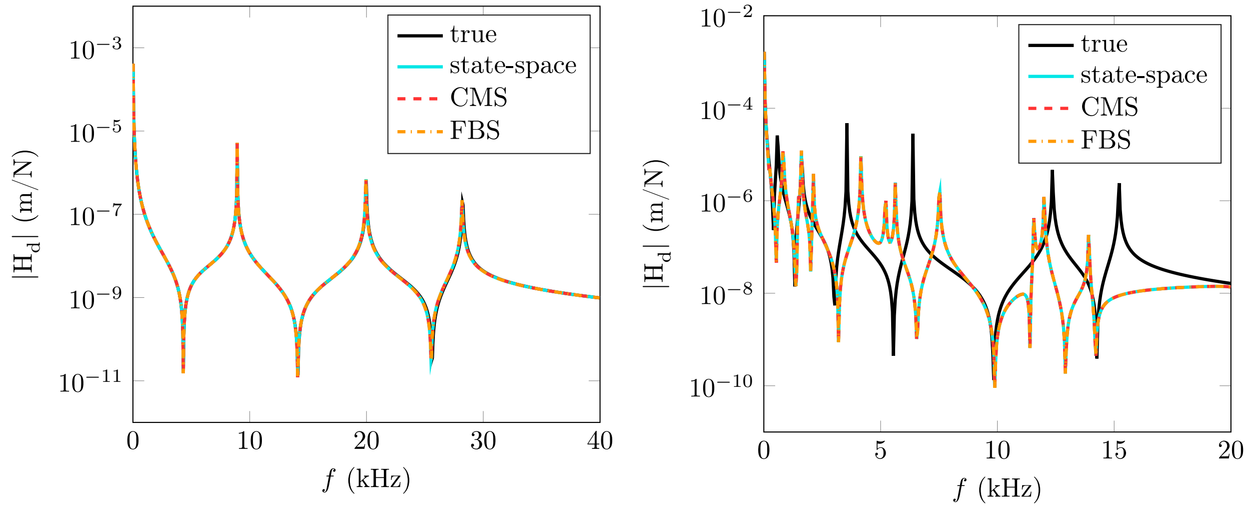

(a) *Direct receptance FRF, node 1 in axial direction*

(b) *Direct receptance FRF, node 4 in lateral direction*

Figure 3.5: *Results for the decoupled beam A with CPT in two directions. All methods yield the exact same FRF. The axial motion estimates the true FRF very well.*

easily identified. In general, this should not affect the estimated FRF. However, neither of the techniques is applied in the present work since the focus in this chapter is on the effects of the transmission simulator rather than on a physical result.

The identified complex resonance frequencies are also present in the state-space results. Here, they appear as their complex conjugates. This means that a purely imaginary resonance frequency in the CMS results transforms to a real pole in the state-space system which appears twice and is comparatively highly damped. One of these real poles is stable, the other unstable. However, the influence in the FRFs is not obvious due to the high damping.

A pair of complex conjugated resonance frequencies in the CMS results turn into two pairs of complex conjugated poles in the state-space representation. Again, the imaginary and real parts are exchanged. Further, two of the four eigenvalues are unstable. Compared to the other modal damping ratios in a lightly damped structure, the damping is still high, consequently reducing their effect on the FRF.

Complex resonance frequencies and state-space poles are complex conjugated because of the definition of the eigenvalue problem. For a second-order equation, the ansatz $e^{i\omega}$ is chosen, whereas a first-order state-space eigenvalue problem is solved with the ansatz e^{λ}. Hence, the resonance frequency will be obtained as a real value in the first formulation, while it is associated with the imaginary part of λ for state-space systems.

After analysing the decoupling step only, the whole coupling procedure as depicted in Figure 3.4 is now investigated. Both the predicted resonance frequencies and the obtained FRF of the beam AB are similar to the true system. Two FRFs are shown in Figure 3.6. Again, the axial motion is retrieved well whereas the lateral motion deviates significantly for lower frequencies and approaches the true FRF for higher frequencies. However, the overall behaviour is captured better than the behaviour of the beam A shown in Figure 3.5.

The first resonance frequency is underestimated by only 1 % but then, numerous spurious modes occur which leads to the spurious peaks in the lateral FRF in Figure 3.6. In contrast to the decoupling without transmission simulator, these modes cannot be readily identified as spurious any longer since they do not come in pairs. In total, six complex resonance frequencies are present in the results. Again, the investigated methods CMS, state-space coupling with a negative input matrix, and inverse coupling of FRFs, yield the same results. If damping is removed, unstable poles in the state-space synthesis occur. However, the FRFs do not deviate from the results obtained with damped systems.

3.2.2 Coupling with MCFS

Compared to CPT, the results both for the beam A and AB are significantly improved with MCFS. Here, all FRFs associated with the body DOFs of the beam A match the true FRF very well. Minor deviations occur only for the modes highest in frequency and are more pronounced at the connection node 4 in lateral and

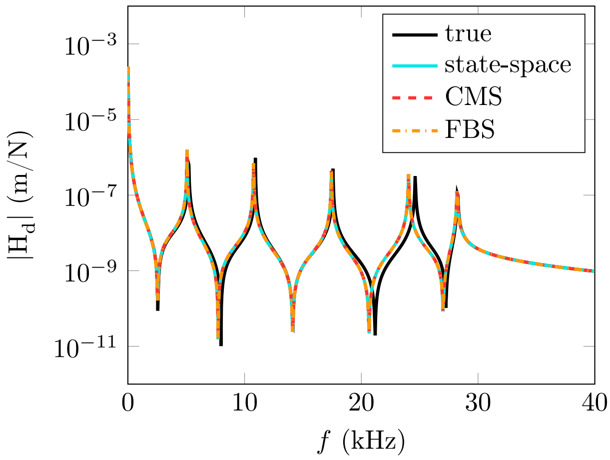

(a) *Direct receptance FRF, node 1 in axial direction*

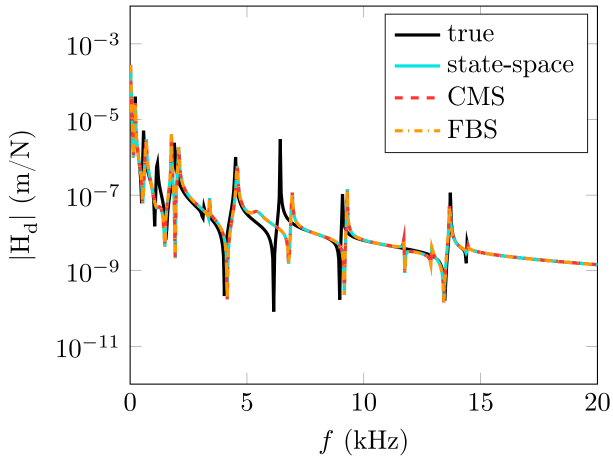

(b) *Direct receptance FRF, node 3 in lateral direction*

Figure 3.6: *Results for the coupled beam AB with CPT. All methods yield the exact same FRF. The axial motion can be estimated well, though one peak is shifted in frequency. Numerous spurious peaks occur in the FRF in lateral direction but the substructured FRF approaches the true FRF for higher frequencies. However, two modes are not captured at all.*

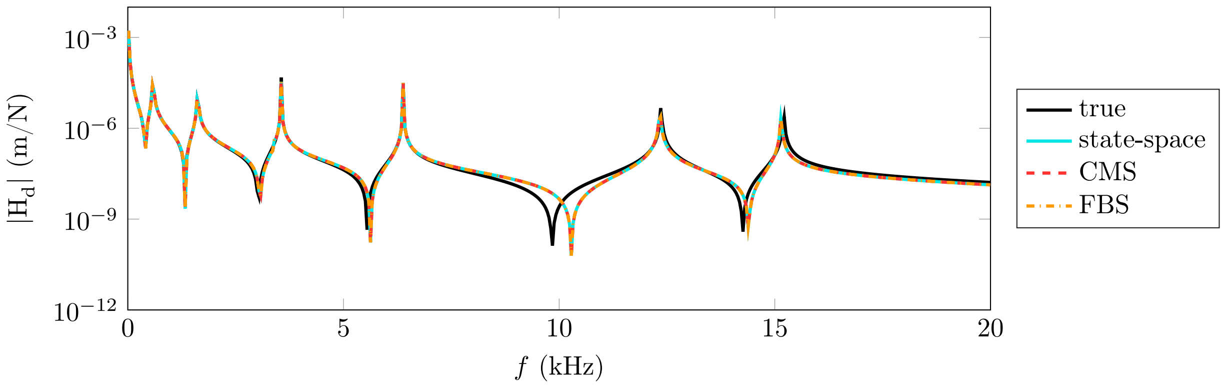

Figure 3.7: *Results for the decoupled beam A with MCFS. The direct receptance FRF at the connection node 4 in lateral direction is shown. All methods yield the exact same FRF, which resembles the true system well.*

rotational direction. By way of example, Figure 3.7 shows the lateral FRF at this node.

Figure 3.8 shows two FRFs of the coupled structure AB. The results are equally good for all DOFs, and only a few modes deviate visibly. Accordingly, the errors for the predicted resonance frequencies and for the damping of the first four modes are low. For higher frequencies, spurious modes appear that are difficult to distinguish from the true modes at first glance. In total, five of those spurious resonance frequencies are complex. As with CPT, unstable poles occur in the state-space results if damping is neglected, although there is no apparent change in the FRFs. In conclusion, the results obtained with MCFS are better than the CPT results, yet the same observations can be made with respect to spurious modes.

In the subsequent, the influence of the included modes for MCFS is investigated. As before, the total system ATS is represented using 20 modes. The results shown so far are obtained with a modal basis of the transmission simulator spanned by nine modes. Further, substructuring was performed with three, four, and six modes. As can be seen in Figure 3.9, the number of modes included has no influence on the axial motion. However, the substructuring results in the lateral direction deteriorate if less modes are considered. For a four mode basis, spurious peaks are present already in the low frequency area which is even more pronounced for three modes. In contrast, good results are gained for both six and nine modes.

Apparently, the motion of the total structure can be better replicated if more mode shapes of the transmission simulator are included. Then, the basis formed by the transmission simulator's modes is more likely to be appropriate for the coupled system's motion. At the same time, the condition number of the modal matrix

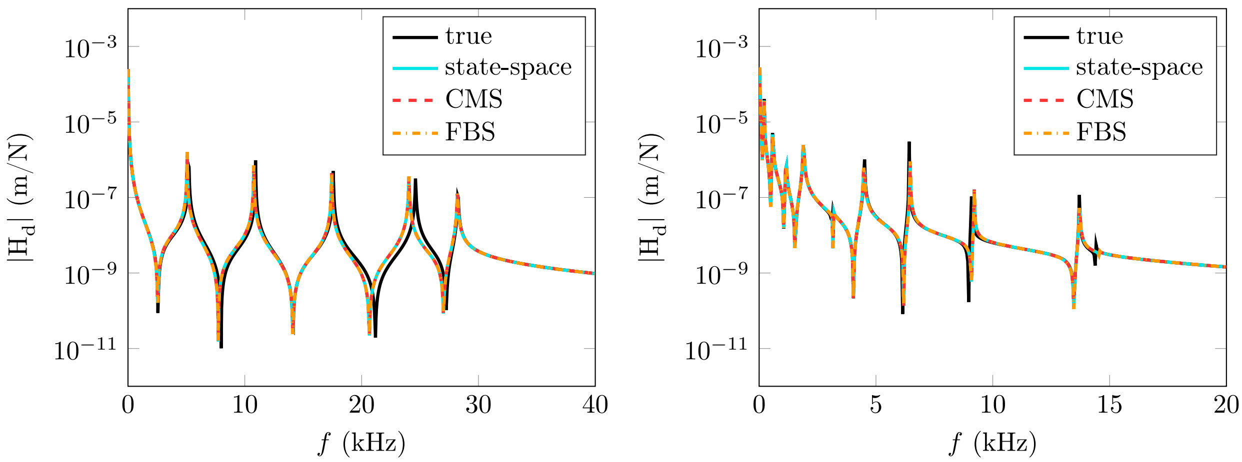

(a) *Direct receptance FRF, node 1 in axial direction* (b) *Direct receptance FRF, node 3 in lateral direction*

Figure 3.8: *Results for the coupled beam AB with MCFS. All methods yield the exact same FRF and both axial and lateral motion are estimated well.*

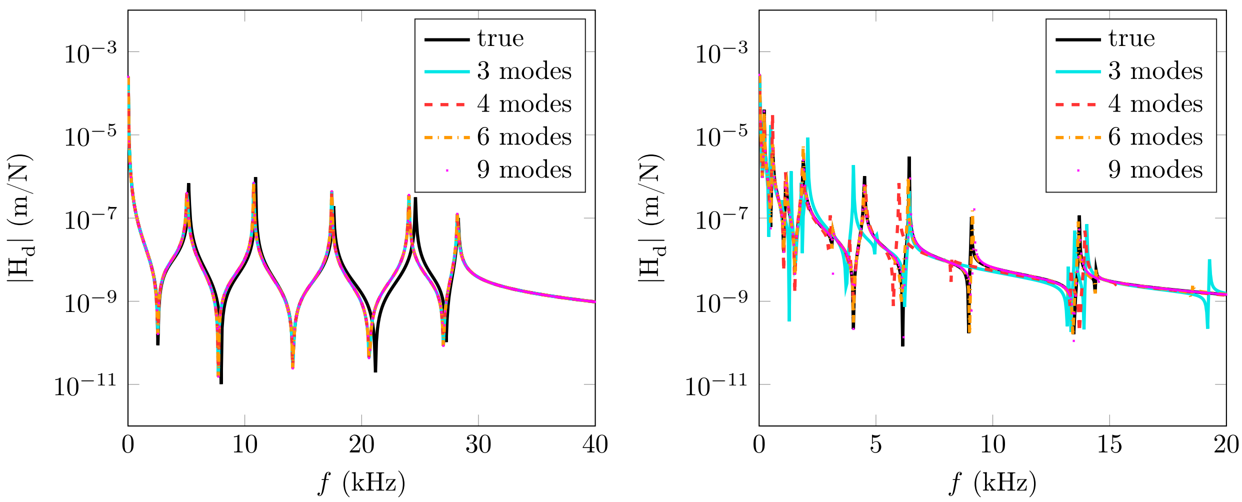

(a) *Direct receptance FRF, node 1 in axial direction* (b) *Direct receptance FRF, node 3 in lateral direction*

Figure 3.9: *Results for the coupled beam AB with MCFS. Here, the number of modes included in the transmission simulator is varied. The number of modes has no influence on the axial motion but the lateral FRFs deteriorate if less modes are considered. Only CMS results are plotted.*

$\mathbf{\Phi}^{(ts)}_{meas}$ increases. In this example, the lowest condition number is 5.9 for three modes. Four and six modes yield a condition number of 11.9 and 25.4, respectively, and the highest is obtained with nine modes and a value of 101.0. The condition number does not seem to be of great importance in a theoretical example like the present. However, for real structures, both experimental and FE models, the metric is believed to be crucial for the success of the transmission simulator [14]. In the literature, the reported condition numbers used in experimental structures were not higher than six [21, 28]. The condition number can be lowered if more measurement points are included. For experiments, this is in turn limited by factors such as the number of available sensors or the introduced mass-loading effect for lightweight structures. Thus, there is a trade-off between a higher number of modes and a limited number of sensors.

3.2.3 Remarks

Two remarks should be stated regarding the presented example. First, it was also attempted to use a vertical beam as transmission simulator following the experimental setup of Allen et al. [21]. In the variant used in this thesis, the beams were simplified and modelled with only few beam elements. The node in the middle of the transmission simulator was chosen as connection point. However, it showed that the mode shapes associated with the corresponding measurement points on the transmission simulator are not able to span an appropriate basis. Thus, the motion of the connection point could not be retrieved, which led to wrong coupling results. A possible remedy would be a second transmission simulator connected from the left to beam B. As stated in the theory chapter, coupling results can be improved if both structures are connected to a transmission simulator which is then removed twice. In the notation used here, this corresponds to $\mathrm{ATS} + \mathrm{TSB} - 2\mathrm{TS} = \mathrm{AB}$. However, the effect of a second transmission simulator on a theoretical example was not investigated in this work.

Second, the dynamics of the transmission simulator are crucial for the substructuring performance. In fact, it is advisable to have a stiff transmission simulator whose first flexible mode is higher in frequency than the first flexible mode of the structure of interest, as stated earlier. If this requirement is violated, the obtained coupling results are erroneous. One possible explanation may be that the dynamics of a too flexible transmission simulator affect the interface dynamics. However, it is difficult to link the erroneous results with the dynamics of the flexible transmission simulator. This insight was gained in the development of this example and will be explained by means of FBS in the following.

Given that the transmission simulator is too flexible, $\boldsymbol{H}^{tot}_{mod,mod}$ and $-\boldsymbol{H}^{ts}_{mod,mod}$ are full rank quadratic matrices. Yet, the summation becomes rank deficient if the transmission simulator is inappropriate. Using Jetmundsen's formulation, this matrix has to be inverted during the coupling procedure. Depending on the structures, good results may still be obtained if the pseudo-inverse is implemented instead, but one should be aware of the rank deficiency. Applying state-space coupling, the inappropriate transmission simulator causes the matrix partition $\boldsymbol{B}_{vv}$ to be rank deficient. In contrast, no evident indication of this issue was found in CMS. Thus, using different methods for the substructuring task proved to be helpful in order to find possible pitfalls.

To summarise the observations, the performance of the substructure process is mainly governed by the chosen properties of the transmission simulator. Changes in the stiffness and mass can result in improvements but also in deteriorated results. Of great importance is the number of modes in the transmission simulator representation as well as the chosen measurement points. The latter needs to contain enough information to fairly represent the motion of the total structure. Therefore, numerical pre-studies of at least the transmission simulator are crucial in order to find suitable structures, measurement points and mode shapes. If the complete substructuring task can be simulated beforehand using numerical models, the experiments can be designed and prepared even better. However, numerical models of the structure of interest may not be at hand, since the lack of models is one of the reasons for applying experimental substructuring.

Moreover, the condition number is believed to play a significant role in substructuring of real structures but did not show an effect on the beam elements. Furthermore, the stiffness and mass matrices of the substructured system become indefinite under certain conditions, yielding complex resonance frequencies in CMS. The complex conjugates of these frequencies occur as doubled poles in the state-space system. Finally, all methods yield the same results if the transmission simulator is well defined. Otherwise, investigating the results of different methods helps in finding possible sources of errors.

4 Application to the Ampair 600 Wind Turbine

This chapter presents the experimental results using the Ampair Wind Turbine. It starts with a selection of mainly experimental work related to the benchmark wind turbine, that was reported over the last years in literature. The contribution of this thesis is elaborated on thereafter. This includes an explanation of the substructuring task, followed by a description of the FE models and the measurement setup. Then, the performed measurements are analysed with respect to different excitations and their validity. Afterwards, the system identification steps are outlined, and finally, the substructuring results are presented and discussed.

4.1 Dynamic Substructuring of the Benchmark Wind Turbine

At the 29$^{\text{th}}$ IMAC in 2011, the SEM dynamic substructuring focus group agreed on using a common testbed structure, the Ampair A600 wind turbine. The turbine is a rather small but challenging structure and was described by Mayes [3] who also carried out first measurements of the whole wind turbine. Harvie and Avitabile [38] investigated different experimental setups for blade measurements. Initial thoughts and ideas on experimental substructuring applied to the testbed were further introduced by Mayes [39].

A thorough investigation of the blades by Gibanica et al. revealed a significant spread above 400 Hz [40]. In the paper, twelve blades were tested including the set of blades that is used in the present work. Moreover, Linderholt et al. [41] reported a rather large spread in the measurements of partly and completely assembled turbines from three universities applying both shaker and impact excitation.

Rahimi et al. [42] contributed to the decoupling of blades by measuring both one blade connected to a chopped off version of the clamp and the assembled rotor. The experimental models were coupled applying Lagrange Multiplier FBS (de-)coupling as well as an adaptation of the Interface Deformation Mode method to overcome the lack of rotational DOFs and to minimise the measurement noise. Furthermore, remarks and observations regarding the experimental setup can be found in their work.

First numerical efforts in decoupling the blades from the hub were made by Brunetti et al. [43]. Using dual FRF coupling by selecting a reduced set of interface DOFs, FE models of the hub and the blades were coupled. The same authors also coupled experimental models of mass-loaded blades to the hub [44].

The transmission simulator method was applied to the testbed structure by Macknelly et al. [45]. Here, a plate attached to the blades was chosen as transmission simulator. However, the obtained results were not satisfying. While emphasising the importance of the transmission simulator design, the brackets were suggested to be an adequate transmission simulator.

Useful insights regarding the driving-point were reported by Rohe and Mayes [17] who used the hub as transmission simulator to couple the rotor to the tower of the wind turbine. Recently, Roettgen and Mayes chose the hub as transmission simulator to arrive at a rotor model built from experimental blade models [18]. The same substructuring task will be carried out in this thesis, as elaborated on in the following section.

4.2 The Substructuring Task

In the present work, the goal of dynamic substructuring is to acquire a model of the rotor, also denoted three-bladed hub. Due to the aforementioned spread found in the blades, it is believed that a system built up by experimental models will outperform FE modelling with identical blades. Thus, three different blades will be measured and coupled to the hub in contrast to Roettgen and Mayes [18] who measured only one blade and coupled it three times.

In the subsequent, the term hub will be used to describe the actual hub assembled to the shafts and the brackets which connect the blades with the hub (see [3] for a description). This structure is believed to be an appropriate transmission simulator since it is stiff compared to the blades and offers enough locations to mount sensors that replicate the motion. Moreover, it inherently includes the joint properties because it is part of the assembled three-bladed hub.

The substructuring scheme is depicted in Figure 4.1. All three blades are separately assembled to the hub as transmission simulator and will be measured. For the one-bladed hubs, each blade is jointed to the same bracket it will be assembled to in the three-bladed hub. The measurement data will be used to identify experimental models, which in turn will be coupled in order to form the assembled structure. To obtain a valid model, the influence of the hub has to be removed twice which is done by means of the FE model.

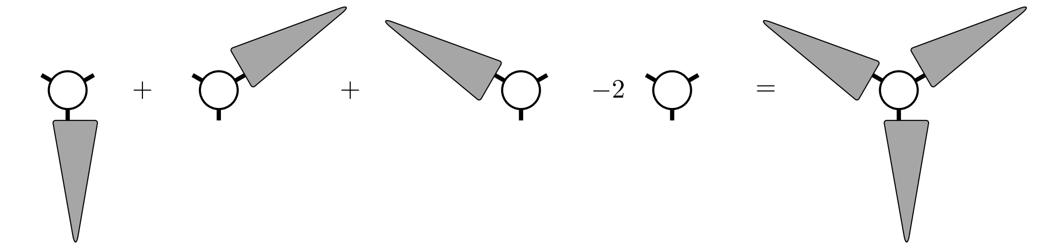

Fig. 4.1: *The substructuring task in this paper. Three one-bladed hubs are measured and coupled with two negative FE transmission simulators. The obtained coupled model of the assembled structure is compared with measurements and the FE model.*

Component	m (kg)
Hub with brackets and bolts	3.980
Hub with brackets without bolts	3.707
Three bolts with nuts and washers, averaged	0.030
One bracket with bolts and shaft, averaged [20]	0.432

Table 4.1: *Component masses of the rotor. The measurements were performed using a scale with a precision of 0.1 g.*

Since the transmission simulator is part of all models to be coupled, MCFS can be applied in all coupling steps. Thus, the need for discrete connection points is avoided, and a more realistic coupling configuration is achieved. To compare the coupled system, the assembled three-bladed hub is also measured.

The blades used in this work have the serial numbers 790, 828, and 850. To shorten the notation, the corresponding one-bladed hubs will be referred to with A, B, and C, respectively.

4.3 Finite Element Models

In this work, the FE models described by Gibanica [20] are used and solved with FEMAP v11.1.0 and NX Nastran. The blade model is built from a combination of solid and layered composite shell elements and is calibrated to one blade which was done by Johansson et al. [46] using destructive material testing. Thus, the model is calibrated to another blade than the ones used here.

The hub, shaft, and bracket were modelled using isotropic solid elements. The density of these components is chosen to match the measured weights listed in Table 4.1. Depending on the configuration, the density of the bracket changes to account for the mass of the bolts. If the hub is in an uncoupled configuration, the bolts are removed, lowering the density as can be seen in Table 4.2. Furthermore, the number of elements and nodes of the FE models is specified in that table.

The interfaces; bracket - blade, shaft - bracket, and shaft - hub; are modelled as flexible connections using the CWELD element of NASTRAN [47] which tends to overestimate the stiffness of the actual connection

Component	Nodes	Elements	ρ (kg/m^3)
Hub	18246	11036	2095
Bracket and shaft without bolts	33443	20126	4050
Bracket and shaft with bolts	33443	20126	5000
Blade	20517	95897	see [46]

Table 4.2: *Properties of the FE models. The densities are calculated such that the FE models match the measured weights listed in Table 4.1.*

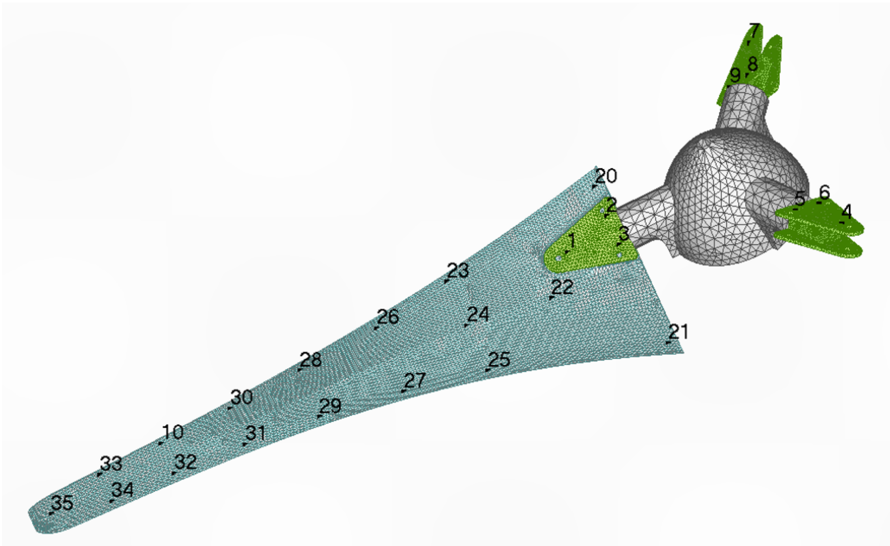

Figure 4.2: *FE model of the one-bladed hub showing the sensor locations both on the blade and the hub. Sensors 11 to 19 are mounted on the back side of the hub and the sensors 1 to 10 are triaxial.*

	Model number	Sensitivity	transverse sensitivity (%)	m (g)
Uniaxial sensor	PCB 352C22/NC	1 mV/(m/s^2)	< 5	0.5
Triaxial sensor	PCB 356A03	1.02 mV/(m/s^2)	< 5	1.0
Impact hammer	PCB 086C03	2.25 mV/N	-	-
Force transducer	Brüel & Kjær 8203	3.3 pC/N	-	3.2

Table 4.3: *Specifications of the measurement equipment including sensors, impact hammer and force transducer.*

between blade and hub. Damping is not included in the FE models. Figure 4.2 shows the one-bladed hub FE model, while the the hub itself and the three-bladed hub are shown in Figures 4.3 and 4.4.

4.4 Experimental Setup

The measurements were performed at the Chalmers Vibration and Smart Structures Lab using a data acquisition system which was developed by National Instruments. Simulating free-free boundary conditions, the structure was hung with fishing lines (see Figure 4.5). It was attempted to have the fishing lines as long as possible in order to reduce the resonance frequency of the rigid body modes. Furthermore, the lines were connected to the suspending structure with springs. Since the edge of the hub hole is sharp, metal wire was used to attach the fishing lines to the structure. The blades were assembled to the bracket applying a bolt tightening torque of 16 lbf-ft (21.69 Nm) according to the the assembly specifications [48].

The three-bladed hub was equipped with 9 triaxial sensors and 24 uniaxial sensors and the one-bladed hub with 10 triaxial and 25 uniaxial sensors. From these configurations, the mass loading was 21 g and 22.5 g for the one-bladed and three-bladed hub, respectively, which was considered negligible. Table 4.3 lists the specifications of the measurement equipment including sensors, impact hammer and force transducer. Great care was taken to align the triaxial sensors with the local FE coordinate system, and the sensors were glued to the structure.

The conditioning of the mode shape matrix is greatly influenced by the sensor placement on the transmission simulator [14]. Therefore, the placement was tested beforehand using numerical models, considering sensor configurations on either bracket, hub, or both. It was found that the sensor placement in Figures 4.2 to 4.4 was best with respect to both the condition number and the results using simulated data considering the number of available sensors. Three triaxial sensors were placed on the front side of each bracket close to the bolts and three uniaxial were mounted at the same locations on the bracket's opposite side (see Figure 4.3). Sensors labelled with a number from 1 to 9 are triaxial sensors. The sensor locations on the blade were chosen among the positions defined by Harvie and Avitabile [38] and, for the the whole three-bladed hub, distributed over the structure such that the symmetry is not disturbed.

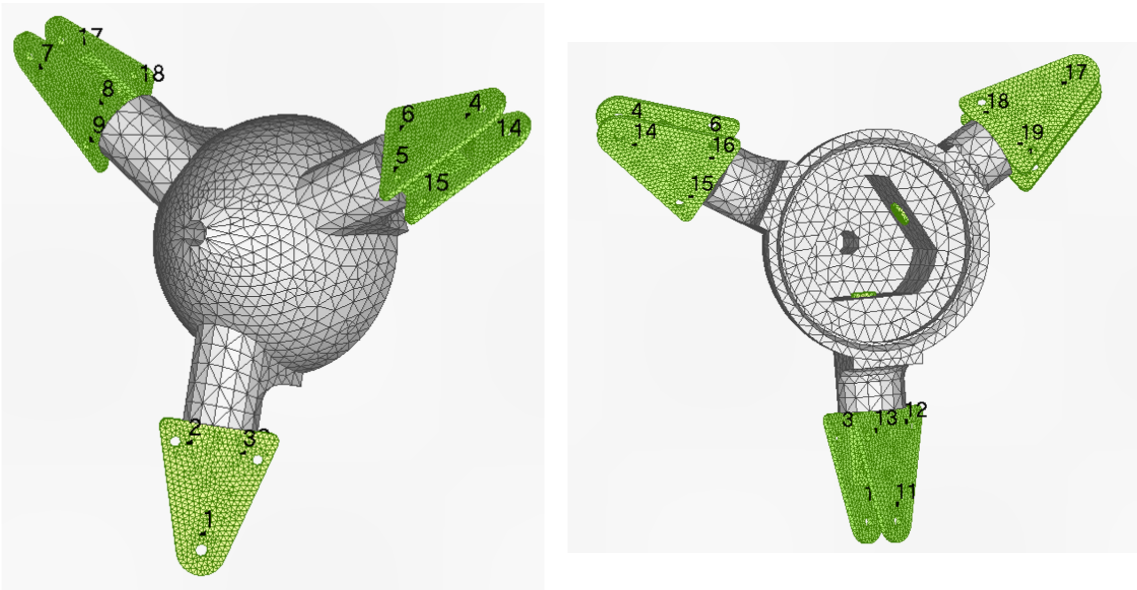

Figure 4.3: *FE model of the hub with sensor locations as used in the measurements of the one-bladed hub. On the front side of the hub, three triaxial sensors are mounted on each bracket (sensors 1 to 9). Nine uniaxial sensors are placed at the same locations on the opposite side (sensors 11 to 19).*

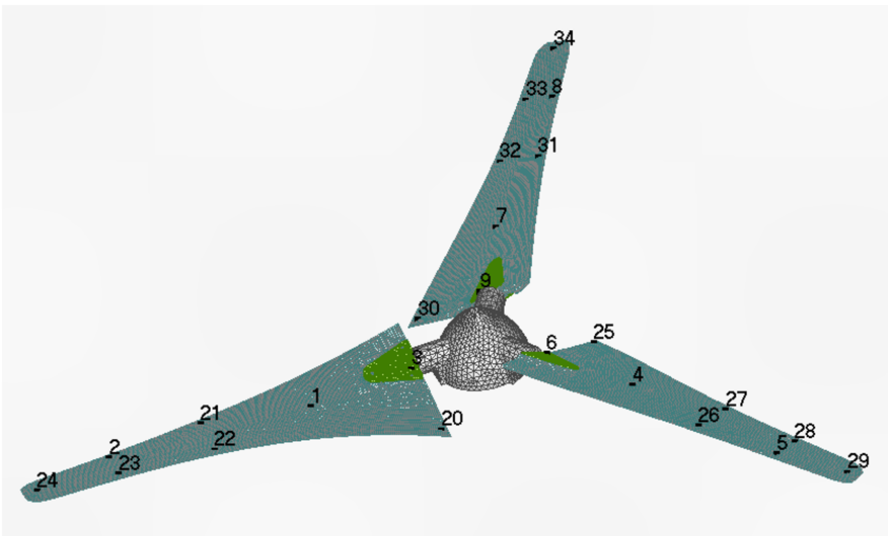

Figure 4.4: *FE model of the three-bladed hub showing the sensor locations both on the blades and the hub. Sensors 11 to 19 are mounted on the back side of the hub and the sensors 1 to 9 are triaxial.*

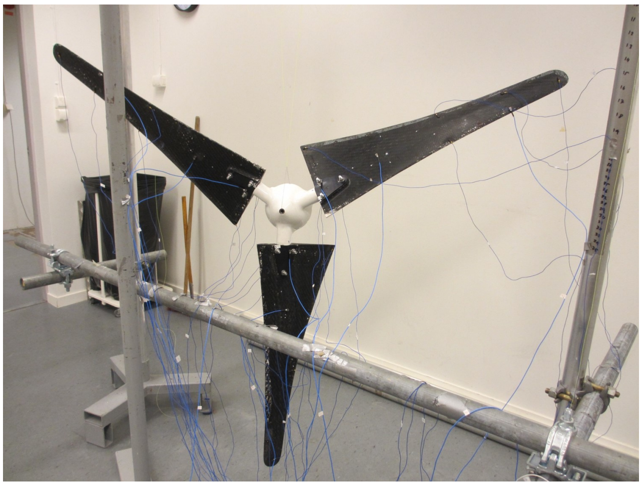

(a) *Three-bladed hub without shaker*

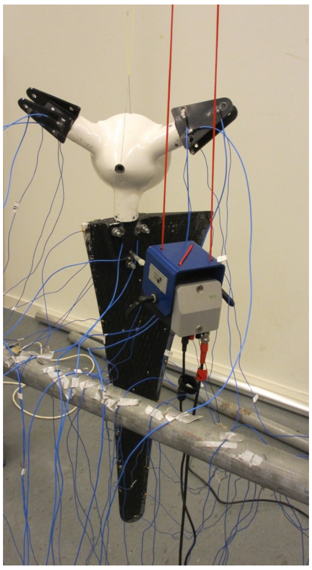

(b) *One-bladed hub with shaker*

Figure 4.5: *Measurement setup. The shaker is hung in strings while the structure is hung utilizing a metal wire and fishing lines.*

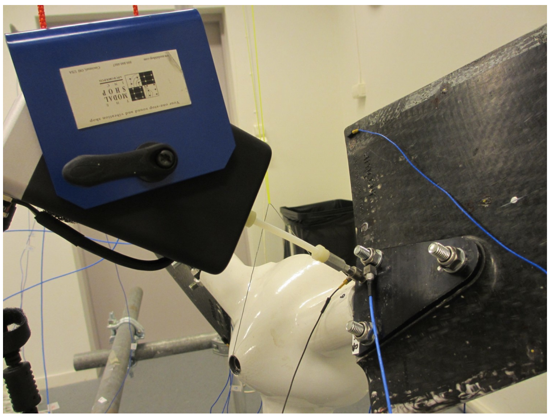

(a) *Three-bladed hub*

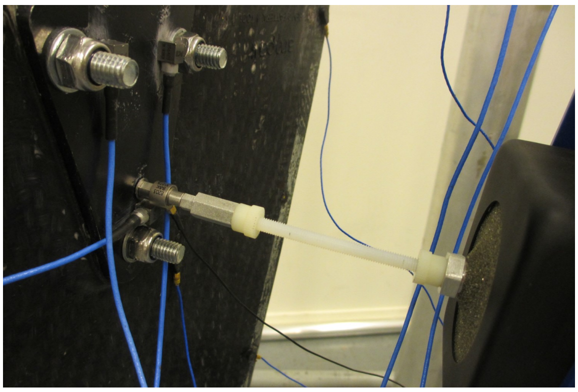

(b) *One-bladed hub*

Figure 4.6: *Attachment of the stinger. The stinger is mounted via a fastener and a force transducer to the bracket next to the sensor. For the three-bladed hub, three input locations were measured, whereas only one input was applied to the one-bladed hubs.*

For the excitation, both a shaker and an impact hammer with a hard metal tip were utilized. First, hammer testing was performed to find the best driving-point locations. All tested locations were chosen to be on, or close to, the bracket since excitation close to the tip of the blade may evoke measurement errors like double hammering due to large deflections [17]. The best input locations were found at positions 3, 6 and 9 for the three-bladed hub and 1, 4 and 7 for the three one-bladed hubs A, B, and C, respectively. For the first structure, three input locations were chosen in order to excite symmetric mode shapes, whereas for the latter, one input per blade was considered to be sufficient. Only out-of-plane excitation was applied.

The shaker used, model K2007E01 purchased from The Modal Shop Inc., was hung in strings. Its threaded nylon stinger of approximately 85 mm length was attached via a fastener and force transducer glued to the bracket as shown in Figure 4.6. Great care was taken to align the stinger. Since the measurements were performed using a force cell and a set of accelerometers only, the fastener needed to be mounted next to the sensor. In fact, the location was in the direction of the hub as can be seen in Figure 4.6. Impact hammering was performed using the same location as for the fastener before the latter was attached.

Shaker testing was carried out with chirp, multisine, and random excitation. Chirps with different amplitude levels were generated to find the linear range in the system and ensure repeatability of the tests. Low level multisine excitation was then performed to obtain the lowest noise level possible. For the sake of comparing different input types, the structure was also excited with low level random signals.

In the following, the specifications of the generated signals are listed. All measurements were sampled with 10 kHz. For the rotor, the frequency range of interest was chosen from 5 Hz to 400 Hz whereas data in the range of 10 Hz to 800 Hz was recorded for the one-bladed hub. The multisine was performed with 2500 frequency lines, distributed as suggested by Khorsand et al. [49]. Ten frequencies are superposed at a time, and ten complete cycles of the largest period are collected after stationarity is reached, again after Khorsand et al. Chirp signals are rapid sine sweeps [29] and were applied for 15 s. A 5 s pause was set between two chirps. For each curve, 15 repeats were averaged. The random signal was normally distributed and averaged over 60 measurements with a signal duration of 8 s and a pause time of 10 s, while the impact signal was recorded over 10 s.

4.5 Analysis of the Measurements

When comparing the different excitation types, it was observed that impact testing yielded the highest noise level. Especially the phase captured by the bracket sensors in the in-plane direction were very noisy since the measured acceleration of the brackets was rather small, thus the low signal to noise ratio. In contrast, the noise level for the sensors mounted on the blade was lower. Moreover, impact testing presumably caused overloading in sensors 20 and 21 for all one-bladed hubs. However, this type of impact excitation is fairly easy and quick to perform since no stinger has to be attached, avoiding the cumbersome stinger alignment. Furthermore, the system is not changed by attaching the stinger. Several driving-points were excited and the system was found to be reciprocal.

One drawback of impact hammering is the limited force control which restricts the suitability for non-linearity checks. Thus, these checks were made with chirps which provoked less noise than impact testing. Chirps as well as random signals require a significantly shorter measurement time compared to the multisine. However, the results of the random testing suffer from noise which could be prevented by a higher number of repeats. Therefore, the measurements of the bracket sensors were impaired with noise and outliers, comparable with impact testing. The fourth applied excitation type, multisine, yielded almost noise-free signals, although the chosen settings caused a minimum measurement duration of 90 minutes to perform one measurement. Hence, only one multisine was applied per blade.

In the following, observations made during the measurements are reported. Figure 4.7 shows the direct accelerance FRF of all three one-bladed hubs obtained with the multisine. A large spread is observed which resembles the deviations found by Gibanica et al. [40]. The first two modes correlate rather well but then, the FRFs start to deviate. Especially structure A differs from the other two one-bladed hubs. Note the large spread between 400 Hz and 600 Hz, which will be elaborated on later in the section.

The system changes due to the stinger attachment are assessed based on the information in Figure 4.8, which shows multisine and impact measurements for the three one-bladed hubs. The resonance frequencies shift to higher frequencies as a result of the added stiffness of the stinger. This effect is most pronounced for the bracket sensors and, according to Figure 4.8, for structure A. In total, the stiffening is regarded to be negligible in the frequency range of interest.

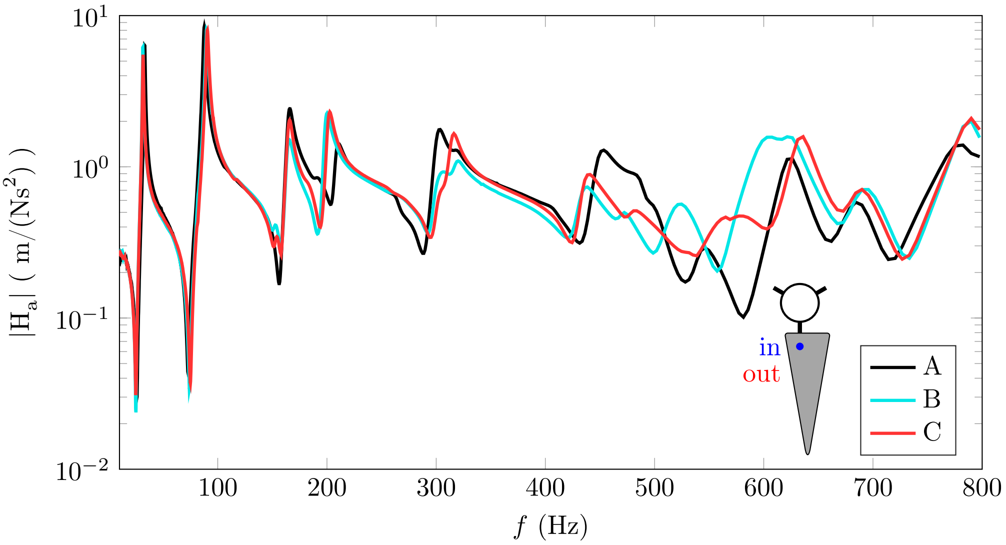

Figure 4.7: *Multisine measurement FRFs of all one-bladed hubs. The direct accelerance FRFs reveal the spread between the blades and deviation between 400 Hz and 600 Hz. Multisine excitation is applied at the input locations 1z, 4z, and 7z, for the structures A, B, and, C, respectively, which are indicated in the sketch of the wind turbine.*

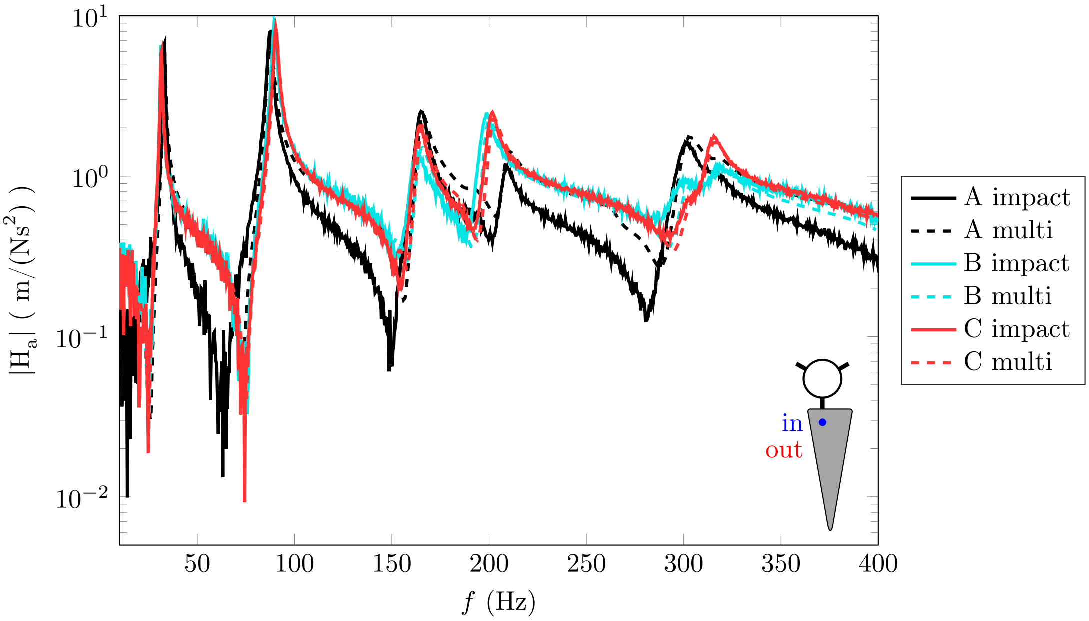

Figure 4.8: *Direct accelerance FRFs for all blades to show the effect of the stinger. Multisine and impact measurements are compared at the input locations 1z, 4z, and 7z, for the structures A, B, and, C, respectively. The effect is most pronounced for structure A.*

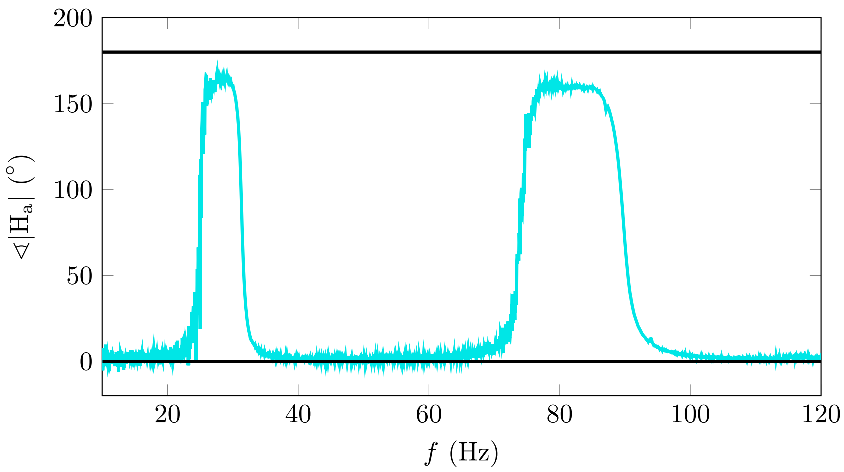

Figure 4.9: *Impassivity due to noise. The phase of the direct accelerance for the structure B indicates impassivity for every frequency line with a negative phase as shown by example of a chirp measurement.*

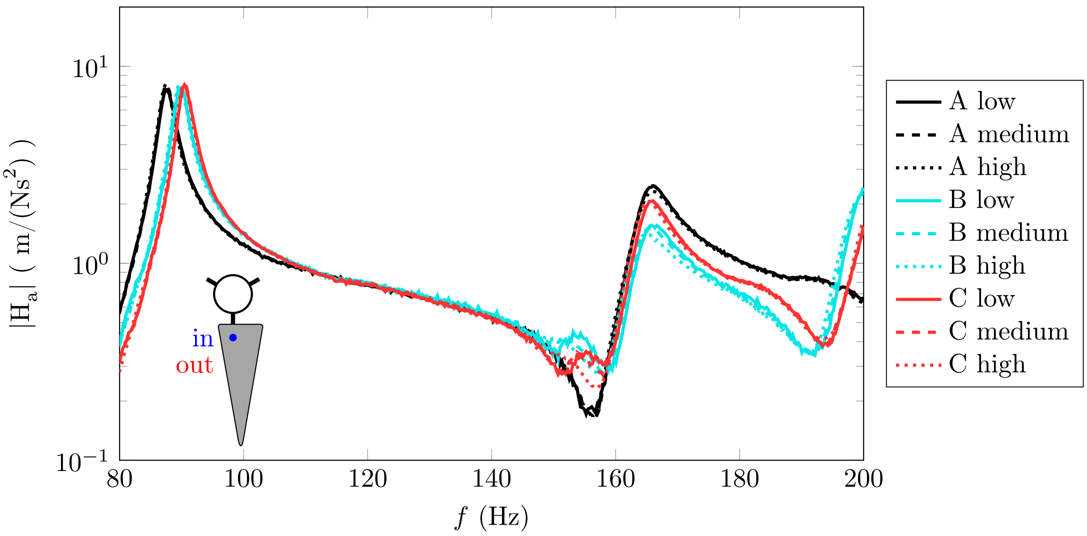

Figure 4.10: *Non-linearities in the blades shown by means of chirp measurements with different amplitude levels for all blades. Here, the minor frequency range 80 Hz - 200 Hz is shown with direct accelerance FRFs at the input locations 1z, 4z, and 7z.*

Noise is present and was found to be one cause of measurement distortion as can be seen in Figure 4.9. For low frequencies, the phase oscillates around 0°, turning the system impassive for every frequency line with a negative phase. Recall that the phase of an accelerance FRF for passive systems should be between 0° and 180°. Later, passivity will be enforced on the identified models to overcome the measurement errors.

Moderate non-linear effects were found in the measurements using chirp excitation with different amplitude levels. Figure 4.10 shows a FRF detail including the second and third flexible mode of all three one-bladed hubs. At the different force levels, the peak height as well as the resonance frequency changes, especially for the third mode. Similar non-linear behaviour was found at driving-points on the blade close to the bracket, e.g. next to sensor 22. Hence, it was concluded that excitation near the bolts on the brackets is comparable to excitation locations on the blade close to the brackets. Furthermore, the lowest force level was chosen as the amplitude for the multisine measurements to suppress non-linearities as much as possible.

As noted earlier, the chirp measurements revealed large deviations in the frequency range between 400 Hz and 600 Hz which becomes evident in the comparison of different amplitude levels. Above 600 Hz, the measurements coincide again. By way of example, Figure 4.11 shows the direct accelerance FRF of the one-bladed hub C. The deviations are most pronounced for this blade. Here, not just results from different excitation levels differ but also two measurements, both taken at the medium level. For the other blades, the deviations seem to be a

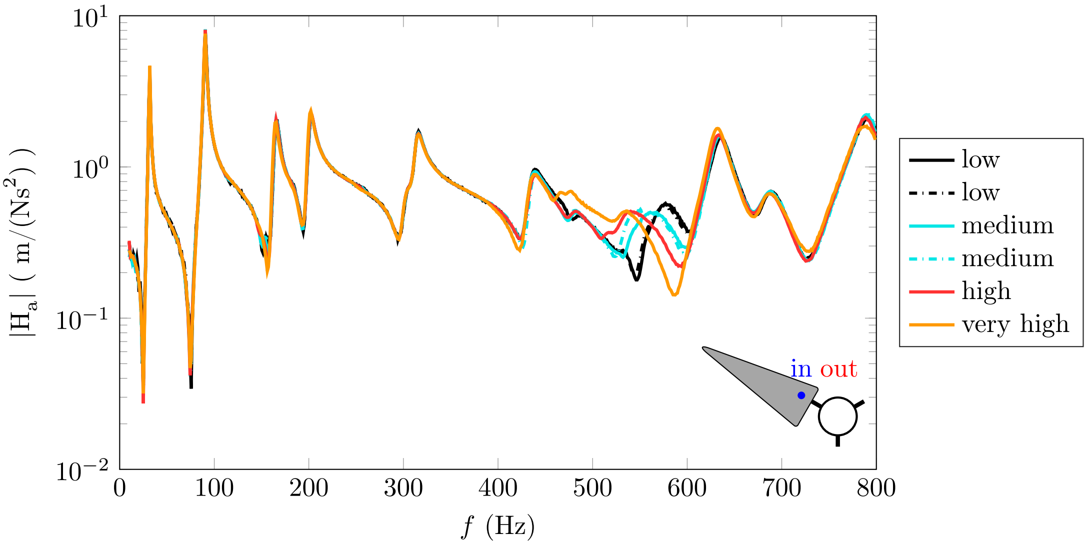

Figure 4.11: *Direct accelerance chirp FRFs for structure C (input/output location 7z) exemplifies the found deviations between 400 Hz and 600 Hz, both for different amplitude levels and for repeated measurements. Below and above this frequency range, the curves coincide.*

function of the amplitude level, possibly indicating a non-linearity. With impact excitation, these effects are significantly reduced, appearing only for sensors mounted on the blade. Random tests provoke no deviations but a higher noise level for this frequency range which in turn yields impassivity. Note that random excitation was only performed at one amplitude level and hammering was performed such that the force level is approximately equal for all measurements. A possible explanation will be given in Section 4.8.

Similar issues were also observed for the three-bladed hub. Figure 4.12 shows a comparison of chirp excitations with different amplitude levels. Non-linear effects are indicated by the peak height around 70 Hz, and larger deviations between the measurements are present between 250 Hz and 270 Hz.

4.6 System Identification

System identification is a crucial factor in experimental dynamic substructuring since the models need to be valid representations of the physical structures. Otherwise, errors amplify during the coupling procedure. In order to compare the coupling results and to choose the best model possible, different models were identified from the measurements in this thesis. Both measurement data obtained from different excitation types and different system identification procedures were utilized.

4.6.1 The One-bladed Hub

Most one-bladed hub models were identified using a manual procedure. First, the influence of the rigid body modes was removed from the measurement data using a synthesised FRF stemming from the FE model. Then, the measurements of the one-bladed hub obtained with multisine excitation were plotted as in Figure 4.7. Initial models were identified by varying the number of states which is the only user-defined input in the system identification procedure `n4sid`. These models were compared to the FE model and any modes that occurred neither in any of the other experimental models nor in the FE model, were discarded. At the end, 14 modes from 10 Hz to 800 Hz were retained. However, one of these modes at around 400 Hz is believed to be potentially spurious. A distinct peak can be found in all measurements but the MAC value for the three experimental models and the FE model is poor. To identify models that do not include any spurious modes, the measurement data was split in smaller frequency ranges and the number of modes in each interval was predefined.

Since the measurements proved to be unreliable above 400 Hz, the focus during system identification was on data up to 400 Hz. Therefore, a model including only eight modes was identified. The eighth mode is added to account for the high frequency residuals, such that the FRFs match well within the chosen frequency range. Subsequently, this model will be referred to as *multi*. Another model, dubbed *multi300*, was identified

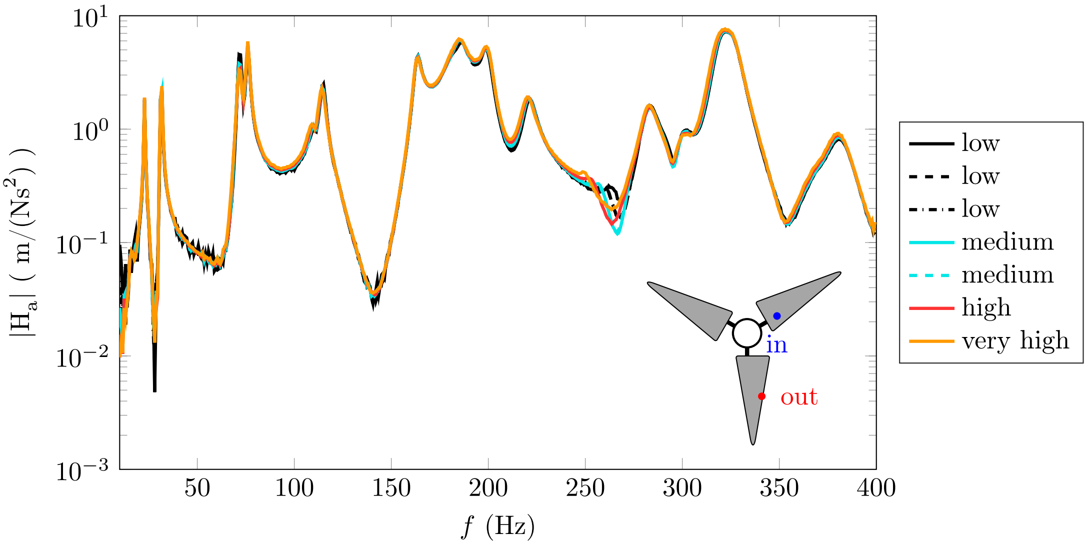

Figure 4.12: *Accelerance FRFs of the three-bladed hub's chirp measurements for different amplitude levels. The input location is at location 6z, the output sensor at position 22. Deviations between the measurements can be found around 70 Hz and between 250 Hz and 270 Hz.*

using only data up to 300 Hz in order to investigate the number of modes included in one-bladed hub models necessary for good substructuring results. Accordingly, the models using the full data set are denoted *multi800w* and *multi800wo* including and excluding the mode around 400 Hz, respectively. They were identified to judge the influence of the deviations between 400 Hz and 600 Hz for high frequencies.

The other system identification method used is the automated procedure by Yaghoubi and Abrahamsson [32]. To obtain the model *auto*, data up to 400 Hz was taken into account. However, the method identified few spurious modes which were removed manually.

To compare the different excitations, models from impact and random testing were manually identified, again with data up to 400 Hz, dubbed *impact* and *random*. Finally, the state-space model *multi* was transformed to second-order modal form to enable CMS as sketched in Section 2.4.

During system identification, deficiencies in signals for certain sensors were revealed. For instance, the first two modes were missing in the data of sensor 24 for the one-bladed hub C. Based on the visual inspection of the mode shapes, sensors 24, 27, and 31 of structure A were discarded, while sensors 24, 26, 28, and 31 were discarded for the structures B and C. Then, system identification was repeated which substantially improved the identified models and their mode shapes.

The identification procedure described above was done with accelerance data, since it yielded the best model for the overall range. The models were then transferred to mobility data, and Maxwell's reciprocity theorem was used to obtain the unmeasured FRFs, using the information of one input and all output channels. Subsequently, all models were assessed with respect to their physical properties. More precisely, passivity and the product $\boldsymbol{CB}$ were analysed. Especially the high frequency modes may disobey these properties, since they do not necessarily have a physical meaning but rather account for high frequency residuals. Passivity was enforced for all channels following the method mentioned in Section 2.5.

Afterwards, the models were transformed to receptance outputs, and the adherence to Newton's second law was checked. Since $\boldsymbol{D}$ was enforced in the system identification procedure, this checks includes the condition $\boldsymbol{CB} = \boldsymbol{0}$ only. The absolute value of the maximum entry of $\boldsymbol{CB}$ was of order 10^{-4}, which was found to be small enough to obtain physical results after coupling. Finally, the rigid body modes of the FE model of the one-bladed hub were added. Therefore, the eigenvalue problem for the FE models was solved, and the resonance frequencies and mode shape vectors corresponding to the six rigid body modes were extracted. Since damping is not included in the FE models, it was chosen to be $\xi = 0.1$ % for all rigid body modes.

Figure 4.13 exemplifies the identified models using multisine and impact data for the structure C. The multisine measurement yields a smooth curve which simplifies identification. However, the rather high noise level of impact testing is levelled out during system identification as long as the noise is random. Moreover, the very noisy signals of the bracket sensors, as mentioned in the previous section, do not affect identification

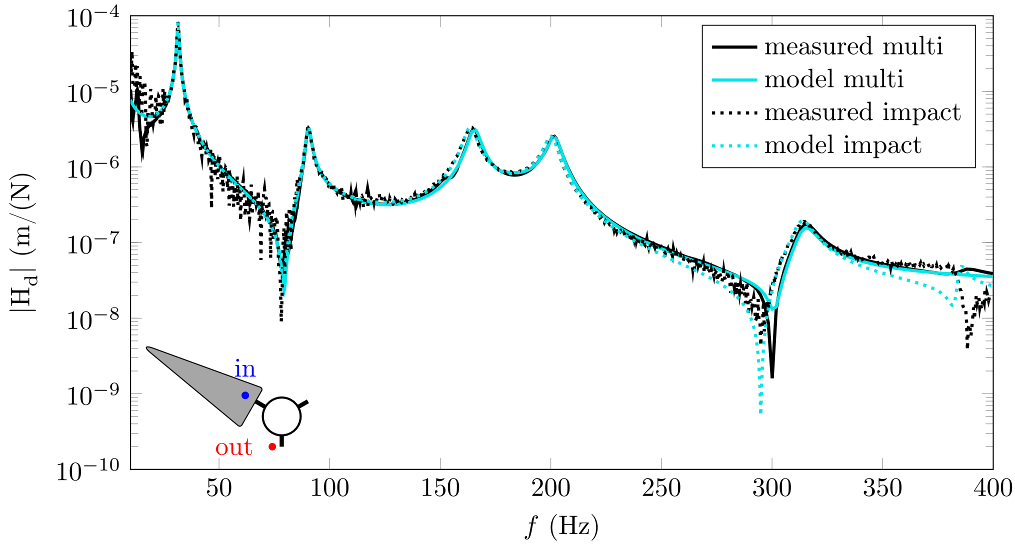

Figure 4.13: *Comparison of measurement and identified models of structure C, using impact and multisine excitation. Receptance FRFs are shown for the input at position 7 in z-direction and output sensor at location 11 at the back side of the bracket. The measurements are well represented by both models.*

	FE	A		B		C		description
		multi	impact	multi	impact	multi	impact	
	f_i (Hz)	f_i (Hz)	f_i (Hz)	f_i (Hz)	f_i (Hz)	f_i (Hz)	f_i (Hz)	
7	30.32	33.11	33.06	31.38	31.41	31.51	31.48	1st bending mode
8	89.72	87.57	87.24	89.75	89.48	90.42	90.25	2nd bending mode
9	180.90	165.27	164.58	164.89	161.59	165.40	163.44	3rd bending mode plus edgewise
10	191.46	190.72	189.02	176.01	180.25	178.87	181.52	1st edgewise bending mode
11	234.06	208.83	207.69	199.36	197.62	201.68	200.28	3rd bending mode plus in-plane
12	330.78	300.84	299.99	301.14	296.91	302.01	300.93	4th bending mode
13	341.88	316.97	315.88	317.94	315.70	314.53	313.41	2nd edgewise bending mode
14	475.64	450.42	422.89	410.54	379.99	448.20	384.80	5th bending mode

Table 4.4: *Identified resonance frequencies for the one-bladed hubs. The models* impact *and* multi *are compared to the FE model. Furthermore, a brief description of the FE mode shapes is given.*

significantly, since the procedure gives more weight to channels with larger signal amplitudes. In conclusion, both models represent the measurement data well.

The identified modal parameters of the two models can be found in Tables 4.4 and 4.5. A comparison of all identified models can be found in the Appendix B in Tables B.1 to B.6. As expected, the identified resonance frequencies with impact testing are lower than with shaker testing probably due to the added stiffness of the stinger, yielding a maximum difference of about 2 %. The only exception is the tenth mode which has a higher resonance frequency in the impact model. However, this mode is highly damped and almost not visible in the FRFs, hampering correct identification. Starting from the third flexible mode, the identified resonance frequencies are lower than their FE counterparts. This may be due to the over-estimated stiffness in the interfaces between brackets and hub.

A MAC value comparison for the first eight flexible modes is shown in Figure 4.14. Here, the multisine models for the one-bladed hubs as well as the FE model and the impact model of structure A are plotted. Since the impact and the multisine model exhibit high correlation for all one-bladed hubs and all modes, the MAC plots of the other impact models are not shown here. It can be seen that all identified models correlate well. Furthermore, the first four measured modes are well captured, whereas higher modes are not well represented in the FE model.

	A		B		C	
	multi ξ_i (%)	impact ξ_i (%)	multi ξ_i (%)	impact ξ_i (%)	multi ξ_i(%)	impact ξ_i (%)
7	1.34	1.07	1.33	1.12	1.50	1.21
8	1.24	1.37	1.32	1.17	1.22	1.23
9	1.71	1.76	1.69	2.29	1.59	1.71
10	2.30	2.41	4.84	2.75	3.24	2.46
11	1.68	1.62	1.52	1.61	1.48	1.47
12	1.79	1.93	2.35	3.21	2.21	2.45
13	1.89	1.88	1.77	1.82	1.48	1.41
14	12.90	3.94	14.65	2.46	12.47	0.46

Table 4.5: *Identified modal damping for the one-bladed hubs. The models* impact *and* multi *are compared. Damping was not included in the FE model. The mode 14 is an unphysical mode, added to account for high frequency residuals.*

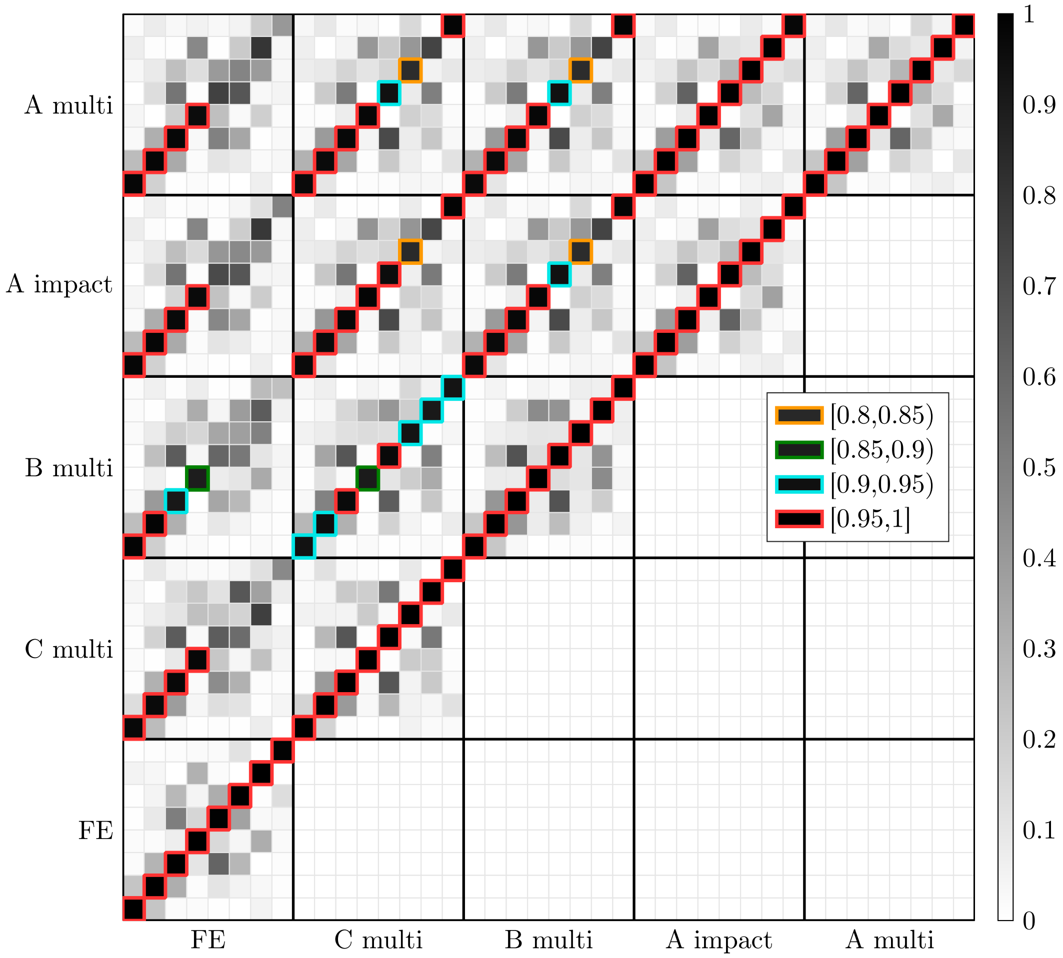

Figure 4.14: *MAC value comparison for the one-bladed hubs including the first eight flexible modes. The multisine models are compared to one impact model and the FE model. The identified models correlate well for all modes but only the first four modes are captured by the FE model.*

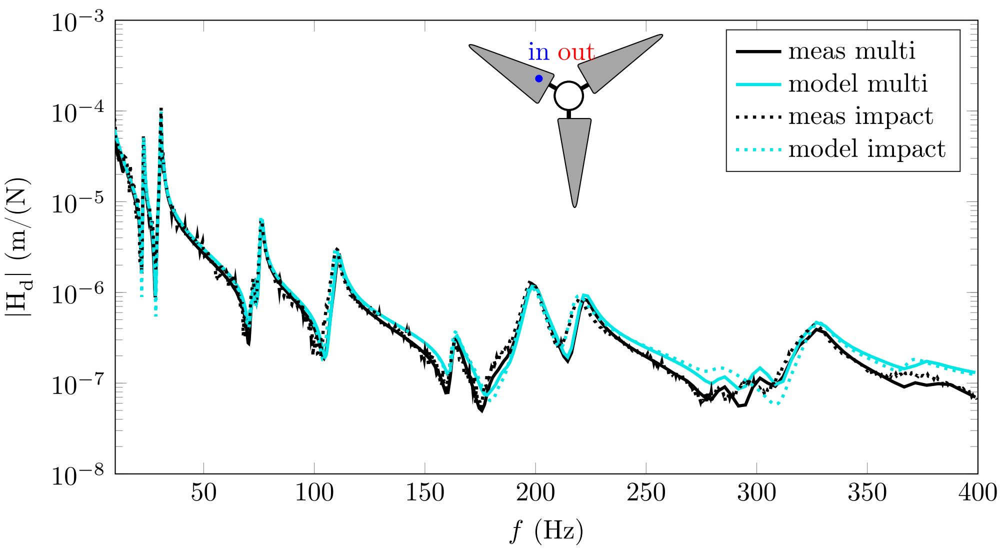

Figure 4.15: *Comparison of the measurement and the identified models for the three-bladed hub, using impact and multisine excitation. Direct receptance FRFs are shown for the input/output at position 9 in z-direction.*

4.6.2 The Three-bladed Hub

Lastly, models for the three-bladed hub were identified using both multisine and impact testing and the procedure explained in the previous section. The measurement data obtained with the three inputs were combined and identified together in order to enable identification of the symmetrical modes. Figure 4.15 shows again a comparison of multisine and impact measurement with the corresponding identified models by means of one representative channel. The measurements are well captured up to 200 Hz which corresponds to twelve flexible modes. For higher frequencies, the models start to deviate. Figure 4.16 shows a MAC value comparison for the two identified models with the FE model. Here, the first 15 flexible modes are plotted.

Due to the symmetry of the structure, these modes can be batched in groups of three. The modes in the second and fourth group are all close in frequency corresponding to symmetric mode shapes, whereas only two modes are close in frequency for the other groups. As explained in Section 2.6, the angle between subspaces is more informative for these modes than the MAC metric. The coloured frames added to the MAC plots take these angles into consideration. The colour is based on the squared cosine of the angle and corresponds to the intervals of the MAC values.

Applying this metric, the first twelve flexible modes of the multisine model correlate well with the FE model, although all symmetric FE modes are mixed up compared to the identified model. Only the first nine modes are captured with the impact model. Furthermore, the two identified models are alike except for the fourth mode shape group. In Tables 4.6 and 4.7, the identified modal parameters and the associated errors for the three-bladed hub are listed. Note that the order of the FE modes is changed taking into account the mode mix-up. Interestingly enough, the resonance frequency of the identified models matches the first FE resonance frequency almost perfectly, even though the first resonance frequency of each one-bladed hub is higher than in the corresponding FE model. The second and third resonance frequencies are slightly higher than in the FE model, whereas all other modes are stiffer in the FE model compared to the identified models. This might be due to the overestimated stiffness in the connection between brackets and hub. In the following, the multisine model will be used as the reference for the true system and referred to as measurement in the plots.

4.7 Substructuring Results

The first flexible mode of the FE hub is above 1700 Hz, which is far above the frequency range of interest. Therefore, the transmission simulator is treated as rigid, which yields a full rank mode shape matrix with six columns. The number of rows is 36 which corresponds to nine triaxial and nine uniaxial sensors. The condition number is 1.9 for this matrix. In the following, the substructuring results with state-space coupling will be presented.

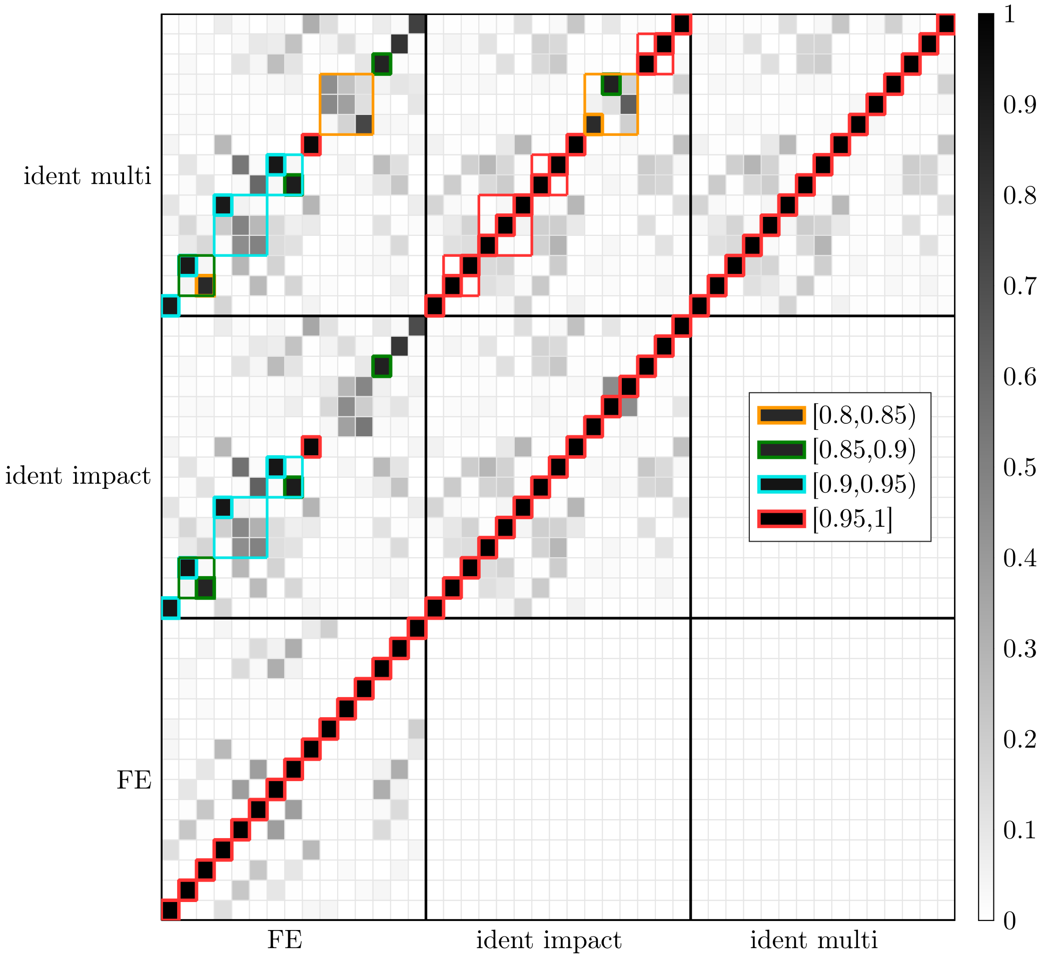

Figure 4.16: *MAC value comparison for the identified three-bladed hub including the first 15 flexible modes. The multisine and impact models are compared to the FE model. The coloured frames are connected to the angles between the subspaces spanned by the mode shape groups.*

To assess the results, direct accelerance FRFs of the coupled and identified models will be used. If the substructuring is successful, the FRFs should resemble each other over the whole frequency range. Moreover, the curves must overlay for low frequencies, since $H_a(\omega = 0)$ for direct FRFs corresponds to the inertia properties of the system, which are essential for a valid model. The latter criteria is fulfilled for all investigated models.

One of the most defective substructuring results was obtained for channel 20. Here, the differences between the coupled modes is visualized clearly, as done in Figure 4.17a. Investigating the substructuring results, this channel reveals problems for the models *multi800w* and *multi800wo*. Both models show an upward trend in the FRFs associated with this channel which is not present in the measurements of the assembled system. Note that only the model *multi800wo* is shown since the two models yield very similar FRFs. The same trend is also present in the model *auto*, whereas the model *multi* follows the true FRF. A possible explanation might be the influence of torsional or in-plane motion which is likely to be larger for this sensor location than for locations closer to the blade's axis. These motions are difficult to capture with the chosen measurement setup. Recall that the sensor location at the upper right corner of the blade has already been identified as fault-prone from the measurements and is sensitive to torsional and in-plane motion,.

The model *multi* as well as the other investigated models *impact* and *random* capture the higher frequencies better, even though they differ substantially above 200 Hz (see Figure 4.17b). The model *multi300* is able to replicate the motion up to 220 Hz. Then, the FRF differs significantly indicating that too few modes are included in the model.

If channels closer to the blade tip are investigated, the substructuring results are remarkably better as shown in Figure 4.18a. Even with the model *multi300*, satisfying results for channel 24 are obtained up to 400 Hz. In the figure, the models *multi800w*, *multi800wo*, and *auto* are not shown. However, the results obtained with these models are also satisfying for this channel.

The best results are obtained with the models *multi* and *impact* which yield equally good FRFs. In fact, Figure 4.18a indicates that the impact model yields the best results since it deviates the least up to 150 Hz. This conclusion can be drawn for most channels. However, for the upper right blade corner as shown in Figure 4.17b, the *multi* model replicates the identified system better.

Table 4.6 compares the modal parameters of these two models with the identified and FE system for the first 15 flexible modes, while the calculated errors are listed in Table 4.7. The predicted parameters for the other models can be found in the appendix in Table B.7. In general, all coupled models represent physical systems since they are passive and $\boldsymbol{CB}$ is sufficiently small. Furthermore, no complex resonance frequencies of the substructured system were found. Thus, the mass and stiffness matrix are positive definite and semi-definite, respectively, after coupling.

Compared to the true, identified system, all resonance frequencies are estimated satisfactorily with a maximum error of 8 %. However, damping is clearly overestimated. It seems as if the impact model can reproduce the real damping slightly better since the errors of most modal damping ratios is smaller compared to the *multi* results. Moreover, the maximum modal error for the *multi* results is 124 %, compared to 59 % for the *impact* model.

The resonance frequencies obtained with substructuring are closer to the true system than the nominal FE model, except the first resonance frequency. Thus, using experimental models to build up the model of the assembled structure is shown to be superior to the nominal FE model used for the present substructuring task.

The MAC value comparison between the two substructured models and the identified system is shown in Figure 4.19. Again, the frames indicate the angle between the subspaces. The first three groups are captured well for both models. The *multi* results are also able to replicate the fourth mode group. In Figure B.1 in the appendix, the mode shapes obtained with the substructured models *multi* are shown. Here, the symmetric mode shapes become apparent.

So far, all presented results are obtained using state-space synthesis. To prove that all methods yield the same results, the model *multi* was transformed to second-order modal form, and a FRF was synthesized. Then, both CMS and FBS were used to repeat the substructuring task. As can be seen in Figure 4.18b, the methods do indeed yield the same FRF. Minor deviations in the estimated resonance frequencies or modal damping between CMS and state-space were found but are put down to numerical errors. Note that FBS was only performed with synthesised data, not with measured FRFs, since only one input was used for the measurements. Reciprocity could be used to retrieve all necessary FRFs of the measurement points on the transmission simulator needed for the coupling procedure but was here only applied on the identified system. Furthermore, the FRF of the FE model is shown in Figure 4.18b. Again, it becomes evident that the substructured model estimates the true system better than the nominal FE model. To plot the FE FRF, the identified damping rations of the model *multi* are applied to the FE model.

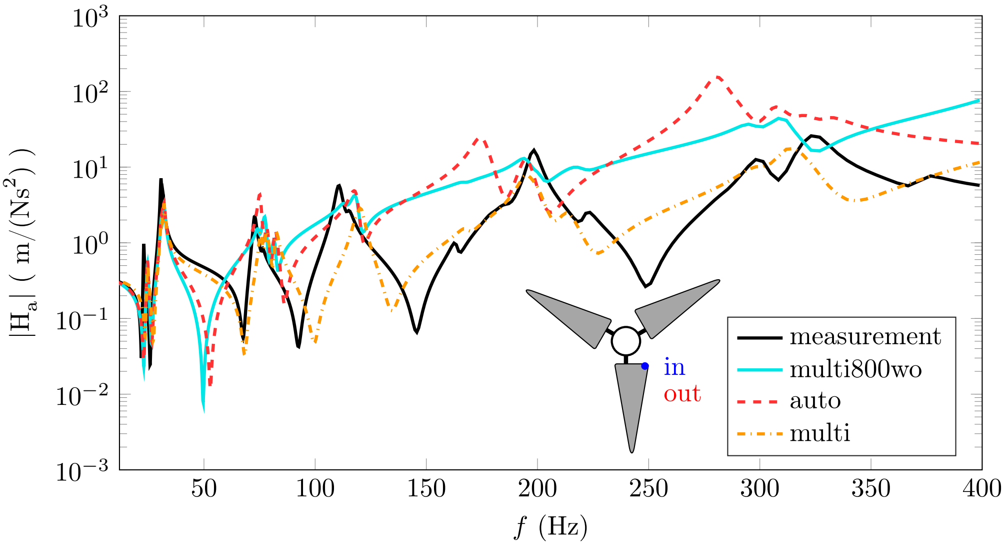

(a) *Models* multi, auto, *and* multi800wo

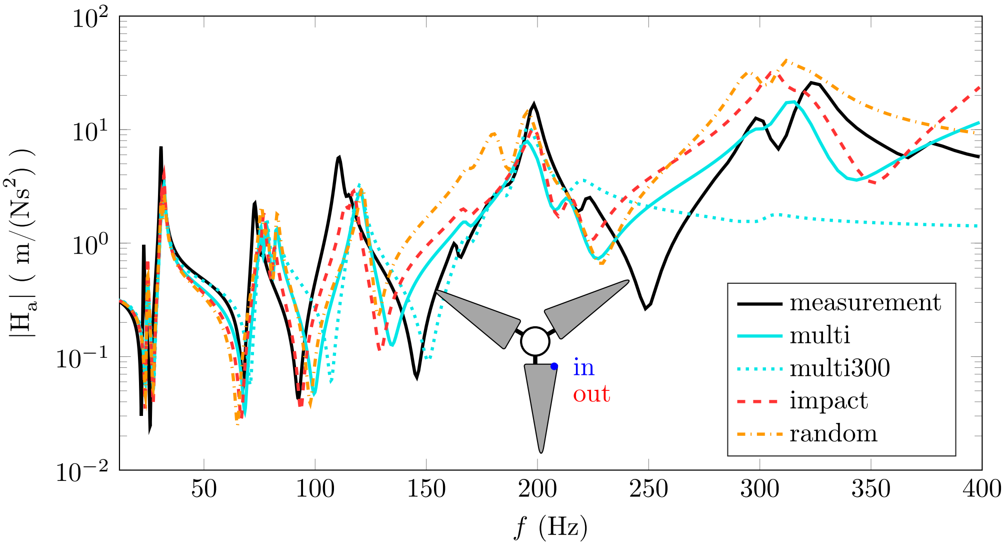

(b) *Models* multi, multi300, impact, *and* random

Figure 4.17: *Direct accelerance FRF of the three-bladed hub for the input/output location 20. The identified measurement model is compared to the models* multi, auto, *and* multi800wo *in the upper figure and to the models* multi, multi300, impact, *and* random *on the lower figure. The models* auto, *and* multi800wo *show a wrong upward trend, while this does not hold for the models in the lower figure. The model* multi300 *cannot capture the whole frequency range.*

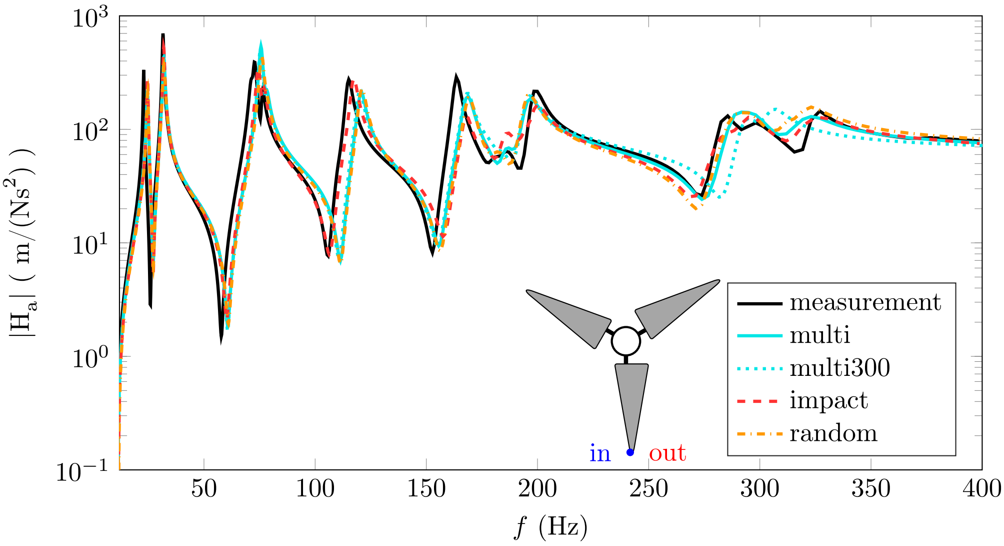

(a) *Different models*

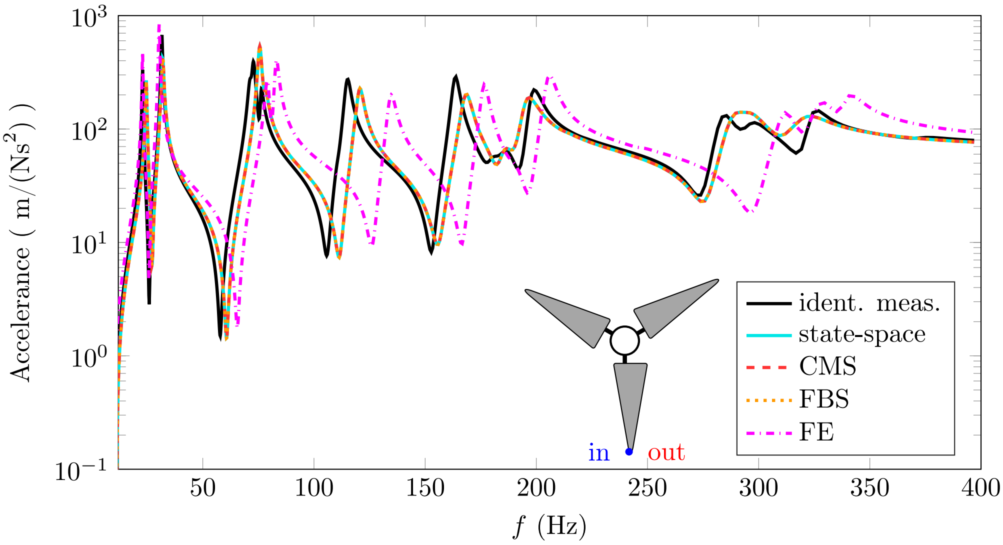

(b) *Different substructuring methods*

Figure 4.18: *Direct accelerance FRF of the three-bladed hub for the input/output location 24. The identified measurement model is compared to the models* multi, multi300, impact, *and* random *in the upper figure. All models correlate very well with the identified system. The lower plot shows a comparison between the methods state-space coupling, CMS, and FBS for the model* multi *together with the nominal FE model. All methods yield the same results when based on the same data, which is a better replication of the true system than the FE model.*

FE	identified				substructured			
	multi		impact		multi		impact	
f_i (Hz)	f_i (Hz)	ξ_i (%)	f_i (Hz)	ξ_i (%)	f_i (Hz)	ξ_i (%)	f_i (Hz)	ξ_i (%)
22.91	22.91	0.80	22.89	0.30	24.57	1.37	24.64	0.93
30.34	30.69	0.85	30.60	0.40	30.97	1.40	30.95	1.13
30.34	31.57	0.89	31.52	0.51	31.94	1.40	31.89	1.09
83.01	71.34	1.23	70.87	1.40	75.63	1.05	74.47	1.32
83.02	72.71	1.10	72.21	1.26	78.05	1.16	76.82	1.18
79.12	76.19	0.86	75.94	0.81	82.41	1.11	81.40	1.16
134.52	110.62	1.39	109.45	1.18	118.60	1.44	113.81	1.45
134.49	114.93	1.27	113.59	1.48	120.46	1.39	117.18	1.37
176.45	163.46	1.03	163.00	1.04	168.26	1.56	167.82	1.55
189.63	179.78	1.90	179.06	1.97	174.19	4.26	174.92	2.19
188.85	181.36	1.89	184.01	2.08	176.26	2.94	179.36	2.40
189.63	185.50	2.43	187.78	0.60	185.37	2.00	185.28	2.13
205.45	198.12	1.24	197.31	1.22	195.44	1.83	194.43	1.87
205.45	200.24	1.42	199.73	1.39	199.44	1.76	198.81	1.62
246.91	221.58	1.37	218.51	1.68	212.97	2.29	215.19	2.18

Table 4.6: *Modal parameters of first five flexible mode groups for the three-bladed hub including the FE model, the identified, and the substructured models* multi *and* impact. *Note that the FE modes are sorted to match the identified models.*

error f_i				error ξ_i	
FE - ident		ident - substr		ident - substr	
FE - multi (%)	FE - impact (%)	multi - multi (%)	multi - impact (%)	multi - multi (%)	multi - impact (%)
0.01	-0.05	7.24	7.55	70.32	16.52
1.17	0.88	0.90	0.85	65.08	33.80
4.07	3.91	1.18	1.01	55.98	21.63
-9.84	-10.43	6.02	4.39	-14.53	7.73
-12.41	-13.01	7.34	5.65	5.09	7.16
-8.23	-8.52	8.16	6.84	28.29	34.51
-17.75	-18.62	7.21	2.88	3.64	5.04
-14.57	-15.56	4.81	1.96	8.85	7.42
-7.36	-7.62	2.94	2.67	51.23	50.60
-4.80	-5.18	-3.11	-2.71	124.11	15.39
-4.36	-2.96	-2.81	-1.10	55.38	26.80
-2.17	-0.97	-0.07	-0.12	-17.50	-12.34
-3.57	-3.96	-1.35	-1.86	47.37	50.77
-2.54	-2.79	-0.40	-0.72	23.86	13.49
-10.26	-11.51	-3.89	-2.88	69.69	58.93

Table 4.7: *Errors of the modal parameters of first five flexible mode groups for the three-bladed hub. Comparisons between the FE model and the identified models as well as between the identified model and the substructuring results are drawn for the resonance frequencies. Furthermore, the damping errors between the identified and substructured models are compared. For the identified and substructured models, the results obtained with* multi *and* impact *are contrasted. Note that the FE modes are sorted to match the identified models in accordance with Table 4.6.*

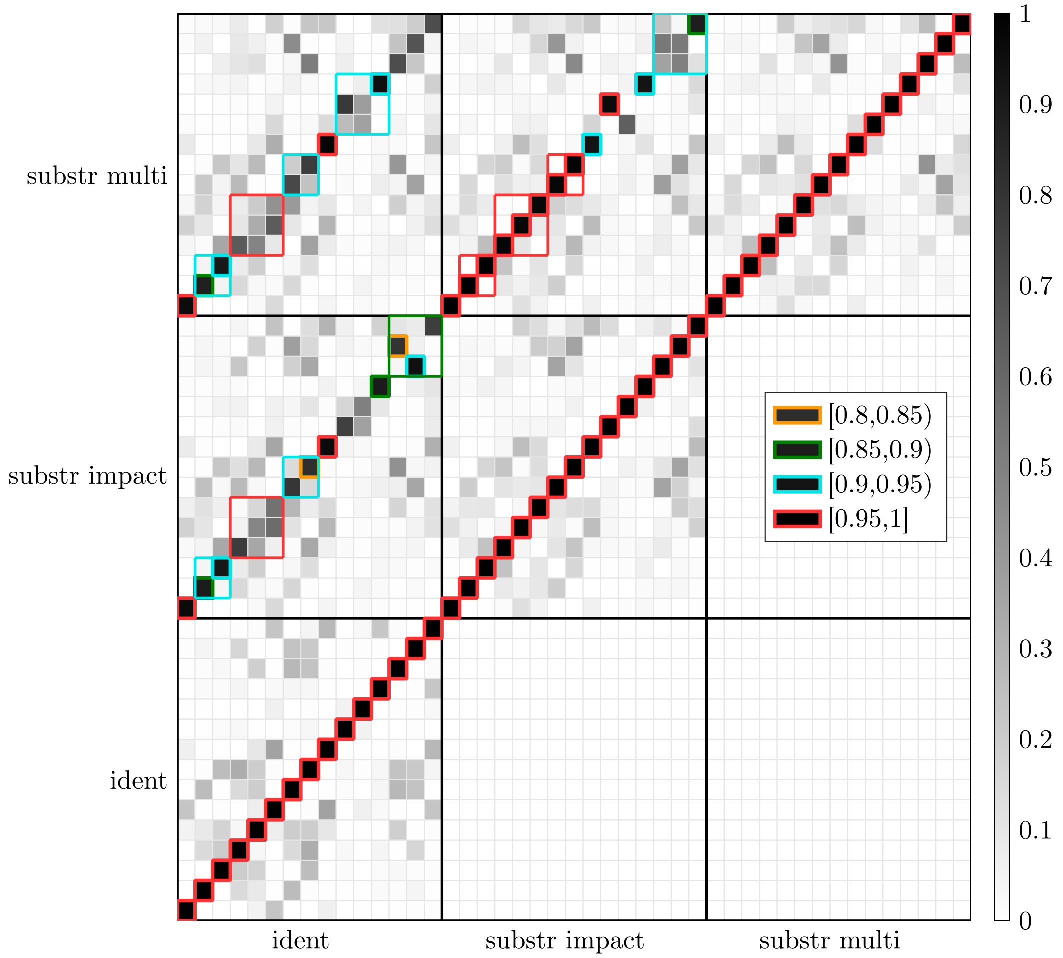

Figure 4.19: *MAC value comparison for the three-bladed hub including the first 15 flexible modes. The substructured multisine and impact models are compared to the identified multisine model. The coloured frames are connected to the angles between the subspaces spanned by the mode shape groups.*

4.8 Discussion

In order to judge the satisfaction of the constraint equations, the motion of the hub of the three substructures and the transmission simulator were plotted similar to the plots by Rohe and Mayes [17]. If the constraints are fulfilled perfectly, there should be no difference in the motion. However, for low frequency flexible modes, the motion of some sensors differs, which may stem either from the modal relaxation of the constraints or from measurement errors.

So far, this check cannot be performed with state-space synthesis. The physical coordinates describing the measurement points' motion are transformed to modal coordinates using the matrix $(\mathbf{\Phi}^{(ts)}_{meas})^{+}$. Then, a reduced set of modal coordinates is chosen to represent the coupled system. In CMS, the choice allows for a transformation back to physical coordinates using the mode shape matrices of the substructures. In state-space coupling, the modal coordinates of only the transmission simulator are chosen as the reduced set assuming that all modal coordinates are exactly equal. After this choice, the physical motion can no longer be deduced in a direct way.

To improve the constraints, it was attempted to add flexible modes to the transmission simulator mode shape matrix. This results in higher errors in the modal parameters however, and the predicted resonance frequencies do not match the true ones any longer. In fact, the first resonance frequency is lowered, whereas the second is increased substantially for one added flexible mode. If three flexible modes are included to account for the symmetry of the hub, the first resonance frequency is increased significantly to over 40 Hz. This observation is even more pronounced for six added flexible modes. Although, the mass and stiffness matrices are still positive definite and semi-definite.

One possible explanation is that adding more modes increases the condition number, which is believed to be crucial for the transmission simulator technique's applicability in experimental coupling [14]. Yet, other effects may also have influenced the results, since the increase is not substantial. The condition number of the mode shape matrix including only rigid body modes is 1.90 and increases to 2.81 for one flexible mode and to 3.01 for three flexible modes.

In order to lower the condition number, more sensors have to be included along with more modes. However, this approach is limited by the number of sensors available. Still, the effect of equipping the brackets with only triaxial sensors on the same locations was investigated by means of FE models only. The numerical study indicated that the aforementioned stiffening effect can be reduced, although only to a limited extent.

The high damping errors could be a sign of an inappropriate damping model. The main source of dissipation is likely to be in the joints, which is probably unsatisfactorily represented by modal damping [18].

Finally, the obtained substructuring results are compared to the results achieved by Roettgen and Mayes [18]. Both the errors for the resonance frequencies and the modal damping ratios are comparable. However, the absolute values of the resonance frequencies are lower for the structure of Roettgen and Mayes revealing that the blades used in the present thesis are stiffer. The MAC values here are lower, yet the angles between the subspaces indicate equally good results.

The results may be influenced by the chosen measurement setup. For instance, non-linearities might become more apparent by measuring close to the joints since the bolts are known to introduce non-linearities to the interface [50]. Still, the brackets were chosen as sensor locations, since mounting the sensors on the brackets enables excitation and measuring in the same direction due to the plain surface.

Other possible sources of errors related to the measurement setup include the suspension. The highest rigid body mode should be less than 20 % of the lowest flexible mode [29]. However, in the measurements, a small peak was found at around 15 Hz which might be a suspension mode influencing the substructuring results. It was found that stinger resonance has no impact on the frequency range of interest. To judge this, the stinger's mass was increased with additional nuts. Since no influence on the measurement was found, the stinger was removed from the list of potential sources of errors. However, no further investigation on shaker or suspension resonances was performed.

The pronounced differences in the measurements above 400 Hz, reported earlier, could also be due to resonance in the suspension. However, the modes in this frequency range are dominated by an in-plane motion which might be particularly sensitive to the input direction. A slight misalignment of the stinger could then cause large deviations. Similar issues were reported in the work of Gibanica et al. [40].

Furthermore, Maxwell's reciprocity theorem is used in order to retrieve the unmeasured FRFs, based on the assumption that one co-located input/output pair is known. Due to the offset between sensor and fastener location, this pair is no longer strictly co-located which may introduce errors during the system identification procedure. The effect was considered negligible. Yet another source of error may be caused by system identification. Liljerehn and Abrahamsson [13] found that the peak value of the identified FRF has a large influence on the substructuring results. In fact, a lower peak causes an increase in the predicted resonance frequencies after substructuring. Even though the identified models replicate the measurements well, a maximum difference between the peak heights was found to be -4.5%, which might be an explanation for the higher resonance frequencies. Moreover, the absolute value of the error for the first mode in the receptance FRF, which are used for coupling, is larger than for the other modes due to the larger displacements for this mode. Thus, the first mode may be influenced the most, explaining the rather high error in the first substructure mode.

Lastly, in total eleven sensors, listed in section 4.6.1, turned out to be defective and where removed from the system identification procedure. Repeating the measurements to achieve a full set of measured points could possibly improve the substructuring results.

Despite the aforementioned causes for errors, the results of the substructuring are satisfying over a large frequency range. Thus, the transmission simulator with least squares constraints is indeed capable of levelling out such kinds of measurement errors.

5 Conclusion and Future Work

The goal of this thesis was to transfer the transmission simulator to state-space synthesis and to verify the method by experiments.

The transmission simulator was developed in the last years to overcome hindrances connected to experimental dynamic substructuring. Problems often encountered are related to the experimental setup in free-free configuration and the measurement of interface DOFs. By applying new, relaxed coupling conditions along with the transmission simulator, measurement errors can be levelled out. So far, this technique was applied to the well-known methods CMS and FBS in the modal and frequency domain, respectively.

However, a third substructuring method exists in the state-space domain, allowing for the wide field of first-order system identification methods. Here, state-space models are coupled directly, hence the name state-space synthesis. To combine the advantages that stem from both the transmission simulator technique and the state-space synthesis, these methods were combined in the thesis at hand.

To achieve this, subtraction of state-space models was derived first theoretically. Moreover, the transmission simulator was transferred to the state-space domain. Both the constraints CPT and MCFS were applied, followed by a verification of the newly developed state-space transmission simulator. To this end, a simple theoretical example as well as an experimental structure were utilized. With the obtained results, it was shown that the methods CMS, FBS and state-space synthesis are equivalent. The FRFs of all three methods as well as the estimated resonance frequencies and damping ratios of CMS and state-space synthesis are identical if the same models are used.

The theoretical example was built up by two plane beams. With the help of this example, important requirements for the transmission simulator involving the design, sensor placement and the included mode shapes were illustrated.

Furthermore, the state-space transmission simulator was tested with an experimental structure. The comparison of the results showed that the substructured models replicate the true system well for the full frequency range of interest. In general, these models are better representations than the nominal FE model used. The resonance frequencies of the subtructured models are closer to the true values than the FE prediction. Moreover, damping can be estimated by dynamic substructuring but was not included in the FE model at hand. Hence, dynamic substructuring outperforms FE modelling for this application.

Experimental substructuring was performed on the Ampair wind turbine benchmark structure. Three one-bladed hubs were measured and the hub as transmission simulator was removed twice to arrive at a model of the three-bladed hub. The results were compared with the measured true system.

By applying different excitation types, using both a shaker and an impact hammer, it showed that the models based on multisine and impact testing yielded the best results. They were comparable in their quality. Based on the experimental data, different models were identified in a thorough system identification procedure. After the enforcement of physical properties in the models, the substructured results obtained with different measurement data were compared to the true system.

Still, there are numerous challenges related to state-space coupling with the transmission simulator. This includes a verification of the coupling constraints, i.e. MCFS, by means of the measurement points' physical motion. So far, this information is not available in state-space synthesis. Therefore, derivations in state-space domain are required in order to enable this helpful check.

Moreover, the method formulation could be modified such that more than two state-space models can be coupled at a time. At last, the prerequisites of state-space synthesis hamper coupling of continuous interfaces. Further research on such interfaces could provide an alternative approach to the transmission simulator. Another research topic involves an investigation regarding the robustness of the transmission simulator or a sensitivity study related to the transmission simulator design.

References

[1] **D. de Klerk, D. J. Rixen, and S. N. Voormeeren**. General Framework for Dynamic Substructuring: History, Review and Classification of Techniques. *AIAA Journal* **46**.5 (2008), 1169–1181.

[2] **R. Mayes, P. S. Hunter, and T. W. Simmermacher**. Combining Lightly Damped Experimental Substructures with Analytical Substructures. *Proceedings of the 25th International Modal Analysis Conference*. Orlando, Florida, USA, 2007.

[3] **R. L. Mayes**. An Introduction to the SEM Substructures Focus Group Test Bed - The Ampair 600 Wind Turbine. *Proceedings of the 30th International Modal Analysis Conference*. Jacksonville, Florida, USA, 2012.

[4] **R. R. Craig and A. J. Kurdila**. *Fundamentals of Structural Dynamics*. 2nd ed. Hoboken, New Jersey, USA: John Wiley & Sons Inc., 2006.

[5] **L. Meirovitch**. *Computational methods in structural dynamics*. Alphen aan den Rijn, The Netherlands: Sijthoff & Noordhoff, 1980.

[6] **R. E. D. Bishop and D. C. Johnson**. *The Mechanics of Vibrations*. Cambridge, UK: Cambridge University Press, 1960.

[7] **B. Jetmundsen, R. L. Bielawa, and W. G. Flannelly**. Generalized Frequency Domain Substructure Synthesis. *Journal of the American Helicopter Society* **33**.1 (1988), 55–64.

[8] **P. Sjövall**. Component Synthesis and Identification in Structural Dynamics. Licentiate thesis. Chalmers University of Technology, 2004.

[9] **P. Sjövall and T. Abrahamsson**. Component system identification and state-space model synthesis. *Mechanical Systems and Signal Processing* **21**.7 (2007), 2697–2714.

[10] **T.-J. Su and J.-N. Juang**. Substructure system identification and synthesis. *Journal of Guidance, Control, and Dynamics* **17**.5 (1994), 1087–1095.

[11] **L. Ljung**. *System Identification: Theory for the User*. 2nd ed. Upper Saddle River, New Jersey, USA: Prentice-Hall, 1999, pp. 132–134.

[12] **T. Mckelvey, H. Akcay, and L. Ljung**. Subspace-based Multivariable System Identification from Frequency Response Data. *IEEE Transactions on Automatic Control* **41**.7 (1996).

[13] **A. Liljerehn and T. Abrahamsson**. Experimental-Analytical Substructure Model Sensitivity Analysis for Cutting Machine Chatter Prediction. *Proceedings of the 30th International Modal Analysis Conference*. Jacksonville, Florida, USA, 2012.

[14] **R. L. Mayes and M. Arviso**. Design Studies for the Transmission Simulator Method to Generate Experimental Dynamic Substructures. *24th International Conference on Noise and Vibration Engineering (ISMA)*. Leuven, Belgium, 2010.

[15] **M. S. Allen and R. L. Mayes**. Comparison of FRF and Modal Methods for Combining Experimental and Analytical Substructures. *Proceedings of the 25th International Modal Analysis Conference*. Orlando, Florida, USA, 2007.

[16] **R. L. Mayes**. Tutorial on Experimental Dynamic Substructuring Using the Transmission Simulator Method. *Proceedings of the 30th International Modal Analysis Conference*. Jacksonville, Florida, USA, 2012.

[17] **D. P. Rohe and R. L. Mayes**. Coupling of a Bladed Hub to the Tower of the Ampair 600 Wind Turbine Using the Transmission Simulator Method. *Proceedings of the 31st International Modal Analysis Conference*. Garden Grove, California, USA, 2013.

[18] **D. R. Roettgen and R. L. Mayes**. Ampair 600 Wind Turbine Three-Bladed Assembly Substructuring Using the Transmission Simulator Method. *Proceedings of the 33rd International Modal Analysis Conference*. Orlando, Florida, USA, 2015.

[19] **D. C. Kammer, M. S. Allen, and R. L. Mayes**. Formulation of a Craig-Bampton Experimental Substructure Using a Transmission Simulator. *Proceedings of the 31st International Modal Analysis Conference*. Garden Grove, California, USA, 2013.

[20] **M. Gibanica**. Experimental-Analytical Dynamic Substructuring. MSc thesis. Chalmers University of Technology, 2013.

[21] **M. S. Allen, R. L. Mayes, and E. J. Bergman**. Experimental modal substructuring to couple and uncouple substructures with flexible fixtures and multi-point connections. *Journal of Sound and Vibration* **329**.23 (2010), 4891–4906.

[22] **M. Gibanica et al.** Experimental-Analytical Dynamic Substructuring of Ampair Testbed: A State-Space Approach. *Proceedings of the 32nd International Modal Analysis Conference*. Orlando, Florida, USA, 2014.

[23] **M. V. van der Seijs et al.** Validation of Current State Frequency Based Substructuring Technology for the Characterisation of Steering Gear–Vehicle Interaction. *Proceedings of the 31st International Modal Analysis Conference*. Garden Grove, California, USA, 2013.

[24] **M. S. Allen, D. C. Kammer, and R. L. Mayes**. Metrics for diagnosing negative mass and stiffness when uncoupling experimental and analytical substructures. *Journal of Sound and Vibration* **331**.25 (2012), 5435–5448.

[25] **R. L. Mayes, M. S. Allen, and D. C. Kammer**. Eliminating Indefinite Mass Matrices with the Transmission Simulator Method of Substructuring. *Proceedings of the 30th International Modal Analysis Conference*. Jacksonville, Florida, USA, 2012.

[26] **B. Seeger**. Chances and Limitations of the Transmission Simulator Techniques: A Numerical Study. Student thesis. University of Stuttgart, 2015.

[27] **W. D'Ambrogio and A. Fregolent**. Direct hybrid formulation for substructure decoupling. *Proceedings of the 30th International Modal Analysis Conference*. Jacksonville, Florida, USA, 2012.

[28] **R. L. Mayes and D. P. Rohe**. Coupling Experimental and Analytical Substructures with a Continuous Connection Using the Transmission Simulator Method. *Proceedings of the 31st International Modal Analysis Conference*. Garden Grove, California, USA, 2013.

[29] **D. J. Ewins**. *Modal Testing: Theory, Practice and Application*. 2nd ed. Baldock,UK: Research Studies Press Ltd., 2000.

[30] **T. Abrahamsson**. Modal Parameter Extraction for Nonproportionally Damped Linear Structures. *The International Journal of Analytical and Experimental Modal Analysis* **3**.2 (1988), 62–68.

[31] **P. Van Overschee and B. De Moor**. *Subspace identification for linear systems: Theory — Implementation — Applications*. 1st ed. Dordrecht, The Netherlands: Springer US, 1996.

[32] **V. Yaghoubi and T. Abrahamsson**. Automated Modal Analysis Based on Frequency Response Function Estimates. *Proceedings of the 30th International Modal Analysis Conference*. Jacksonville, Florida, USA, 2012.

[33] **A. Liljerehn and T. Abrahamsson**. Dynamic sub-structuring with passive state-space components. *26th International Conference on Noise and Vibration Engineering (ISMA)*. Leuven, Belgium, 2014.

[34] **J. N. Reddy**. *An Introduction to Continuum Mechanics with applications*. New York, USA: Cambridge University Press, 2008.

[35] **R. J. Allemang**. The Modal Assurance Criterion (MAC): Twenty Years of Use and Abuse. *Proceedings of SPIE - The International Society for Optical Engineering*. 2002,

[36] **R. Brincker and C. Ventura**. *Introduction to Operational Modal Analysis*. Chichester, UK: John Wiley & Sons Inc., 2015. Chap. 12.

[37] **H. P. Gavin**. Structural Element. Stiffness, Mass, and Damping Matrices. Duke University, Department of Civil and Environmental Engineering CEE 541 Structural Dynamics. 2014.

[38] **J. Harvie and P. Avitabile**. Comparison of Some Wind Turbine Blade Tests in Various Configurations. *Proceedings of the 30th International Modal Analysis Conference*. Jacksonville, Florida, USA, 2012.

[39] **R. L. Mayes**. Wind Turbine Experimental Dynamic Substructure Development. *Proceedings of the 30th International Modal Analysis Conference*. Jacksonville, Florida, USA, 2012.

[40] **M. Gibanica et al.** Spread in Modal Data Obtained from Wind Turbine Blade Testing. *Proceedings of the 31st International Modal Analysis Conference*. Garden Grove, California, USA, 2013.

[41] **A. Linderholt et al.** A Comparison of the Dynamic Behavior of Three Sets of the Ampair 600 Wind Turbine. *Proceedings of the 33rd International Modal Analysis Conference*. Orlando, Florida, USA, 2015.

[42] **S. Rahimi, D. de Klerk, and D. J. Rixen**. The Ampair 600 Wind Turbine Benchmark: Results From the Frequency Based Substructuring Applied to the Rotor Assembly. *Proceedings of the 31st International Modal Analysis Conference*. Garden Grove, California, USA, 2013.

[43] **J. Brunetti et al.** Selection of Interface DoFs in Hub-Blade(s) Coupling of Ampair Wind Turbine Test Bed. *Proceedings of the 31st International Modal Analysis Conference*. Garden Grove, California, USA, 2013.

[44] **J. Brunetti et al.** Experimental Dynamic Substructuring of the Ampair Wind Turbine Test Bed. *Proceedings of the 32nd International Modal Analysis Conference*. Orlando, Florida, USA, 2014.

[45] **D. Macknelly, M. Nurbhai, and N. Monk**. IMAC XXXI: Additional Modal Testing of Turbine Blades and the Application of Transmission Simulator Substructuring Methodology for Coupling. *Proceedings of the 31st International Modal Analysis Conference*. Garden Grove, California, USA, 2013.
[46] **A. T. Johansson et al.** Modeling and Calibration of Small-Scale Wind Turbine Blade. *Proceedings of the 31st International Modal Analysis Conference*. Garden Grove, California, USA, 2013.
[47] **SIEMENS**. *NX Nastran 10 - Quick Reference Guide*. 2014.
[48] **Sandia National Laboratories**. *Substructuring Testbed Assembly Instructions*. Tech. rep. 2012. URL: `http://substructure.engr.wisc.edu`.
[49] **M. Khorsand Vakilzadeh et al.** Experiment Design for Improved Frequency Domain Subspace System Identification of Continuous-Time Systems. 17th IFAC Symposium on System Identification. Bejing, China, 2015.
[50] **P. Reuß et al.** Identification of Nonlinear Joint Characteristic in Dynamic Substructuring. *Proceedings of the 31st International Modal Analysis Conference*. Garden Grove, California, USA, 2013.

A Appendix to the Theory Chapter

This chapter is the appendix to the theory chapter. First, Jetmundsen's formulation for FBS will be derived and then, one special case of the Woodbury matrix identity is given.

A.1 Jetmundsen's formulation

The derivation of this formula uses the FRF of the substructures 1 and 2, respectively

$$\begin{bmatrix} Q_c^{(s)} \\ Q_b^{(s)} \end{bmatrix} = \boldsymbol{H}^{(s)} \begin{bmatrix} F_c^{(s)} \\ F_b^{(s)} \end{bmatrix} \tag{A.1}$$

with

$$\boldsymbol{H}^{(s)} = \begin{bmatrix} \boldsymbol{H}_{cc}^{(s)} & \boldsymbol{H}_{cb}^{(s)} \\ \boldsymbol{H}_{bc}^{(s)} & \boldsymbol{H}_{bb}^{(s)} \end{bmatrix} \tag{A.2}$$

and the coupling conditions for two substructures

$$F_c^{(1)} + F_c^{(2)} = F_c \tag{A.3}$$

and

$$Q_c^{(1)} = Q_c^{(2)} = Q_c. \tag{A.4}$$

The derivation starts with rewriting equation (A.4) using the FRFs of the substructures,

$$\boldsymbol{H}_{cc}^{(1)} F_c^{(1)} + \boldsymbol{H}_{cb}^{(1)} F_b^{(1)} = \boldsymbol{H}_{cc}^{(2)} F_c^{(2)} + \boldsymbol{H}_{cb}^{(2)} F_b^{(2)}. \tag{A.5}$$

Expressing $F_c^{(1)}$ in terms of F_c and $F_c^{(2)}$ with equation (A.3) yields

$$F_c^{(2)} = \left(\boldsymbol{H}_{cc}^{(1)} + \boldsymbol{H}_{cc}^{(2)}\right)^{-1} \left(\boldsymbol{H}_{cc}^{(1)} F_c + \boldsymbol{H}_{cb}^{(1)} F_b^{(1)} - \boldsymbol{H}_{cb}^{(2)} F_b^{(2)}\right). \tag{A.6}$$

$Q_b^{(1)}$ can be written as

$$Q_b^{(1)} = \boldsymbol{H}_{bc}^{(1)} F_c^{(1)} + \boldsymbol{H}_{bb}^{(1)} F_b^{(1)} \tag{A.7}$$

If one uses $F_c^{(1)} = F_c - F_c^{(2)}$ and equation (A.6), the equation can be rewritten with

$$Q_b^{(1)} = \left(\boldsymbol{H}_{bb}^{(1)} - \boldsymbol{H}_{bc}^{(1)} (\boldsymbol{H}_c)^{-1} \boldsymbol{H} cb^{(1)}\right) F_b^{(1)} + \left(\boldsymbol{H}_{bc}^{(1)} - \boldsymbol{H}_{bc}^{(1)} (\boldsymbol{H}_c)^{-1} \boldsymbol{H}_{cc}^{(1)}\right) F_c + \boldsymbol{H}_{bc}^{(1)} (\boldsymbol{H}_c)^{-1} \boldsymbol{H}_{cb}^{(2)} F_b^{(2)} \tag{A.8}$$

with the abbreviation $\boldsymbol{H}_c = \left(\boldsymbol{H}_{cc}^{(1)} + \boldsymbol{H}_{cc}^{(2)}\right)$. Comparing this to the first equation of the coupled FRF

$$Q_b^{(1)} = \bar{\boldsymbol{H}}_{bb}^{(11)} F_b^{(1)} + \bar{\boldsymbol{H}}_{bc}^{(1c)} F_c + \bar{\boldsymbol{H}}_{bb}^{(22)} F_b^{(2)} \tag{A.9}$$

yields

$$\bar{\boldsymbol{H}}_{bb}^{(11)} = \boldsymbol{H}_{bb}^{(1)} - \boldsymbol{H}_{bc}^{(1)} (\boldsymbol{H}_c)^{-1} \boldsymbol{H}_{cb}^{(1)} \tag{A.10}$$

$$\bar{\boldsymbol{H}}_{bc}^{(1c)} = \boldsymbol{H}_{bc}^{(1)} - \boldsymbol{H}_{bc}^{(1)} (\boldsymbol{H}_c)^{-1} \boldsymbol{H}_{cc}^{(1)} \tag{A.11}$$

$$\bar{\boldsymbol{H}}_{bb}^{(12)} = \boldsymbol{H}_{bc}^{(1)} (\boldsymbol{H}_c)^{-1} \boldsymbol{H}_{cb}^{(2)}. \tag{A.12}$$

In the same manner, $Q_b^{(2)} = \boldsymbol{H}_{bc}^{(2)} F_c^{(2)} + \boldsymbol{H}_{bb}^{(2)} F_b^{(2)}$ can be rewritten with equation (A.6), yielding

$$\bar{\boldsymbol{H}}_{bb}^{(21)} = \boldsymbol{H}_{bc}^{(2)} (\boldsymbol{H}_c)^{-1} \boldsymbol{H}_{cb}^{(1)} \tag{A.13}$$

$$\bar{\boldsymbol{H}}_{bc}^{(2c)} = \boldsymbol{H}_{bc}^{(2)} (\boldsymbol{H}_c)^{-1} \boldsymbol{H}_{cc}^{(1)} \tag{A.14}$$

$$\bar{\boldsymbol{H}}_{bb}^{(22)} = \boldsymbol{H}_{bb}^{(2)} - \boldsymbol{H}_{bc}^{(2)} (\boldsymbol{H}_c)^{-1} \boldsymbol{H}_{cb}^{(2)}. \tag{A.15}$$

The missing FRF entries are found by the equation $Q_c = Q_c^{(1)} = \boldsymbol{H}_{cc}^{(1)} F_c^{(1)} + \boldsymbol{H}_{cb}^{(1)} F_b^{(1)}$. Once more replacing $F_c^{(1)}$ and using equation (A.6), the entries are

$$\bar{\boldsymbol{H}}_{cb}^{(c1)} = \boldsymbol{H}_{cb}^{(1)} - \boldsymbol{H}_{cc}^{(1)} (\boldsymbol{H}_c)^{-1} \boldsymbol{H}_{cb}^{(1)} \tag{A.16}$$

$$\bar{\boldsymbol{H}}_{cc}^{(cc)} = \boldsymbol{H}_{cc}^{(1)} - \boldsymbol{H}_{cc}^{(1)} (\boldsymbol{H}_c)^{-1} \boldsymbol{H}_{cc}^{(1)} \tag{A.17}$$

$$\bar{\boldsymbol{H}}_{cb}^{(c2)} = \boldsymbol{H}_{cc}^{(1)} (\boldsymbol{H}_c)^{-1} \boldsymbol{H}_{cb}^{(2)}. \tag{A.18}$$

In matrix form, those equations are

$$\begin{bmatrix} Q_b^{(1)} \\ Q_c \\ Q_b^{(2)} \end{bmatrix} = \begin{bmatrix} \boldsymbol{H}_{bb}^{(1)} - \boldsymbol{H}_{bc}^{(1)} (\boldsymbol{H}_c)^{-1} \boldsymbol{H}_{cb}^{(1)} & \boldsymbol{H}_{bc}^{(1)} - \boldsymbol{H}_{bc}^{(1)} (\boldsymbol{H}_c)^{-1} \boldsymbol{H}_{cc}^{(1)} & \boldsymbol{H}_{bc}^{(1)} (\boldsymbol{H}_c)^{-1} \boldsymbol{H}_{cb}^{(2)} \\ \boldsymbol{H}_{cb}^{(1)} - \boldsymbol{H}_{cc}^{(1)} (\boldsymbol{H}_c)^{-1} \boldsymbol{H}_{cb}^{(1)} & \boldsymbol{H}_{cc}^{(1)} - \boldsymbol{H}_{cc}^{(1)} (\boldsymbol{H}_c)^{-1} \boldsymbol{H}_{cc}^{(1)} & \boldsymbol{H}_{cc}^{(1)} (\boldsymbol{H}_c)^{-1} \boldsymbol{H}_{cb}^{(2)} \\ \boldsymbol{H}_{bc}^{(2)} (\boldsymbol{H}_c)^{-1} \boldsymbol{H}_{cb}^{(1)} & \boldsymbol{H}_{bc}^{(2)} (\boldsymbol{H}_c)^{-1} \boldsymbol{H}_{cc}^{(1)} & \boldsymbol{H}_{bb}^{(2)} - \boldsymbol{H}_{bc}^{(2)} (\boldsymbol{H}_c)^{-1} \boldsymbol{H}_{cb}^{(2)} \end{bmatrix} \begin{bmatrix} F_b^{(1)} \\ F_c \\ F_b^{(2)} \end{bmatrix} \tag{A.19}$$

or

$$\bar{\boldsymbol{H}} = \begin{bmatrix} \boldsymbol{H}_{bb}^{(1)} & \boldsymbol{H}_{bc}^{(1)} & \boldsymbol{0} \\ \boldsymbol{H}_{cb}^{(1)} & \boldsymbol{H}_{cc}^{(1)} & \boldsymbol{0} \\ \boldsymbol{0} & \boldsymbol{0} & \boldsymbol{H}_{bb}^{(2)} \end{bmatrix} - \begin{bmatrix} \boldsymbol{H}_{bc}^{(1)} \\ \boldsymbol{H}_{cc}^{(1)} \\ -\boldsymbol{H}_{bc}^{(2)} \end{bmatrix} \left(\boldsymbol{H}_{cc}^{(1)} + \boldsymbol{H}_{cc}^{(2)} \right)^{-1} \begin{bmatrix} \boldsymbol{H}_{bc}^{(1)} \\ \boldsymbol{H}_{cc}^{(1)} \\ -\boldsymbol{H}_{bc}^{(2)} \end{bmatrix}^T \tag{A.20}$$

which ends the derivations.

A.2 Woodbury matrix identity

Here, a special case of the Woodbury matrix identity is derived.

$$\begin{aligned}
\boldsymbol{A} - \boldsymbol{A}(\boldsymbol{A}+\boldsymbol{B})^{-1}\boldsymbol{A} &= \boldsymbol{A}\left[\boldsymbol{I} - (\boldsymbol{A}+\boldsymbol{B})^{-1}\boldsymbol{A}\right] \\
&= \boldsymbol{A}\left[\boldsymbol{I} - (\boldsymbol{A}+\boldsymbol{B})^{-1}\left(\boldsymbol{A}^{-1}\right)^{-1}\right] \\
&= \boldsymbol{A}\left[\boldsymbol{I} - \left(\boldsymbol{A}^{-1}(\boldsymbol{A}+\boldsymbol{B})\right)^{-1}\right] \\
&= \boldsymbol{A}\left[\boldsymbol{I} - \left(\boldsymbol{I}+\boldsymbol{A}^{-1}\boldsymbol{B}\right)^{-1}\right] \\
&= \boldsymbol{A}\left[\left(\boldsymbol{I}+\boldsymbol{A}^{-1}\boldsymbol{B}\right)\left(\boldsymbol{I}+\boldsymbol{A}^{-1}\boldsymbol{B}\right)^{-1} - \left(\boldsymbol{I}+\boldsymbol{A}^{-1}\boldsymbol{B}\right)^{-1}\right] \\
&= \boldsymbol{A}\left(\boldsymbol{I}+\boldsymbol{A}^{-1}\boldsymbol{B}-\boldsymbol{I}\right)\left(\boldsymbol{I}+\boldsymbol{A}^{-1}\boldsymbol{B}\right)^{-1} \\
&= \boldsymbol{A}\boldsymbol{A}^{-1}\boldsymbol{B}\left(\boldsymbol{I}+\boldsymbol{A}^{-1}\boldsymbol{B}\right)^{-1} \\
&= \left(\boldsymbol{B}^{-1}\right)^{-1}\left(\boldsymbol{I}+\boldsymbol{A}^{-1}\boldsymbol{B}\right)^{-1} \\
&= \left(\left(\boldsymbol{I}+\boldsymbol{A}^{-1}\boldsymbol{B}\right)\boldsymbol{B}^{-1}\right)^{-1} \\
&= \left(\boldsymbol{B}^{-1}+\boldsymbol{A}^{-1}\right)^{-1}
\end{aligned}$$

$$\begin{aligned}
\boldsymbol{A}(\boldsymbol{A}+\boldsymbol{B})^{-1}\boldsymbol{B} &= \left(\boldsymbol{A}^{-1}\right)^{-1}(\boldsymbol{A}+\boldsymbol{B})^{-1}\boldsymbol{B} \\
&= \left((\boldsymbol{A}+\boldsymbol{B})\boldsymbol{A}^{-1}\right)^{-1}\boldsymbol{B} \\
&= \left(\boldsymbol{I}+\boldsymbol{B}\boldsymbol{A}^{-1}\right)^{-1}\left(\boldsymbol{B}^{-1}\right)^{-1} \\
&= \left(\boldsymbol{B}^{-1}\left(\boldsymbol{I}+\boldsymbol{B}\boldsymbol{A}^{-1}\right)\right)^{-1} \\
&= \left(\boldsymbol{B}^{-1}+\boldsymbol{A}^{-1}\right)^{-1}
\end{aligned}$$

B Appendix to the Experimental Results

In this appendix, more experimental results of the substructuring in Chapter 4 are given. First, the identified modal parameters for all one-bladed hub models are listed, followed by the substructuring results of these models. At the end, the mode shapes of the substructured model are depicted.

B.1 Identified Modal Parameters for the One-Bladed Hubs

Here, all the identified resonance frequencies and modal damping ratios for all one-bladed hub models are given, including the models *multi800w*, *multi800wo*, *multi*, *multi300*, *auto*, *impact*, and *random*. Furthermore, the resonance frequencies of the FE model are listed.

	FE	multi800wo	multi800w	multi	multi300	auto	impact	random
	f_i (Hz)	f_i (Hz)	f_i (Hz)	f_i (Hz)	f_i (Hz)	f_i (Hz)	f_i (Hz)	f_i (Hz)
7	30.32	33.11	33.11	33.11	33.11	33.11	33.06	33.15
8	89.72	87.57	87.57	87.57	87.57	87.56	87.24	87.46
9	180.90	165.27	165.27	165.27	165.23	165.33	164.58	166.08
10	191.46	190.72	190.72	190.72	190.79	190.68	189.02	190.98
11	234.06	208.83	208.83	208.83	208.66	208.90	207.69	209.69
12	330.78	301.35	301.45	300.84	301.06	301.16	299.99	301.07
13	341.88	318.07	317.94	316.97		317.56	315.88	317.73
14	475.64		406.68	450.42			422.89	
15	517.88	448.25	448.76					
16	522.78	492.94	492.94					
17	636.54	540.50	540.61					
18	694.37	621.63	621.67					
19	736.72	681.38	681.34					
20	865.59	782.74	782.64					

Table B.1: *Identified resonance frequencies for structure A and all models.*

	multi800wo	multi800w	multi	multi300	auto	impact	random
	ξ_i (%)	ξ_i (%)	ξ_i (%)	ξ_i (%)	ξ_i (%)	ξ_i (%)	ξ_i (%)
7	1.34	1.34	1.34	1.34	1.33	1.07	1.60
8	1.24	1.24	1.24	1.24	1.22	1.37	1.37
9	1.71	1.71	1.71	1.70	1.67	1.76	1.76
10	2.30	2.30	2.30	2.44	2.70	2.41	2.85
11	1.68	1.68	1.68	1.65	1.61	1.62	1.50
12	1.74	1.65	1.79	1.35	1.78	1.93	1.86
13	1.71	1.53	1.89		1.84	1.88	2.14
14		0.36	12.90			3.94	
15	2.24	2.13					
16	1.12	1.12					
17	2.67	2.68					
18	1.67	1.67					
19	2.82	2.82					
20	2.35	2.36					

Table B.2: *Identified damping for structure A and all models.*

	FE f_i (Hz)	multi800wo f_i (Hz)	multi800w f_i (Hz)	multi f_i (Hz)	multi300 f_i (Hz)	auto f_i (Hz)	impact f_i (Hz)	random f_i (Hz)
7	30.32	31.38	31.38	31.38	31.38	31.39	31.41	31.25
8	89.72	89.75	89.75	89.75	89.75	89.74	89.48	89.84
9	180.90	164.89	164.89	164.89	164.84	164.38	161.59	165.67
10	191.46	176.01	176.01	176.01	177.76	179.20	180.25	184.21
11	234.06	199.36	199.36	199.36	199.38	199.71	197.62	199.83
12	330.78	301.14	301.14	301.15	301.11	301.01	296.91	302.27
13	341.88	317.94	317.94	318.16		317.97	315.70	319.12
14	475.64		394.10	410.54			379.99	402.78
15	517.88	434.30	433.62					
16	522.78	471.06	471.07					
17	636.54	523.30	523.14					
18	694.37	610.97	610.78					
19	736.72	683.19	682.91					
20	865.59	789.38	789.21					

Table B.3: *Identified resonance frequencies for structure B and all models.*

	multi800wo ξ_i (%)	multi800w ξ_i (%)	multi ξ_i (%)	multi300 ξ_i (%)	auto ξ_i (%)	impact ξ_i (%)	random ξ_i (%)
7	1.33	1.33	1.33	1.33	1.36	1.12	1.18
8	1.32	1.32	1.32	1.32	1.22	1.17	1.62
9	1.69	1.69	1.69	1.69	1.81	2.29	1.54
10	4.84	4.84	4.84	4.70	3.91	2.75	2.04
11	1.52	1.52	1.52	1.54	1.47	1.61	1.39
12	2.34	2.34	2.35	2.10	2.34	3.21	2.45
13	1.76	1.76	1.77		1.73	1.82	1.73
14		1.67	14.65			2.46	8.87
15	1.89	2.14					
16	2.37	2.44					
17	1.44	1.35					
18	2.61	2.59					
19	2.57	2.57					
20	0.55	0.56					

Table B.4: *Identified damping ratios for structure B and all models.*

	FE	multi800wo	multi800w	multi	multi300	auto	impact	random
	f_i (Hz)	f_i (Hz)	f_i (Hz)	f_i (Hz)	f_i (Hz)	f_i (Hz)	f_i (Hz)	f_i (Hz)
7	30.32	31.51	31.51	31.51	31.51	31.51	31.48	31.28
8	89.72	90.42	90.42	90.42	90.42	90.39	90.25	90.42
9	180.90	165.40	165.40	165.40	165.36	165.05	163.44	165.78
10	191.46	178.87	178.87	178.87	179.43	180.53	181.52	179.40
11	234.06	201.68	201.68	201.68	201.72	201.68	200.28	201.58
12	330.78	302.04	302.04	302.01	302.30	301.90	300.93	302.42
13	341.88	314.58	314.58	314.53		314.52	313.41	314.59
14	475.64		391.24	448.20			384.80	395.09
15	517.88	435.70	435.82					
16	522.78	476.11	477.22					
17	636.54	524.24	524.24					
18	694.37	633.42	633.42					
19	736.72	683.18	683.18					
20	865.59	791.45	791.45					

Table B.5: *Identified resonance frequencies for structure C and all models.*

	mutli800wo	multi800w	multi	multi300	auto	impact	random
	ξ_i (%)	ξ_i (%)	ξ_i (%)	ξ_i (%)	ξ_i (%)	ξ_i (%)	ξ_i (%)
7	1.50	1.50	1.50	1.50	1.51	1.21	1.56
8	1.22	1.22	1.22	1.22	1.15	1.23	1.09
9	1.59	1.59	1.59	1.57	1.58	1.71	1.53
10	3.24	3.24	3.24	3.32	3.00	2.46	2.14
11	1.48	1.48	1.48	1.50	1.46	1.47	1.50
12	2.25	2.25	2.21	1.98	2.21	2.45	2.35
13	1.46	1.46	1.48		1.47	1.41	1.40
14		7.73	12.47			0.46	183.27
15	1.89	1.84					
16	1.48	1.51					
17	1.84	1.84					
18	1.31	1.31					
19	2.17	2.17					
20	1.38	1.38					

Table B.6: *Identified damping ratios for structure C and all models.*

B.2 Substructuring Results

Here, results obtained with substructuring the models *multi800w*, *multi800wo*, *multi300*, *auto*, and *random* are listed.

	multi800wo		multi800w		auto		random		multi300	
	f_i (Hz)	ξ_i (%)	f_i (Hz)	ξ_i (%)	f_i (Hz)	ξ_i (%)	f_i (Hz)	ξ_i (%)	f_i (Hz)	ξ_i (%)
7	24.56	1.17	24.56	1.19	24.55	1.29	24.68	1.24	24.57	1.37
8	30.96	1.40	30.96	1.40	30.96	1.42	30.83	1.34	30.97	1.40
9	31.93	1.39	31.93	1.40	31.93	1.39	31.95	1.55	31.94	1.40
10	74.49	1.02	74.78	1.01	75.16	1.05	75.95	1.26	75.63	1.05
11	77.53	1.06	77.68	1.06	78.16	1.09	78.19	1.43	78.05	1.16
12	81.79	1.05	81.79	1.04	82.10	1.16	82.73	1.00	82.41	1.11
13	113.46	1.58	114.95	1.55	116.65	1.41	120.68	1.29	118.60	1.44
14	118.54	1.32	119.00	1.28	118.32	1.38	121.49	1.25	120.46	1.39
15	167.03	1.52	167.16	1.45	166.96	1.61	169.05	1.45	168.26	1.56
16	171.83	3.49	172.42	3.69	174.52	2.47	177.34	2.03	174.19	4.26
17	174.77	2.79	175.60	2.87	175.04	2.31	181.19	2.24	176.26	2.94
18	183.32	1.98	182.97	1.95	178.53	3.54	182.21	2.01	185.37	2.00
19	195.57	1.84	195.41	1.79	194.96	1.70	195.19	1.74	195.44	1.83
20	200.89	1.79	200.97	1.81	203.01	1.87	201.32	1.89	199.44	1.76
21	219.22	2.34	216.69	2.21	212.21	2.09	211.00	1.85	212.97	2.29

Table B.7: *Modal parameter for the other substructured models of the three-bladed hub*

B.3 Mode Shapes of the Three-Bladed Hub

Figure B.1 shows the first twelve flexible mode shapes of the three-bladed hub obtained with substructuring.

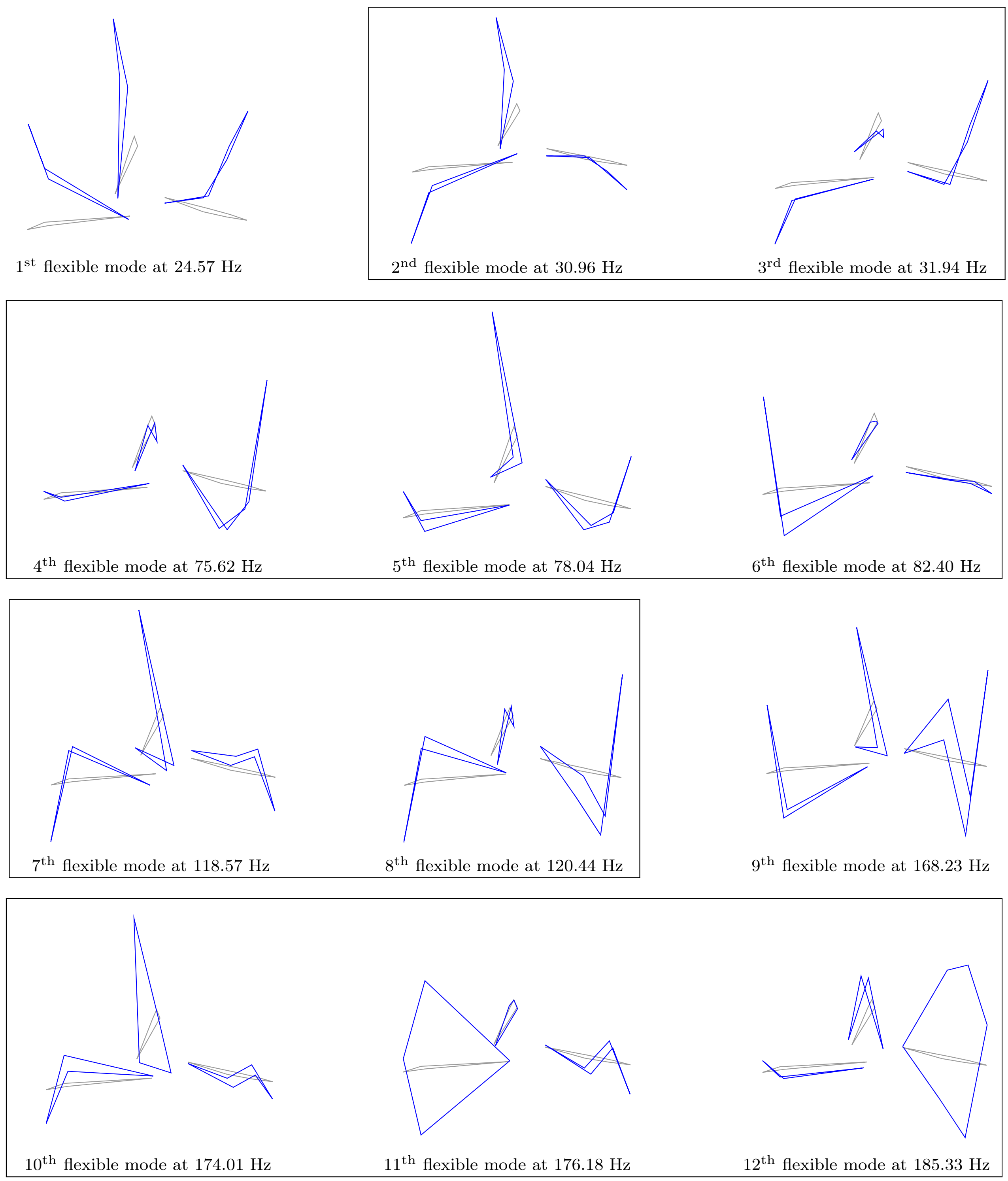

Fig. B.1: *The first twelve flexible mode shapes of the coupled system are shown here. Symmetric mode shapes that are close in frequency are framed. The first flexible mode is a bending mode with all blades in phase followed by two symmetric first bending modes where one blade is out of phase. The modes in the second row are second bending modes whereas the third row shows the third bending motion. Here, the seventh and eighth modes are symmetric, and in the ninth mode all blades are in phase. The next three modes combine bending with torsional motion where one blade is dominated by the latter. Not all nodes measured are plotted here and only out-of-plane displacements of the triaxial sensors are considered for the sake of visualization. The gray lines indicate the undeformed structure.*